Understanding Planet Formation Through High Precision Photometry and Spectroscopy

Thesis by

Alexandra Charlotte Lockwood

In Partial Fulfillment of the Requirements

for the Degree of

Doctor of Philosophy

California Institute of Technology

Pasadena, California

2014

(Submitted May 29, 2014)

I dedicate this thesis to PhDComics - may you empathize with, amuse, and inspire generations of grad students to come.

Acknowledgements

I've been fortunate enough to attend one of the best universities in the world for my graduate work and am thankful for the people and the experiences. I'd like to acknowledge my friends at Caltech, most of whom I was fortunate to share an office with for many years, Mike, Kondy, Ajay, Olga, Adam, Kelley, Josh, Masha, Adria, and Lauren. You were all amazing friends, even family, and made the journey a lot more enjoyable. I also appreciate the opportunities I had at Caltech – throwing social events for the grads with the Graduate Student Council and supporting the mental health of undergraduates through the Resident Associate program. Finally, I must recognize the PHD Movie. Through this work and the subsequent PhDetours, I have made great friends and allies and discovered my true passion: science outreach.

My family has always meant so much to me. Their continued belief in my abilities was the only thing keeping me going sometimes. We put the "fun" in "dysfunctional", with a lot of love in there as well. Along with family are my closest friends, Laura and Megan for whom I do not have words to express my love. Or maybe I do, but they were all put into this thesis! And lastly, I thank my recent partners in crime and closest companions, Rachael and Arnav, for you have made every day of this thesis writing better and I look forward to so many more wonderful memories.

Professionally, I am very grateful for my collaborators. Chad Bender, John Carr, and

Travis Barman, your quick and friendly correspondence made my venture into exoplanets a pleasant experience. John Stansberry was similarly kind and helpful and Mike Brown has taught me many things, for which I am appreciative. I'd especially like to acknowledge the important role that Klaus Pontoppidan has had in my graduate studies. I was fortunate to work with him a bit here at Caltech and then further at Space Telescope. Klaus always knew how to give me the details I needed to get the job done, while also answering my general scientific questions. And as hard-hitting as he could be, Klaus would provide a word of encouragement when it was most needed, thank you. Also, to Rebecca for putting up with me all those weeks and thanks to Luke for all the smiles.

I'd like to thank the members of my committee for helpful comments and critiques along the way. Most importantly, I'd like to recognize how each of you has realized the humanity in academia that is so often lost. Thank you Andy, for being an active demonstration of how to live humbly and happily as a science superstar. Thank you Yuk, for showing the option how students and advisors can be dedicated to each other, and how that relationship leads to productivity. Thank you Heather, for being a scientific role model of femininity, kindness, and acute perception and intelligence. You really are the future of planetary science and I am grateful for your strong presence in this role. Thank you John, for continually igniting my passion for discovery and believing in me while simultaneously pushing me to find my own answers. I would not be here today without you.

And last, but certainly not least, thank you Geoff. You have been my personal role model for balancing duty to the community and commitment to science. I have had the great fortune of getting to know you and Karen well over the past few years, and I hope you will always be part of my life. I will forever be grateful for your support and understanding throughout my graduate career.

Abstract

From studies of protoplanetary disks to extrasolar planets and planetary debris, we aim to understand the full evolution of a planetary system. Observational constraints from ground- and space-based instrumentation allows us to measure the properties of objects near and far and are central to developing this understanding. We present here three observational campaigns that, when combined with theoretical models, reveal characteristics of different stages and remnants of planet formation. The Kuiper Belt provides evidence of chemical and dynamical activity that reveals clues to its primordial environment and subsequent evolution. Large samples of this population can only be assembled at optical wavelengths, with thermal measurements at infrared and sub-mm wavelengths currently available for only the largest and closest bodies. We measure the size and shape of one particular object precisely here, in hopes of better understanding its unique dynamical history and layered composition.

Molecular organic chemistry is one of the most fundamental and widespread facets of the universe, and plays a key role in planet formation. A host of carbon-containing molecules vibrationally emit in the near-infrared when excited by warm gas, T$\sim$1000 K. The NIRSPEC instrument at the W.M. Keck Observatory is uniquely configured to study large ranges of this wavelength region at high spectral resolution. Using this facility we present studies of warm CO gas in protoplanetary disks, with a new code for precise excitation modeling. A parameterized suite of models demonstrates the abilities of the code and matches observational constraints such as line strength and shape. We use the models to probe various disk parameters as well, which are easily extensible to others with known disk emission spectra such as water, carbon dioxide, acetylene, and hydrogen cyanide.

Lastly, the existence of molecules in extrasolar planets can also be studied with NIRSPEC and reveals a great deal about the evolution of the protoplanetary gas. The species we observe in protoplanetary disks are also often present in exoplanet atmospheres, and are abundant in Earth's atmosphere as well. Thus, a sophisticated telluric removal code is necessary to analyze these high dynamic range, high-resolution spectra. We present observations of a hot Jupiter, revealing water in its atmosphere and demonstrating a new technique for exoplanet mass determination and atmospheric characterization. We will also be applying this atmospheric removal code to the aforementioned disk observations, to improve our data analysis and probe less abundant species. Guiding models using observations is the only way to develop an accurate understanding of the timescales and processes involved. The futures of the modeling and of the observations are bright, and the end goal of realizing a unified model of planet formation will require both theory and data, from a diverse collection of sources.

Contents

List of Figures

List of Tables

Chapter 1

Introduction

In the search for knowledge, we aim to answer the most basic questions: “who?”, “what?”, “where?”, “when?”, and “why?” The “how?” is also of particular interest to scientists, as we break down the processes that explain natural phenomenon. One of the most fundamental questions the human race has struggled with has to be “*why* are we here?” While science maybe not be able to answer this question directly, we can tackle the question “*how* have we come to be here?” Biologists have determined water to be one of the essential components of terrestrial life, if not the most important ingredient. Fortunately, water has been found abundantly in the Universe. But how, exactly, did the Earth come to acquire liquid oceans made of this precious biological medium? Why, further, is Venus too hot for human existence and Jupiter a giant ball of (mostly) gas? To address these questions we turn to understanding the process of planet formation and evolution. In this introductory chapter we will discuss the “what?”, “where?”, and “when?” of different stages of planetary evolution, using recent observational findings as the basis for framing further questions.

As astronomers, we make use of spectroscopy and photometry, at a multitude of wavelengths, to probe planetary systems as they are assembled and mature. To study the beginning of planetary evolution, in the so-called protoplanetary disk stage, we use wavelengths where the disk material is self-luminous and vastly outshines the central star. At near- and mid-infrared wavelengths, for example, spectroscopy of the rovibrational bands of molecules can be used to probe the simple organic species present in the inner few Astronomical Units (AU) of the disk. These species include water, the hydroxyl radial, methane, carbon monoxide and carbon dioxide, hydrogen cyanide and acetylene – many of which are best observed from space (Carr & Najita 2008; Salyk et al. 2008). For sufficiently high resolution observations from the ground taken at the right times of the year, however, rovibrational emission can be detected at wavelengths for which the Earth's atmosphere is sufficiently transparent. These same molecular species can be incorporated into gas giant planets (Swain et al. 2008, 2009; Konopacky et al. 2013), although the path is neither conservative nor direct. (See Figure 1.1 for a general schematic of the evolution of a planetary system).

We can also use the same spectroscopic instrumentation to study the end product of planetary evolution: the planets themselves. Specifically, the first exoplanets discovered (Mayor & Queloz 1995) have effective temperatures and gas densities that are sufficiently high to vibrationally excite these same molecules in their upper atmospheres, allowing the spectroscopic detection of abundant species therein. Along with the planets, debris is often regenerated in these systems, after the gas and primordial dust grains have either been dissipated or incorporated into the bulk of the solid mass in larger bodies. In our Solar System, this debris is predominantly generated in the Asteroid Belt and Kuiper Belt. These nearby repositories can be studied using photometry, at visible and infrared wavelengths, from the Earth and from space. This thesis aims to use high precision photometric and spectroscopic observations of (proto)planetary material at various evolutionary epochs to provide a better understanding of planet formation.

The quest for knowledge begins right here in our own celestial back yard. After 4.5 billion years of evolution, our own Solar System still contains numerous clues to its origins. The

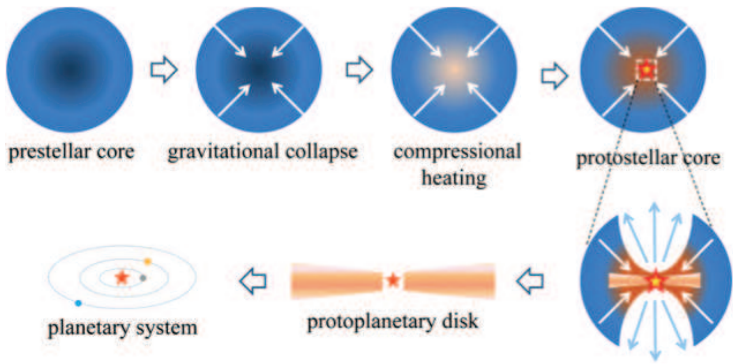

Figure 1.1: A simple cartoon of the process of star and planet formation. The collapse of a molecular cloud ultimately forms a protoplanetary disk that can become a stable stellar and planetary system. Taken from Aikawa (2013).

Kuiper and asteroid belts, for example, represent the remnants of planet formation; they are reservoirs of material that have been exposed to sunlight and dynamic interactions, but for sufficiently small bodies, have not been drastically altered as can happen during incorporation into a planet(oid). While the absolute volatile abundance is certainly not conserved, there are still patterns that can help us understand an object's origin in the protoplanetary disk and subsequent evolution. Indeed, there is a strong link between the species on the surface of icy objects and those that were present during the gas-rich disk phase (Licandro et al. 2006; Barucci et al. 2006) – and the remaining volatiles can be understood in terms of the body's thermal evolution and atmospheric escape in particular (Schaller & Brown 2007). However, we still see a great diversity in size, color, and composition of Kuiper Belt objects (KBOs) (Jewitt & Luu 2001) that warrants further study.

Levison & Morbidelli (2003) postulate that the Kuiper Belt was disrupted several hundred million years after formation (the so-called NICE model), and thus the current object locations do not necessarily indicate their primordial development. However, similarities observed in the dynamical properties of bodies can be related to a common evolutionary path. The classification of KBOs into cold classical objects versus the dynamically hot population, for example, represents observable differences in both color and location that have implications for varying origins in the protoplanetary disk. Brown et al. (2011) propose that the location of KBOs, after the disk dissipated but before the dynamical mixing described by Levison & Morbidelli (2003) occurs, determines the volatile escape from the body and thus the colors and spectra we observe.

While an overarching goal of studies of the Kuiper Belt is to use current knowledge of this population to extract their original location and molecular abundances, and tie this back to the evolution of the system as a whole, the understanding of the Kuiper Belt ultimately comes down to the study of individual objects. One of the more interesting objects discovered thus far is 2003EL61, also known as Haumea (Brown et al. 2005). It is one of the largest objects in the Kuiper Belt, with a bulk density that indicates a mostly rocky body (Rabinowitz et al. 2006; Lacerda et al. 2008; Lellouch et al. 2010). The surface reflectance spectrum indicates mostly pure water ice, perhaps with small deposits of organic material (Trujillo et al. 2007; Dumas et al. 2011). The body is dynamically and spectrally related to several other KBOs (Brown et al. 2007; Leinhardt et al. 2010) and is highly non-spherical (Rabinowitz et al. 2006; Lacerda et al. 2008). However, the precise shape and albedo is still under debate (Lacerda et al. 2008; Lacerda 2009; Lellouch et al. 2010) and further observations would benefit the physical characterization of this dwarf planet. In Chapter 2, I present unpublished observations from Hubble Space Telescope and utilize photometry and radiometry to constrain the size, shape, albedo, and density of Haumea, thus furthering the knowledge of the Kuiper Belt population.

Of course, the Solar System represents but a single outcome of the star and planet formation process. Arguably one of the most exciting scientific discoveries of the past two decades are those of the extraordinarily diverse array of extrasolar planets. Indeed, the variety of the compositions of the (exo)planets as well as the systems as a whole has led us to re-evaluate our entire understanding of planet formation. The first planets discovered were the so-called "hot Jupiters" – large planets that orbit very close to their host stars (period < 10 days) (Mayor & Queloz 1995; Butler et al. 1997). At these radii the accreting material would be predominantly gaseous, and any solid material would not be massive enough to maintain an atmosphere in the presence of stellar winds. Therefore, these planets must have migrated inwards to their current distances (Goldreich & Tremaine 1980; Lin & Papaloizou 1986). Today, the range of known systems includes massive planets further out, multiple planets in and near resonant configurations, planets with highly inclined and eccentric orbits, and a range of planetary sizes and compositions extending into the Earth mass and radius regime (Howard 2013; Batalha et al. 2013; Wright et al. 2011).

For a large portion of the planets discovered by the stellar radial velocity (RV) technique, a key physical parameter is still unknown. Stellar RV surveys have discovered hundreds of objects and are a powerful tool with one significant setback: the true mass of the planet cannot be determined, in that the RV technique only gives a lower limit on the mass of planet, $M_{\mathrm{p}} \sin i$ (where i is the inclination angle of the system, with zero degrees being face-on). Several groups have tried to use the measured minimum mass as a proxy to model the true mass distribution (Jorissen et al. 2001; Zucker & Mazeh 2001; Marcy et al. 2005; Brown 2011). However, Ho & Turner (2011) argue that the true mass of the planet cannot be trivially estimated from the minimum mass because the value of $\sin i$ is not actually drawn from the assumed isotropic distribution of the inclination. The RV technique is also biased towards more massive and close-in planets. Over the past few years the Kepler mission has afforded thousands of smaller planetary candidates at a range of orbital distances, with well known inclinations since transits are used to detect the companion (that is, the inclination must be nearly edge-on). Regardless, the large population of RV-detected planets are essential in understanding the true mass distribution. The distribution of planetary masses in all systems, as well as that around an individual star, is of particular interest to planet formation and evolution.

There is a nascent technique that has the potential to measure the motion of the planet directly, thereby solving for the planetary mass uniquely. The idea is to measure the structure of the planetary spectrum, along with the star, to get an independent radial velocity for the companion. In this sense, it is the extreme mass ratio extrapolation of stellar binary studies via spectroscopy, which have a long and highly successful history (a sample of discoveries throughout the decade: Christie & Wilson (1938); Herbig & Turner (1953); Pfeiffer (1977); Latham et al. (1988, 1992); Basri & Reiners (2006)). In the first application of this technique to extrasolar planets, Snellen et al. (2010) detected features from atmospheric CO in the well-characterized planet HD 209458 b to a precision of 2 km/s, sufficient to hint at the existence of significant winds around the planet. Brogi et al. (2012) then used the same instrumentation and analysis to detect CO on a non-transiting planet, the first detection of its kind, that was confirmed shortly thereafter by Rodler et al. (2012). These measurements allow for orbital and physical characteristics of the planet to be determined simultaneously and begin to probe atmospheric composition of non-transiting planets.

Powerful though they may be, such data are also quite difficult to attain. Both high dynamic range detections must be combined with high spectral resolution, along with a sophisticated atmospheric removal routine since many of the prominent species that shape the photospheric emission of extrasolar planetary atmospheres are also present in our own atmosphere. The Very Large Telescope (VLT) CRIRES spectrometer, used by Brogi et al. (2012), has a high resolution (R$\sim$100,000) that is well suited for these molecular detections, but a limited wavelength grasp due to both the high dispersion used and the single echelle order recorded by the optics and detectors available. Furthermore, the near-infrared wavelengths it studies capitalize on the strong rovibrational emission from the molecules we expect to be abundant both in exoplanets as well as protoplanetary disks (Tinetti et al. 2007; Swain et al. 2009; Vasyunin et al. 2008; Bergin 2011; Henning & Semenov 2013). The NIRSPEC instrument at the W.M. Keck Observatory has slightly worse resolution (R$\sim$25,000), but offers more wavelength coverage which allows for high signal-to-noise observations that are potentially sensitive to several atmospheric constituents. Using these facilities we have studied a handful of exoplanets at several epochs, providing several independent spectroscopic measurements that will be used to determine the radial velocity and then the true mass of these bodies. One object in particular, τ Boo b, has been fully analyzed and I present a detection of hot water in its atmosphere in Chapter 3.

The diversity of exoplanetary systems discovered reveal vastly different evolutionary path, ones we hope to uncover. While NICE-like models can shape outer planetary systems long after the primordial gas-rich protoplanetary disk has dissipated, many – if not most – of the salient features seen in the extrasolar planetary systems must clearly be established while significant gas is present. Thus, to place the observed diversity of extrasolar planetary systems into context, the nature of the earliest stages of planetesimal assembly and growth must be understood from both observational and theoretical perspectives.

Moving from the end stages of planet formation to the beginning, we can understand the evolution of the entire system. When a star forms from a dense molecular cloud core, the infalling gas and dust becomes a torus of material due to the conservation of angular momentum. This torus is often referred to as a proplyd, or protoplanetary disk, whose shape in the latter stages of the star-formation process is determined by the radiation from the central and nearby stars, as well as the balance of gravity and hydrostatic equilibrium of the disk material itself. Figure 1.2 provides a nice overview of the layers of a disk as well as important processes within. The disk begins with well-mixed gas and dust distributions and evolves to a state where the denser mid-plane is comprised of dust and gas with enhanced dust particle content that may be critical to the earliest stages of planetesimal accretion and growth (Dullemond et al. 2007). Ultraviolet and X-ray radiation from the central star (and accretion boundary layer) can photodissociate and ionize the molecular gas near the disk surface, and intense winds can blow away gas and particles in the inner regions of the disk. If the disk becomes sufficiently cleared, systems can result with gaps of dust and/or gas. These disks are referred to as transitional and are characterized by a spectral energy distribution, or SED, with fluxes at near-infrared (near-IR) wavelengths that are decreased relative to the longer wavelength emission or to disks with no gaps. There have been many such disks found (Merín et al. 2010; Brown et al. 2012), where a variety of processes may be responsible. Indeed, it is difficult to distinguish between a gap or hole that is cleared by the stellar-driven photoevaporation or by a growing planet without observations that can study both gas and dust and that can locate the putative edges in the disk. Recent simulations have suggested that protoplanets might also create detectable asymmetries in the gas (and dust), which could be observed using a combination of high spatial and spectral resolution techniques. Both situations have been observed in nearby disks and warrant further investigation (Isella et al. 2013; van der Marel et al. 2013). Finally, a mature planetary system is devoid of gas, other than what has been incorporated into planets, and usually has a stable planetary configuration that will persist unless perturbed, as described above for the NICE model scenario.

The classic protoplanetary disk stage – where well mixed gas and dust exist around the

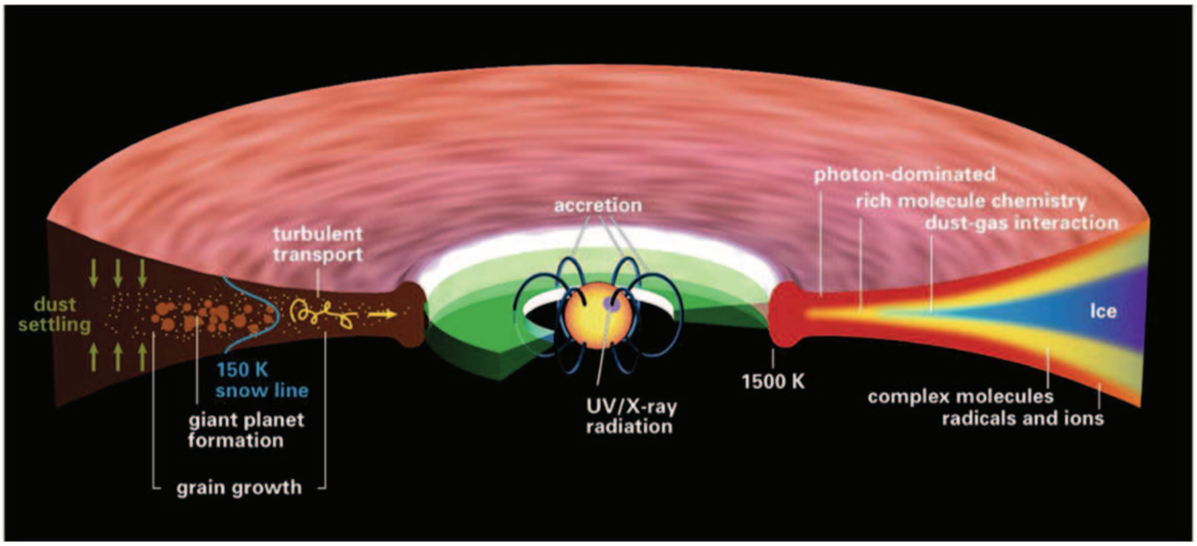

Figure 1.2: A cartoon image of a protoplanetary disk and some of the important processes and properties therein, taken from Henning & Semenov (2013).

young star – is itself highly complex. An edge-on view of the system would reveal a flared disk, where the local scale height is determined by the hydrostatic balance in the disk. Chiang & Goldreich (1997) find the scale height of the disk to increase with radius as $r^{2/7}$. This shape allows for irradiation from central star to penetrate the surface layers of the disk out to distant (>100 AU) radii. Along with the irradiation at the inner edges of the disk, this creates extensive temperature gradients that vary radially as well as vertically. Density gradients also exist in three dimensions due to the original surface density function of the disk, the natural dust settling from gravity and the viscous processes that are responsible for the inward transport of matter and the outward transport of angular momentum.

A chemical gradient follows both of these profiles in physical conditions. The surface layers, since they are directly exposed to starlight, have significant ionization fractions and are hot. Just below this layer, shielded from the harsh dissociating radiation, molecules are plentiful and a rich chemical arena results. Water, methane, carbon dioxide, hydrogen cyanide, acetylene, and many other simples species have been discovered emitting from this warm, but tenuous (as compared to the surface conditions on the Earth) region (Carr & Najita 2008; Salyk et al. 2008; Brown et al. 2013). The presence of these organic materials at planet-forming distances is of special interest to astronomers. Finally, the midplane of the disk is denser and colder than the surface layers of a passive disk (that in which accretion is sufficiently low that stellar radiation dominates the luminosity and energy budget of the system), with temperatures in the tens of Kelvin range beyond a distance of 10-20 AU. The question of turbulence in the midplane is ongoing and important (Balbus & Hawley 1991; Sano et al. 2000), but so-called “dead zones”, where the ionization is too low to drive magnetorotational instabilities, could be the key to planetesimal accretion (Flock et al. 2011; Semenov et al. 2004). Regardless, we know that planets do form and are common (Udry & Santos 2007; Batalha et al. 2013).

Hundreds of protoplanetary disks have been discovered and characterized (Strom et al. 1989; Sargent & Beckwith 1987; Kenyon & Hartmann 1995; Blake & Boogert 2004). As the birthplaces of planetary systems, the chemical make-up and dynamical processes within these disks are ultimately responsible for the variety of planetary systems found to date. To interpret the most basic properties of exoplanets, we must first begin to understand the disks from which they form, and beyond this the interactions of growing planets with their natal environment. There are many fundamental questions we seek answers to involving protoplanetary disks, among them: Given our current understanding of the nature of the so-called snow line – that suite of locations in the disk where water vapor condenses to ice – how was water delivered to the early Earth? Why is there a correlation between stellar metallicity and planet occurrence? How does disk formation and evolution affect elemental abundances and thereby the composition of planetary-mass companions? All of these questions can be addressed by studying the chemical and dynamical processes within protoplanetary disks.

Recent work on such disks has focused on developing the thermochemical models that are needed to understand disk structure. The assumption of hydrostatic equilibrium in a disk is maintained while gas and dust temperature and density distributions are exactly calculated. One of the leading new disk codes, PRODIMO (Woitke et al. 2009), fully calculates the gas and dust thermal balance using a dust continuum radiative transfer code that is coupled with gas simulations that include photochemistry, ice formation and gas phase heating and cooling processes. The authors find the gas temperature decouples from that of the dust in the surface layers of the disk and predict that it is precisely these regions where the bulk of the emission lines from CO and H_2O observed in the infrared arise. Other authors also argue for decoupling of the gas and dust temperature to explain the temperatures that characterize the rotational state distributions observed by the Herschel Space Observatory (Bruderer et al. 2012). The likelihood that grain growth and/or dust settling is a prominent feature of disks is made clear by the results of (Meijerink et al. 2009), who find that substantially enhanced gas-to-dust ratios are needed to match the water emission lines observed by the Spitzer Space Telescope. The vertical disk structure is thus a controversial, but important component in understanding emission lines.

Another prominent question concerning protoplanetary disks regards the validity of the assumption that the gas is in local thermodynamic equilibrium (LTE). While this assumption simplifies disk models greatly, it is hardly accurate as densities in the molecular layer of the disks are well below critical densities of the observed species (Dullemond & Dominik 2004). The PRODIMO group has attempted to more accurately calculate the emission lines by solving the equations of statistical equilibrium using an accelerated lambda iteration method (Woitke et al. 2009) but has not yet succeeded in matching their theoretical predictions to the suite of available data. Other non-LTE codes available include RADEX (van der Tak et al. 2007) and RADTRAN (Bruderer et al. 2012), which both incorporate an escape probability mechanism to simplify the opacity calculations in a source with large radial velocity gradients and well characterized vertical structure. Bruderer et al. (2012) also developed a thermophysical code for self-consistent thermal and chemical calculations within a protoplanetary disk and apply it to CO in HD 100546. However, the aforementioned groups focus on matching the observed rotational lines of molecules, and have not been able to reproduce rovibrational emission seen in the mid- and near-infrared. The need for a non-LTE code and its ability to accurately reproduce the available data are questions currently under examination. Toward this end, our aim is to understand the full disk structure and how this structure relates to the emission lines that have been observed from various sources. Chapter 4 presents a new non-LTE excitation code that is able to match observed line fluxes from fundamental, overtone, and isotopologue CO emission. Ultimately, a quantitative understanding of molecular abundance profiles within protoplanetary disks will define the initial conditions for planet formation, and is a critical piece of knowledge to pursue.

To conclude, I summarize the future of disk and exoplanet spectroscopy, both in terms of the continuation of this work and as a general outlook. The use of current instrumentation such as NIRSPEC and ALMA and the upcoming JWST will afford a much richer understanding of planet formation. Finally, appendices describing the codes and processes developed for this work are included for future use.

Chapter 2

The Kuiper Belt

2.1 Introduction

Haumea, one of the largest bodies in the Kuiper Belt, is also one of the most intriguing objects in this distant population. Its rapid rotation rate, multiple satellites, and dynamically-related family members all suggest an early giant impact Brown et al. (2007). Its surface spectrum reveals a nearly pure water ice surface Barkume et al. (2006); Trujillo et al. (2007); Merlin et al. (2007); Dumas et al. (2011), with constraints on other organic compounds with upper bounds $< 8\%$ Pinilla-Alonso et al. (2009). Lacerda et al. (2008) also find evidence for a dark spot on one side of the rotating body, make the surface albedo non-uniform. Even more interesting is that shape modeling has suggested a density higher than nearly anything else known in the Kuiper belt and consistent with a body almost thoroughly dominated by rock Rabinowitz et al. (2006),Lacerda et al. (2008),Lellouch et al. (2010). Lacerda & Jewitt (2007) concluded a density of 2.551 g cm^{-3} and follow up work found consistent values between 2.55 and 2.59 g cm^{-3}, depending on the model used. Such a rocky body with an icy exterior could be a product of initial differentiation before giant impact and subsequent removal of a significant amount of the icy mantle. Leinhardt et al. (2010) demonstrate that such an impact is possible in a graze and merge collision between equal size bodies, and are able to reproduce the properties of the Haumea family system.

Much of our attempt at understanding the history of Haumea relies on the estimate of the high density of the body. Haumea's large-amplitude light curve and rapid rotation have been used to infer an elongated shape for the body. Assuming that the rotation axis lies in the same plane as the plane of the satellites, the amplitude of the light curve then gives a ratio of the surface areas along the major and minor axes of the bodies. If the further assumption is made that Haumea is large enough to be in hydrostatic equilibrium, the full shape can be uniquely inferred to be a Jacobi ellipsoid with fixed ratios of the three axes. From this shape and from the known rotation velocity, the density is precisely determined. Finally, with the mass of Haumea known from the dynamics of the two satellites Ragozzine & Brown (2009), the full size and shape of Haumea is known Rabinowitz et al. (2006),Lacerda et al. (2008),Lellouch et al. (2010).

The major assumption in this chain of reasoning is that Haumea is a figure of equilibrium. While it is true that a strengthless body can instantaneously have shapes very different from figures of equilibrium Holsapple (2007), long-term deformation at the pressures obtained in a body this size should lead to essentially fluid behavior, at least at depth. Indeed, any non-spinning body large enough to become round due to self-gravity has attained the appropriate figure of equilibrium. While the size at which this rounding occurs in the outer solar system is not well known, the asteroid Ceres, with a diameter of 900 km is essentially round Millis et al. (1987),Thomas et al. (2005), while among the icy satellites, everything the size of Mimas and larger ($\sim$400 km) is essentially round. It thus seems reasonable to assume that a non-spinning Haumea, with a diameter of $\sim$1240 km Lellouch et al. (2013),Fornasier et al. (2013) would be round, thus a rapidly-spinning Haumea should likewise have a shape close to that of the Jacobi ellipsoid defined by Haumea's density and spin rate.

Nonetheless, given the importance of understanding the interior structure of Haumea and the unusually high density inferred from these assumptions, we find it important to attempt independent size and density measurements of this object. Here we use unpublished photometric data from the Hubble Space Telescope (HST) to determine a best-fit Jacobi ellipsoid model. We then compare the predicted thermal flux from this best-fit Jacobi ellipsoid to thermal flux measured from the Spitzer Space Telescope(first presented in Stansberry et al. (2008)) and consider these constraints on the size and shape of the body.

2.2 Observations

Haumea was imaged on 2009 February 4 using the PC chip on the Wide Field/Planetary Camera 2 on HST. We obtained 68 100s exposures using the F606W filter, summarized in Table 1. The observations were obtained over 5 consecutive HST orbits, which provides a full sample of Haumea's 3.9154 hr rotational lightcurve Rabinowitz et al. (2006). With a pixel scale of ~5500 km at the distance of Haumea and semi-major axes of ~50,000 km and ~25,000 km for Hi'iaka and Namaka, respectively Ragozzine & Brown (2009), this is the first published dataset where the object is resolved from its satellites, providing a pure lightcurve of the primary. During the observation, both satellites are sufficiently spatially separated from the primary that we are able to perform circular aperture photometry. Basic photometric calibrations are performed on the data including flat fielding, biasing, removing charge transfer efficiency effects, and identifying and removing hot pixels and cosmic rays[1]. In five of our images the primary is contaminated by cosmic rays so we do not include these data. A 0.5" aperture is used to measure the object, and we apply

---

[1] see the WFPC2 handbook at http://www.stsci.edu/instruments/wfpc2/Wfpc2_dhb/WFPC2_longdhbcover.html

an infinite aperture correction of 0.1 magnitudes Holtzman et al. (1995). We present and model the data in the STMAG magnitude system, but a convolution of the F606W filter with the Johnson V filter shows a difference of approximately 0.1 magnitudes. This difference, along with the satellite flux contributions of 10% Ragozzine & Brown (2009) included in previous photometry of the dwarf planet, indicate that the magnitude and amplitude of the lightcurve presented here(Δm = 0.32) is consistent with the findings of Rabinowitz et al. (2006) (Δm = 0.28) and Lacerda et al. (2008) (Δm = 0.29). The rotational period of Haumea is known sufficiently precisely that all of the observations are easily phased. We combine our data with that of Rabinowitz et al. (2006) and Lacerda et al. (2008) to get a 4-year baseline of observations and find a period of 3.91531 ± 0.00005 hours using phase dispersion minimization Stellingwerf (1978). This period is consistent with that of Lellouch et al. (2010) (P = 3.915341 ± 0.000005 h derived from a longer baseline), whose more precise solution we use to phase all observations, visible and infrared. With this period, there is a 60s uncertainty in the phasing over the 1.5 years between observations. We define a phase of 0 to be the point of absolute minimum brightness of Haumea and define a longitude system in which $\lambda = [(JD - 2454867.042]$ modulo 360 degrees. This result is given in JD at Haumea, which is consistent with the phased data of Lacerda et al. (2008), and Lellouch et al. (2010) who instead quote their phasing in JD at the Earth. The photometric results are shown in Fig. 2.1.

The thermal radiometry of Haumea was obtained 2007 July 13 – 19 using the 70 micron band of the MIPS instrument Rieke et al. (2004) aboard the Spitzer Space Telescope (SST). Haumea's lightcurve was unknown at the time, and the objective of the observations was simply to detect the thermal emission at a reasonably high signal to noise ratio (SNR). The data were collected as three 176 minute long observations, each of which is nearly as long as the (now known) lightcurve period. Stansberry et al. (2008) published the flux obtained by combining all three observations, as well as models indicating a diameter of about 1150 ± 175 km. Contemporaneously, Haumea's lightcurve was published Lacerda et al. (2008), a result that led us to consider re-analysing the Spitzer data to try and detect a thermal lightcurve. To that end, we split the original 176 minute exposures (each made up of many much shorter exposures) into 4 sub-observations, each 44 minutes long. The resulting data was processed using the MIPS Instrument Team pipeline Gordon et al. (2005), resulting in flux calibrated mosaics for each of the 12 sub-observations. These individual observations are presented in Table 2. One of the points was obviously discrepant and was removed from the analysis. The data were also re-processed using improved (relative to the 2007 processing published in Stansberry et al. (2008)) knowledge of Haumea's ephemeris. The reprocessing was undertaken as part of a project to reprocess all Spitzer/MIPS observations of TNOs (described in Mommert et al. (2012)) and is key to obtaining the highest SNR from the data. Had Haumea's lightcurve been known at the time the Spitzer observations were planned, the observations probably would have been taken, for example, as a series of about 10 approximately 60 min exposures spaced about 4.1 rotations apart. The non-optimal observation plan may in part explain why the the uncertainties on the flux measurements appear to be somewhat optimistic, as discussed in more detail below.

The motion of Haumea was significant over the 6-day observing interval, so we were able to make a clean image of the background sources (i.e., one without contamination from Haumea), and then subtract that sky image from our mosaics. The procedure used has been described previously, e.g., by Stansberry et al. (2008). We performed photometry on the sky-subtracted images, obtaining significantly smaller uncertainties than was possible using the original mosaics. The raw photometry was corrected for the size of the photometric aperture

(15" radius). The signal-to-noise ratio of the resulting detections was about 7 in each of the 12 epochs. An additional calibration uncertainty of 6% should be systematically applied to the entire dataset. The thermal results are shown in Fig. 1. Where multiple observations are made at the same phase, these observations are averaged, and the uncertainty is taken from the standard deviation of the mean (or the full range if only two points go into the mean).

Though the uncertainties are large, the thermal light curve appears in-phase with the measured visible light curve. To robustly ascertain the detection of a thermal lightcurve, we look for a correlation between the thermal and visible datasets. We compare the mean visible flux during the phase of each 44 minute long thermal observation with the measured thermal flux during that observation (Fig. 2.2). A linear fit to the data suggests that a positive correlation between the optical and thermal brightness. As noted above, the deviation of the measurements from the model are larger than expected, so we assess the significance of the correlation between the optical and thermal data using the non-parametric Spearman rank correlation test Spearman (1904). With this test, we find that the two data sets are correlated at the 97% confidence level, and that the correlation is positive, that is: the observed optical and thermal flux increase and decrease in phase and there is only a 3% chance that this phase correlation is random. This positive correlation between the thermal and visible data sets indicates that we are viewing an elongated body and that the visible light curve must be caused – at least in part – by the geometric effects of this elongated body.

Table 2.1: HST F606W flux of Haumea

JD -2450000	phase (deg)	F606W mag	uncertainty	JD -2450000	phase (deg)	F606W mag	uncertainty
4866.943802	142.27	17.863	0.004	4867.0898	104.08	17.689	0.003
4866.945802	146.87	17.865	0.004	4867.0918	108.68	17.707	0.003
4866.948202	151.47	17.887	0.004	4867.0937	113.28	17.717	0.003
4866.950202	156.06	17.897	0.004	4867.0962	117.88	17.740	0.003
4866.952102	160.66	17.913	0.004	4867.0981	122.47	17.753	0.003
4866.954602	165.26	17.923	0.004	4867.1025	131.67	17.808	0.004
4866.956502	169.86	17.935	0.004	4867.1435	222.08	17.847	0.004
4866.958502	174.45	17.926	0.004	4867.1455	226.68	17.815	0.004
4866.960402	179.05	17.930	0.004	4867.1474	231.28	17.793	0.004
4866.962902	183.65	17.931	0.004	4867.1494	235.87	17.772	0.004
4866.964802	188.24	17.922	0.004	4867.1518	240.47	17.751	0.003
4866.966802	192.84	17.927	0.004	4867.1538	245.07	17.741	0.003
4866.971202	202.04	17.907	0.004	4867.1557	249.66	17.731	0.003
4867.010702	289.39	17.772	0.004	4867.1577	254.26	17.723	0.003
4867.012702	293.98	17.795	0.004	4867.1601	258.86	17.725	0.003
4867.014602	298.58	17.802	0.004	4867.1621	263.46	17.718	0.003
4867.017102	303.18	17.825	0.004	4867.1640	268.05	17.727	0.003
4867.019002	307.77	17.862	0.004	4867.1660	272.65	17.723	0.003
4867.021002	312.37	17.887	0.004	4867.1684	277.25	17.743	0.003
4867.022902	316.97	17.913	0.004	4867.1704	281.85	17.747	0.003
4867.025402	321.57	17.931	0.004	4867.2143	18.39	17.925	0.004
4867.027302	326.16	17.935	0.004	4867.2163	22.99	17.904	0.004
4867.029302	330.76	17.954	0.004	4867.2182	27.58	17.884	0.004
4867.031202	335.36	17.963	0.004	4867.2202	32.18	17.873	0.004
4867.035602	344.55	17.973	0.004	4867.2226	36.78	17.847	0.004
4867.075202	71.90	17.695	0.003	4867.2265	45.97	17.801	0.004
4867.077102	76.50	17.664	0.003	4867.2285	50.57	17.768	0.004
4867.079602	81.10	17.664	0.003	4867.2309	55.17	17.748	0.003
4867.081502	85.69	17.655	0.003	4867.2329	59.77	17.724	0.003
4867.083502	90.29	17.671	0.003	4867.2348	64.36	17.713	0.003
4867.085402	94.89	17.671	0.003	4867.2368	68.96	17.697	0.003
4867.087902	99.49	17.674	0.003				

Table 2.2: Thermal Flux of Haumea

JD - 2450000	phase (deg)	MIPS 70 μm flux (mJy)	uncertainty (mJy)
4294.6770	194.5	14.77	1.88
4294.7367	326.1	12.58	1.98
4294.7664	31.9	11.67	1.53
4297.4004	84.9	18.51	2.02
4297.4302	150.0	7.61	1.47
4297.4601	216.0	13.86	1.55
4297.4899	281.8	15.86	1.64
4300.4980	79.1	16.18	1.84
4300.5277	145.4	14.24	1.79
4300.5576	211.4	13.69	1.55
4300.5874	277.1	20.14	2.35

2.3 Photometric model

We begin with the assumption that Haumea is indeed a Jacobi ellipsoid whose shape is defined by its density and spin period. To find the Jacobi ellipsoid which best fits the photometric data, we model the expected surface reflection from an ellipsoid by creating a mesh of 4,000 triangular facets covering the triaxial ellipsoid and then determining the the total visible light from the sum of the light reflected back toward the observer from each facet. Facets are approximately equal-sized equilateral triangles with length equal to 5 degrees of longitude along the largest circumference of the body. Mesh sizes a factor of 2 larger or smaller give identical results. For each facet we use a Hapke photometric model Hapke (1993) to determine the reflectance as a function of emission angle. This model accounts for the effects of low phase angle observations, such as coherent backscattering and shadow hiding, and has been used to model the reflectance of many icy surfaces. For concreteness, we adopt parameters determined by Karkoschka (2001) for Ariel, a large satellite which exhibits deep water ice absorption and a high geometric albedo. We utilize the published values for the mean surface roughness($\bar{\theta} = 23°$), single-scattering albedo ($\varpi = 0.64$), asymmetry parameter($g = -.28$), and magnitude($S(0)$) and width(h) of the coherent backscattering and shadowing functions, $S(0)_{CB} = 4.0$, $h_{CB} = 0.001$, $S(0)_{SH} = 1.0$, and $h_{SH} = 0.025$ Karkoschka (2001) . While we have chosen Ariel because it is perhaps a good photometric analog to Haumea, we do note that within the range of Hapke parameters of icy objects throughout the solar system ($\varpi \sim 0.4 - 0.9$, $g = -.43 - -.17$, $\bar{\theta} = 10 - 36°$), including the icy Galilean satellites and Triton Buratti (1995),Hillier et al. (1990), the precise parameters chosen will affect only the geometric albedo and the beaming parameter, as discussed below.

The visible flux reflected from the body then becomes:

$$F_{vis} = p_{vis} \frac{F_{\odot,606}}{{R_{AU}}^2} A \frac{H \cos e}{\pi \Delta^2} \tag{2.1}$$

where p_{vis} is the visual albedo, $F_{\odot,606}$ is the solar luminosity over the bandwidth of the F606W filter, A is the projected surface area, H is the Hapke reflectance function, e is the angle of incidence, Δ is the geocentric distance to the body, and R is the heliocentric distance.

Our modeled body is rotated about the pole perpendicular to our line of sight – consistent with the hypothesis that the rotation pole is similar to the orbital pole of the satellites – and the photometric light curve is predicted. For such a model, the peak and trough of the visible lightcurve correspond to the largest and smallest cross-sectional areas of the body, and the ratio of the length of the largest non-rotational axis (a) to the smallest non-rotation axis (b), controls the magnitude of the photometric variation. With a uniform albedo across the surface of Haumea, however, no triaxial ellipsoid can fit the asymmetric observed lightcurve. We confirm the assertion of Lellouch et al. (2010) that the photometric variations of Haumea are caused primarily by shape and that surface albedo variations add an only minor modulation. In this approximation, the brightest peak and brightest trough of the data are assumed to be from essentially uniform albedo surfaces and are modeled to determine the ratio of the axes of the body. For plausible values of the dimension of the rotational axis (c), the measured peak-to-trough amplitude in the lightcurve of $\Delta m = 0.32 \pm 0.006$ is best modeled with an axis ratio of $b/a = 0.80 \pm 0.01$. Using the brightest trough and darkest peak instead, the axial ratio would be b/a = 0.83, but the surface heterogeneity necessary for this assertion is less likely than the single darker spot proposed here and observed by others Lacerda et al. (2008).

Our measured value of 0.80 differs from previous measurements of b/a of .78 Rabinowitz et al. (2006) and .87 Lacerda et al. (2008) for a number of reasons. Our visible dataset resolves Haumea from its satellites which results in a slightly deeper lightcurve. More to the point, including a realistic surface reflectance model changes that estimated shape significantly. Rabinowitz et al. (2006) do not actually model the shape of the body, while Lacerda et al. (2008) assume the surface to be uniformly smooth, giving a value for b/a that is too high. More recently, Lellouch et al. (2010) confirm a more elongated body (b/a = .80), after having tested two different models, including that of Lacerda et al. (2008).

With the ratio of the axes fixed, we now find the simplest surface normal albedo model consistent with the data. We divide the surface longitudinally into 8 slices and allow the albedo to vary independently between sections to account for the possible hemispherical variation apparent in our data and explored by others Lacerda et al. (2008),Lacerda (2009). Dividing the surface further does not significantly improve the fit. The middle panel of Figure 2.1 shows how the geometric albedo varies across the surface of the body.

Assuming that Haumea is indeed a Jacobi ellipsoid, the ratio $b/a = 0.80$ combined with the rotation period uniquely defines $c/a = 0.517$ and a density of 2.6 g cm^{-3}. Combining these parameters with the known mass of Haumea from Ragozzine & Brown (2009) implies $a = 960$ km, $b = 770$ km, and $c = 495$ km. These radii agree with the ones obtained by Lellouch et al. (2010) using a Lommel-Seelinger reflectance function.

2.4 Thermal model

To calculate the thermal emission from our shape and albedo model we first determine the temperature of each facet of the body. Due to Haumea's rapid rotation, the temperature of any given face of the surface does not have time to equilibrate with the instantaneous incoming insolation. Instead, we calculate the average amount of sunlight received by a facet during a full rotation, which is only dependent on the angle between rotational pole and the facet normal. Although we implement a standard thermal model, the rapidly spinning object gives rise to surface temperatures indicative of an isothermal latitude model Stansberry et al. (2008), which we precisely calculate for the non-spherical geometry of the object. Indeed the agreement between the visible and infrared datasets as seen in Figure 2.2 supports the hypothesis of a body with negligible thermal conductivity.

We model the average amount of sunlight absorbed for each facet by multiplying the geometric albedo of each facet by an effective phase integral q and averaging over a full rotation. The average facet phase integral is a mild function of the shape of the body, but for simplicity, we simply adopt a value of $q = 0.8$, as used by Stansberry et al. (2008) for large, bright KBOs. In fact, the precise value used has little impact on our final results.

If we assume the surface is in thermal equilibrium, the temperature of each facet, is determined by balancing this absorbed sunlight with the emitted thermal radiation. We choose a typical thermal emissivity of 0.9 and invoke a beaming parameter, η, which is a simple correction to the total amount of energy radiated in the sunward direction, usually

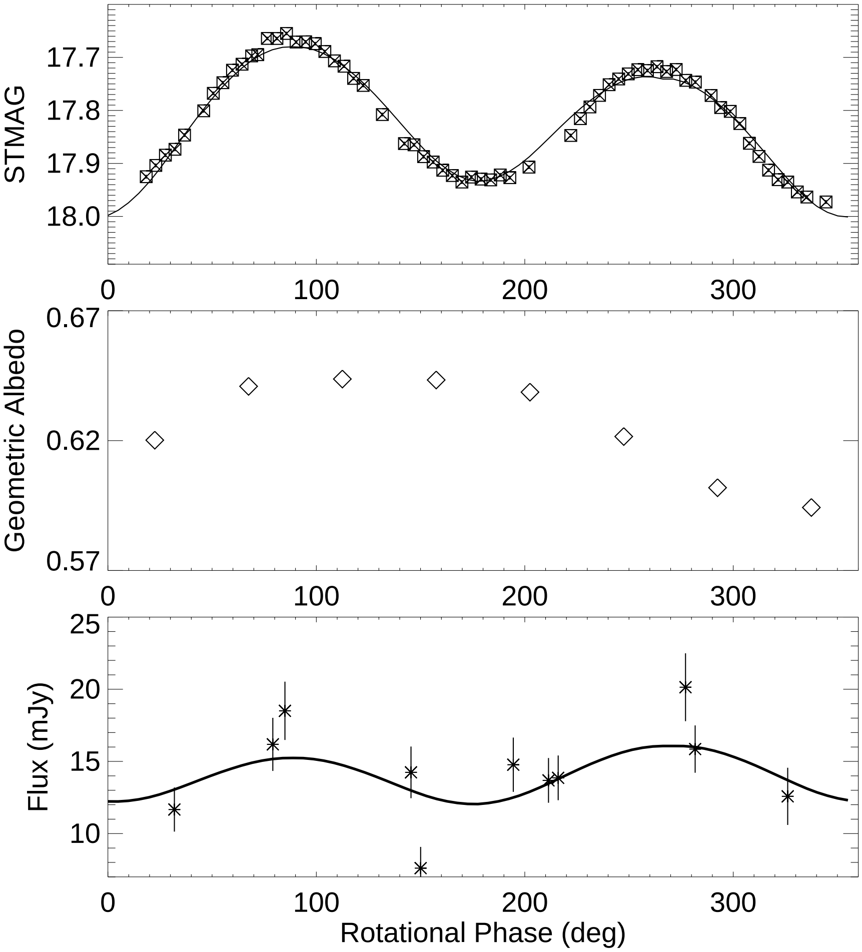

Figure 2.1: The visible lightcurve, geometric albedo, and thermal lightcurve of Haumea plotted over one rotation. The error bars in the top two panels are smaller than the size of the plotted point. The visible photometry are fit with a Jacobi ellipsoid of dimensions 1920 x 1540 x 990 km with the modest longitudinal variation in reflectance shown. This ellipsoid model provides an excellent fit to the 70 μm thermal data from Spitzer.

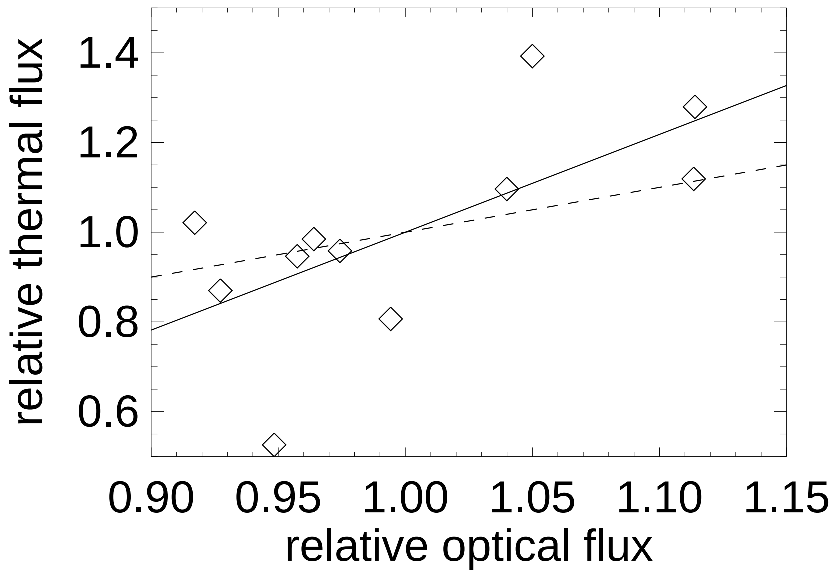

Figure 2.2: Correlation of the optical and thermal flux. The dashed line shows a one-to-one correlation, while the solid line shows the best fit. A rank correlation test shows that the two distributions are correlated at the 97% confidence level. The in-phase thermal light curve of Haumea demonstrates that it is an elongated body.

assumed to be caused by surface roughness, but which can be taken as a generic correction factor to the assumed temperature distribution. For asteroids of known sizes, Lebofsky et al. (1986) found η to be approximately 0.756, a correction which agrees well with measurements of icy satellites in the outer solar system Brown et al. (1982a),Brown et al. (1982b). The beaming parameter value range for Trans-Neptunian objects is fully described in Lellouch et al. (2010), who found η of 1.15-1.35 for Haumea, with hemispherical variations consistent with a much lower value ($\eta \sim .4$-$.5$). The MIPS and PACS fluxes values presented in Lellouch et al. (2010) were updated and presented in Fornasier et al. (2013), who, also using the SPIRE data, found a beaming factor of $0.95^{0.33}_{-0.26}$ with a NEATM model. We leave this as a free parameter in our modeling, but consider an inclusive range.

For each rotational angle of our model, we predict the total thermal flux by calculating the blackbody spectrum from each visible facet and integrating this flux in the full 70 μm band pass of MIPS, according to

$$F_{IR} = \frac{A \cos e}{\pi^2 \Delta^2} \epsilon \int B_\lambda(T(\theta, \phi)) \sin\theta d\theta d\phi \tag{2.2}$$

where A is the cross-sectional surface area, $\epsilon = 0.9$ is the emissivity, B is the Planck function and T is the temperature at each piece of the surface. Assuming a solar flux at 70 μm of S at the distance of Haumea, R, then T is calculated for an edge-on rotating body and

$$T = [\frac{S * (1 - qp_{vis})}{\epsilon\sigma\eta R^2}]^{1/4} \tag{2.3}$$

Figure 2.1 shows the measured Spitzer flux along with the flux predicted from a model for the theoretical Jacobi ellipsoid with $a = 960$ km and $a : b : c = 1.00 : 0.80 : 0.52$ and a thermal beaming parameter of $\eta = 0.76$. The best fit is obtained by assuming $\eta = 0.89$, but values of η between 0.82 and 0.97 are within the 1-σ error limits. The larger values measured by Lellouch et al. (2010) and quoted for the majority of Kuiper Belt objects (~1.2 by Stansberry et al. (2008) and ~ 1-2.5 by Lellouch et al. (2013)) are consistent with our result if we consider the difference of thermal models employed. Stansberry et al. (2008) explain that the surface temperature difference between an isothermal latitude model (that is used in this work) and a standard thermal model (used by Lacerda (2009) and Lellouch et al. (2010) is simply a factor of $\pi^{-\frac{1}{4}}$. If this value is incorporated into the beaming factor, the inconsistency between the models and resulting beaming parameters is resolved. Remarkably, the shape and albedo model constructed from only photometric observations and the assumption of fluid equilibrium, provides an acceptable prediction of the total thermal flux at 70 μm and its rotational variation.

2.5 Discussion

The thermal and photometric light curves of Haumea are consistent with the assumption that Haumea is a fluidly relaxed, rapidly rotating Jacobi ellipsoid with a density of 2.6 g cm^{-3} and minor albedo variation across its surface. Although we allow the albedo to change longitudinally, we have demonstrated that the reason for the double-peaked lightcurve of Haumea is in fact a shape effect. This work presents new data and an informed Hapke model that agree with the findings of previous authors Lellouch et al. (2010)Lacerda et al. (2008)Rabinowitz et al. (2006).

The lightcurve in several colors Lacerda et al. (2008)Lacerda (2009) indicates that the albedo variation is concentrated in a large spot on one side of the body, an argument supported by our allowed albedo variation. The precise geometric albedo presented here is less than that of Fornasier et al. (2013), but with a small variation in either the single-scattering albedo or the asymmetry parameter, we easily find agreement between the two values. We do not focus on the absolute value of the albedo here, as it is closely tied to the unknown Hapke parameters for the surface. The only affect this has on the thermal fit is to change the best fit beaming parameter, which does not differ by more than 1-σ from the reported value. The important point here, however, is that our precise visible data set agrees with the dark spot proposed by Lacerda et al. (2008).

There are still a number of questions remaining regarding this KBO. The temperature of the dark spot is still uncertain and our data are not precise enough to constrain it, although the lower albedo we use to match the visible data agree well with a warmer region. Another assumption used here that could be disputed is the rotation axis of the body as perpendicular to our line of sight. However, assuming that the majority of the depth of the light curve is from the major axes of the body, the pole position will only affect the size of the third dimension of the body and the thermal beaming factor, which become somewhat degenerate when fitting the thermal data anyway. If the body were not mostly edge-on, it would be difficult to explain the particular surface patterning needed to recreate the visible lightcurve.

While it is encouraging that a dense Jacobi ellipsoid fits both data sets, it is important to point out that we can only obtain a unique solution under the assumption that the object has a prescribed shape. If Haumea is modeled as an arbitrary triaxial ellipsoid rather than a Jacobi ellipsoid, large families of solutions are possible. To first order, the photometric data constrain the ratio b/a, while the thermal flux is roughly proportional to the emitting surface area which is proportional to ac and bc. As long as the ratio of b/a is kept constant, however, equally good fits can be obtained from very elongated ellipsoids with a very short rotation axis, or from only moderately elongated ellipsoids with a large rotation axis, as long as the value ac is approximately constant. For this unconstrained problem, densities anywhere between 1 g cm^{-3} (for very elongated objects) and 3 g cm^{-3} for compact objects are compatible with both data sets. While such large deviations from an equilibrium shape appear implausible, the thermal data alone cannot rule them out.

Chapter 3

Exoplanets

3.1 Introduction

Since the first detection of an exoplanet around a main-sequence star (Mayor & Queloz 1995), astronomers have discovered hundreds of exoplanets using the radial velocity (RV) technique (Wright et al. 2012). This powerful tool for discovering exoplanets only measures the minimum, or "indicative" mass, $M_{\rm p} \sin i$, leaving a degeneracy between two interesting properties of the system, one physical and one orbital. While the indicative mass is useful for statistical studies, uniquely measuring the true mass of an exoplanet not only yields a key physical property, but also furthers our understanding of planetary formation and evolution via measurement of true mass distribution of exoplanets (Zucker & Mazeh 2001; Weiss et al. 2013). Additionally, indicative masses can only provide a measure of a planet's true mass if the underlying true mass distribution is known. For example, Ho & Turner (2011) demonstrate that knowledge of the true mass distribution is necessary to convert a minimum mass, $M_{\rm p} \sin i$, into an estimate of a planet's true mass for RV-detected systems.

One class of objects for which the planet mass can be directly determined are those that transit their host star. Hundreds of transiting planets have been discovered and characterized, and the ongoing *Kepler* mission has found potential exoplanet candidates numbering in the thousands (Borucki et al. 2011; Batalha et al. 2013). Transit events also provide atmospheric information through transmission spectroscopy and secondary eclipses. Investigators have measured spectra of some of the larger transiting planets (Charbonneau et al. 2002), leading to the discovery of species such as water, methane and carbon monoxide (Knutson et al. 2012; Berta et al. 2012; Crossfield et al. 2013; Baskin et al. 2013). A variety of spectral retrieval methods have been used to verify the results, confirming the hypothesis that O- and C-bearing gases are present in the atmospheres of hot Jupiters (Madhusudhan & Seager 2009; Line et al. 2012).

Recently, a technique previously used to detect low mass ratio, spectroscopic binary stars has been applied to stars known to host exoplanet systems. The direct RV detection of an exoplanet involves separating the planetary and stellar components spectroscopically. The high flux ratio between the primary and companion makes these detections difficult, but not impossible, thanks to modern infrared echelle spectrographs on 8-10m class telescopes. Snellen et al. (2010) detected CO on HD 209458 b with a precision of 2 km/s using the R$\sim$100,000 Very Large Telescope CRIRES instrument. This detection provided the spectroscopic orbit of the system and determined the true mass of the planet. Although some of the properties of the system had been measured more precisely from transit observations (Henry et al. 2000; Charbonneau et al. 2000), Snellen et al. (2010) demonstrated the ability to directly detect the RV of an exoplanet.

Indeed, this technique can be applied to non-transiting, RV-detected exoplanets to extract the unknown inclination and true mass. CRIRES was also used to detect CO on τ Boötis b (Brogi et al. 2012), the first ground-based detection of a short-period non-transiting exoplanet atmosphere, a result confirmed shortly thereafter by Rodler et al. (2012). These studies provide the true mass of the planet and probe the chemical composition of its atmosphere. The sensitivity required to extract the planetary signal is such that these detections were made possible only by combining several CO overtone lines and the high resolution available.

Despite the agreement between the two groups, the direct detection of exoplanets, especially τ Boo b, has a storied history. Collier Cameron et al. (1999) first reported a detection of reflected light from τ Boo b more than a decade ago and Wiedemann et al. (2001) reported a possible detection of CH_4 in the planet's atmosphere soon thereafter, using the same orbital solution. However, the planetary velocity from the earlier results disagrees with more recent findings discussed above.

Here we report a detection of water vapor in the atmosphere of τ Boo b, using spectroscopic observations centered around 3.3 μm. The τ Boötis system is a stellar binary comprised of a F-type 'A' component and a M-dwarf 'B' component. The hot Jupiter τ Boo b orbits the larger 'A' component with a period of 3.312 days and a minimum (indicative) mass $\mathrm{M}\sin i = 3.87\mathrm{M}_{Jup}$ (Butler et al. 1997). Our detection confirms the mass determined by Brogi et al. (2012) and serves to further characterize the atmospheric chemistry of this exoplanet. Data from five epochs reveal orbital motion of τ Boo b that is consistent with that reported by Brogi et al. (2012). The planetary template spectrum used in the cross-correlation is dominated by water vapor opacity, providing strong evidence of water in the atmosphere of a non-transiting hot Jupiter for the first time.

3.2 Methods

3.2.1 Observations and Data Reduction

We observed the τ Boo system on five separate nights in March 2011, May 2011, and April 2012 (Table 3.1), chose to optimize phasing near orbital quadrature, allowing for maximum separation of stellar and planetary lines. We use the Near Infrared Echelle Spectrograph (NIRSPEC) (McLean et al. 1995) at the W.M. Keck Observatory, which provides high resolution (R $\sim$ 25,000 for a 3-pixel slit) in multiple orders at the wavelengths of interest to study near-infrared water emission. We obtained spectra covering 3.404-3.457 μm, 3.256-3.307 μm, 3.121-3.170 μm, and 2.997-3.043 μm. Each epoch covers a total elapsed time of approximately one hour, and is comprised of a continuous sequence of hundreds of exposures.

We extract NIRSPEC spectra using a custom Interactive Data Language (IDL) optimal extraction pipeline, similar to that described by Cushing et al. (2004). The spatial profile weighting intrinsic to optimal extraction provides a reliable method for detecting and removing bad pixels due to detector defects and cosmic rays. It adjusts for seeing variations that occur over the course of an observation, and can also minimize the contamination from nearby stars that happen to fall on the slit. We have determined that the contamination from the M-dwarf companion τ Boo B is negligible in all epochs of our extracted τ Boo A spectra. Arc lamps typically used for wavelength calibration do not provide useful reference lines in the thermal infrared. Instead, we wavelength calibrate our spectra using unblended telluric features with accurately known rest wavelengths. Between 15 and 30 individual telluric lines are used for each order.

We first correct the bulk telluric absorption with TERRASPEC (Bender et al. 2012), a synthetic forward-modeling algorithm that uses the line-by-line radiative transfer model

Table 3.1: L-band observations of Tau Boo b

Date	JD - 2450000	Phase (rad)	$V_{barycentric}$ (km/s)
21 May 2011	5702.8542	0.3199	17.36
03 Apr 2012	6021.0625	0.3847	-2.26
01 Apr 2012	6019.0625	0.7810	-3.02
14 Mar 2011	5634.9375	0.8164	-11.75
24 Mar 2011	5644.9375	0.8353	-7.39

LBLRTM (Clough et al. 2005) to generate a synthetic absorption function for the Earth's atmosphere (hereafter, TAF). The TAF includes continuum absorption and line absorption for 28 molecular species, with line information provided by the HITRAN 2008 database (Rothman et al. 2009). Vertical mixing profiles for the seven most prominent species (H_2O, CO_2, O_3, N_2O, CO, CH_4, and O_2) can be scaled or adjusted from the LBLRTM default profiles, which include the US Standard 1976, tropical, midlatitude, and subartic models. These models represent the average atmosphere for their respective latitudes (in 1976), which is a good initial guess for the instantaneous atmosphere corresponding to a single observation. We use the tropical model to provide initial vertical profiles for spectroscopy obtained from Mauna Kea.

TERRASPEC convolves the TAF with an instrumental broadening profile (hereafter, IP), which is measured from the data. The IP is parameterized as a central Gaussian surrounded by satellite Gaussians offset by a fixed percentage of the Gaussian width, and with adjustable amplitudes. This is similar to the IP parameterization described by Valenti et al. (1995) for use with I_2 absorption cells. Typically 2-4 satellite Gaussians serve to model the IP. The instrumental broadened TAF is then multiplied by a low-order wavelength dependent polynomial to correct for the combined effects of blaze sensitivity and stellar continuum. TERRASPEC uses the least-squares fitting algorithm `MPFIT` (Markwardt 2009) to optimize the parameters comprising the TAF, IP, and continuum. The FWHM of the profile is consistently $1.3 \times 10^{-4}\mu$m, which yields $R = \lambda/\Delta\lambda = 24,000$. Spectral regions containing stellar absorption are excluded from the optimization by adaptive masks.

The initial telluric correction can be significantly affected by the instrumental fringing. We therefore mask strong stellar lines from the telluric corrected spectrum, and analyze the remaining spectral range with a Lomb-Scargle periodogram (Scargle 1982) to measure the frequency and power of the individual fringes present in our spectra. Two prominent fringes are seen at ∼1.75 cm^{-1}and 2.18 cm^{-1}. We then calculate the composite fringe function as the product of the individual fringes, and divide it into the non-telluric-corrected spectrum. The defringed spectrum is then reprocessed with TERRASPEC, yielding the telluric-free and continuum-normalized stellar spectrum, a measurement of the TAF, and a parameterization of the IP. This process was often iterated 2-3 times to ensure full removal of fringing and telluric absorption. Regions with atmospheric transmission ≤40% of the continuum value, determined from the TAF, are masked and excluded from the final planet search. Figure 3.1 shows the telluric removal process, resulting in spectra with noise levels comparable to those presented in Rodler et al. (2012).

3.2.2 Two-Dimensional Cross Correlation

Next we use a two-dimensional cross correlation analysis, TODCOR (Zucker & Mazeh 1994), to simultaneously extract the planetary and stellar velocity shifts. We generated a synthetic stellar model of the τ Boo A spectrum using a recent version of the LTE line analysis code MOOG (Sneden 1973) and the MARCS grid of stellar atmospheres (Gustafsson et al. 2008). The input linelist was created by detailed matching of a synthetic solar spectrum to the ATMOS ATLAS-3 infrared solar spectrum (Abrams et al. 1996), starting from the solar

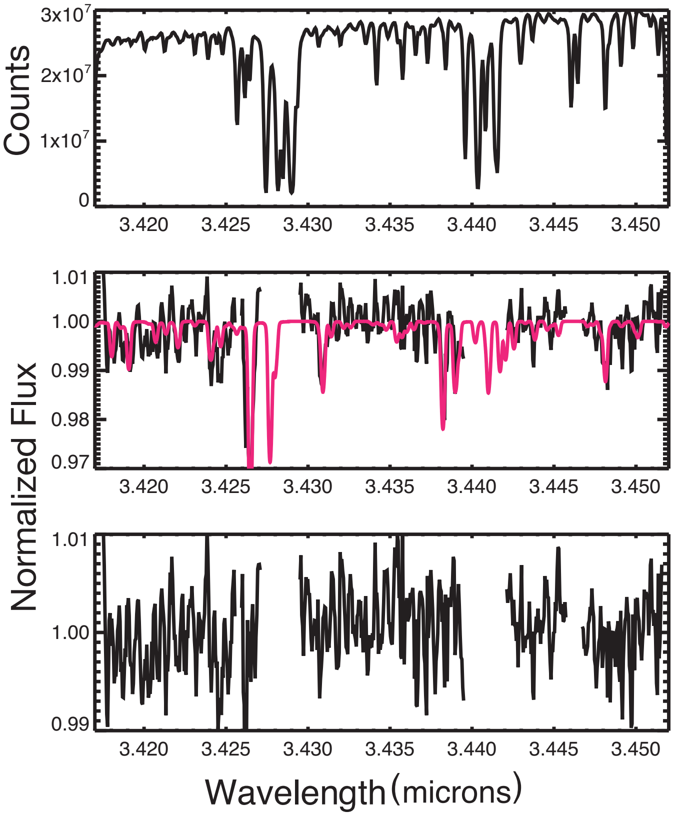

Figure 3.1: The longest wavelength order of data from 14 March 2011. *Top:* The original wavelength-calibrated data. *Middle:* Telluric-removed spectra with stellar features overlaid (dotted line). *Bottom:* Stellar- and telluric-removed spectrum.

linelist generated by Sauval (see Hase et al. 2006). Using the MARCS solar model and solar abundances in Grevesse et al. (2007), adjustments were then made to the atomic line parameters, in particular the g_f-values and damping constants, to fit the solar spectrum. For τ Boo, a stellar atmosphere with effective temperature $T_{\rm eff} = 6375$ K, surface gravity $\log g = 4.0$, and metallicity [m/H] = +0.25 was adopted, based on a review of abundance analyses in the literature. Individual abundances were set by matching observed lines for elements that were well measured by NIRSPEC (Fe, Si, Mg, Na); otherwise, an abundance of +0.25 was used.

A plane-parallel model was calculated for τ Boo b using the PHOENIX stellar and planetary atmosphere code (Barman et al. 2001, 2005). The planet is very hot, with an equilibrium dayside temperature between 1600–2000 K, depending on the day-to-night redistribution of incident stellar flux. Only 2π redistribution ($\mathrm{T_{eq}}$ ~2000 K) was used here. With an unknown planet radius, the surface gravity was arbitrarily set to 10^4 cm/sec^2. As discussed above, water lines are the primary signal we seek in the planetary spectrum and to accurately model these, we use the best available water line list from the ExoMol group (Barber et al. 2006). A final high-resolution spectral template was calculated at 10× the observed resolution ($\Delta\lambda = 0.05$ Å).

For every epoch, the target spectrum is cross-correlated to determine the cross-correlation function (CCF) for each order. The planet/star spectroscopic flux ratio is set to 10^{-5}, the same order of magnitude as the expected photometric contrast between the two objects. We also tested flux ratios from 10^{-3} to 10^{-7} and the shape of the resulting maximum likelihood function remains the same because the analysis is only weakly sensitive to the absolute contrast ratio.

3.2.3 Maximum Likelihood Analysis

To find the most likely solution, each CCF must be converted into a probability, or likelihood, $\mathcal{L}$. To do this, we start with a relationship between $\mathcal{L}$ and the familiar χ^2 statistic

$$\begin{aligned} \mathcal{L} &= \frac{1}{\sqrt{2\pi}\sigma_i} \prod_i \exp\left(-\frac{\chi_i^2}{2}\right) \\ \log \mathcal{L} &= \kappa - \frac{\chi^2}{2} \qquad (3.1) \end{aligned}$$

where κ is a constant that does not matter when comparing relative likelihoods, assuming $\sigma_i = \sigma =$ const. Denoting the observed spectra as S_i and the template spectra as $f_i \equiv$

$f(\lambda_i + \Delta\lambda)$ yields

$$\begin{aligned}\chi^2 &= \sum_i \frac{(S_i - f_i)^2}{\sigma^2} \\ &= \frac{1}{\sigma^2}\sum_i (S_i^2 + f_i^2 - 2S_if_i) \qquad (3.2)\end{aligned}$$

Each part of the quotient can be summed individually. For a continuum-normalized spectrum with N points, this results in

$$\sigma^2 = \frac{1}{N}\sum S_i^2 \qquad (3.3)$$

$$\chi_i^2 = \text{const} - \sum \frac{S_if_i}{\sigma^2} \qquad (3.4)$$

The second term on the right-hand-side of Eqn 3.4 is simply the CCF. Thus, the CCF and $\mathcal{L}$ are related by:

$$\log \mathcal{L} = \text{const} + CCF \qquad (3.5)$$

The goal is to maximize $\sum \log L$ for both the stellar and planetary velocity shifts, where the sum is over all spectral orders for an individual epoch. Figure 3.2 (top panel) demonstrates that the stellar velocity clearly stands out as the most likely solution for one epoch, as is the case for all other epochs as well. Our NIRPSEC spectra have insufficient RV precision to be sensitive to the orbital motion of τ Boo A so the stellar RV is therefore fixed at the systemic value. Barycentric movement is accounted for.

The maximum likelihood (ML) solution of the planet's orbit is much more complex. The likelihood is proportional to the CCF, a two-dimensional surface that reflects coherence in features between template spectra and those of the target. Due to the multiplicity of rovibrational transitions in the asymmetric top spectrum of hot water, the correlation coefficient remains large (>0.9) over significant offsets. This results in multiple "peaks" at incorrect velocity lags, as can be seen in Fig. 3.2. Thus, a single epoch would lead to a degeneracy of solutions. Fortunately, we do not worry about alignment between planet and telluric spectra because not only are the spectra very different, but the combined systemic and planetary RV shifts the planetary spectrum sufficiently to avoid collisions between spectral features.

3.2.4 Orbital Solution

To break the degeneracy, several epochs of data must be brought to bear. Using the known period of the planet, we calculate the orbital phase of each epoch (Table 3.1) and use that to find the most likely planetary velocity consistent with a circular Keplerian orbit (the estimated planetary eccentricity is small, e $\sim$0.02, (Butler et al. 1997; Brogi et al. 2012)). Since the absolute orbital velocity of the planet is known from the period, we are actually interested in k_p, or semi-amplitude. A range of k_p is tested, each corresponding to a different inclination of the planet, as well as a unique mass. Furthermore, each k_p leads to a different velocity lag at a given phase, such that

$$v_{pl} = \mathrm{k}_p \sin(\omega\ t + \phi) + \gamma \tag{3.6}$$

where $\omega = 2\ \pi/P$, ϕ is a phase lag that can be set to zero by choosing the proper starting date, and γ is the combined stellar barycentric and systemic velocities ($V \sin i \approx$ -15 km/s (Butler et al. 2006) and $V_{barycentric}$ listed in Table 3.1) . We then seek the best-fitting k_p by maximizing the sum of the likelihood of v_{pl} for all epochs, whose highest value indicates the most likely solution for k_p.

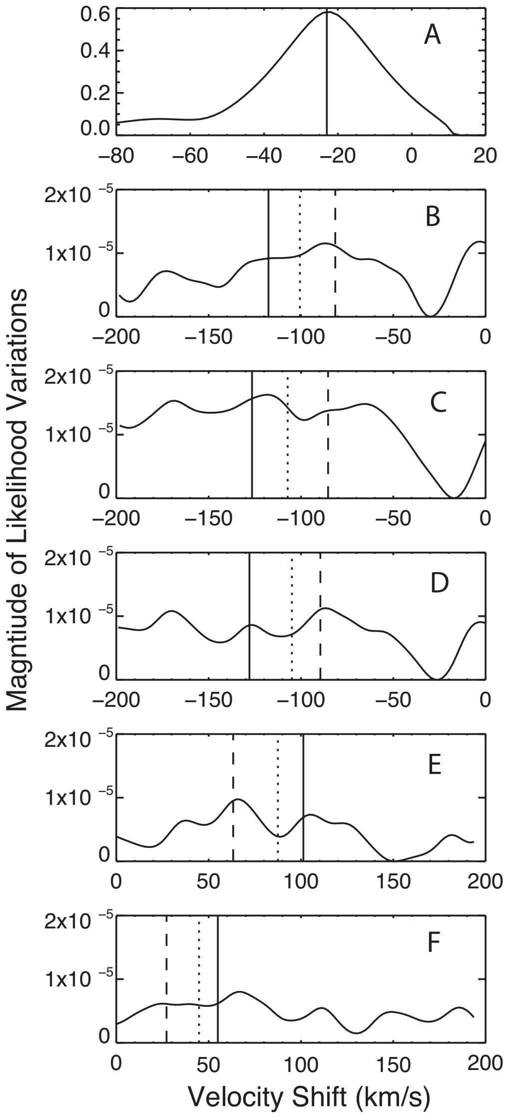

Figure 3.2: *A:* The ML function of the stellar velocity shift using the data from 24 March 2011. *B-F:* The ML function for the planet signal for 24 March 2011, 14 March 2011, 1 April 2012, 21 May 2011, and 3 April 2011, respectively. Note the changing sign of planetary velocities for each epoch, which are anti-correlated with the sign of the stellar RV shift. The vertical lines correspond to the velocity shift at a given epoch for an orbital solution with k_p=70 (dashed), k_p=90 (dotted), and k_p=110 km/s (solid).

3.3 Results

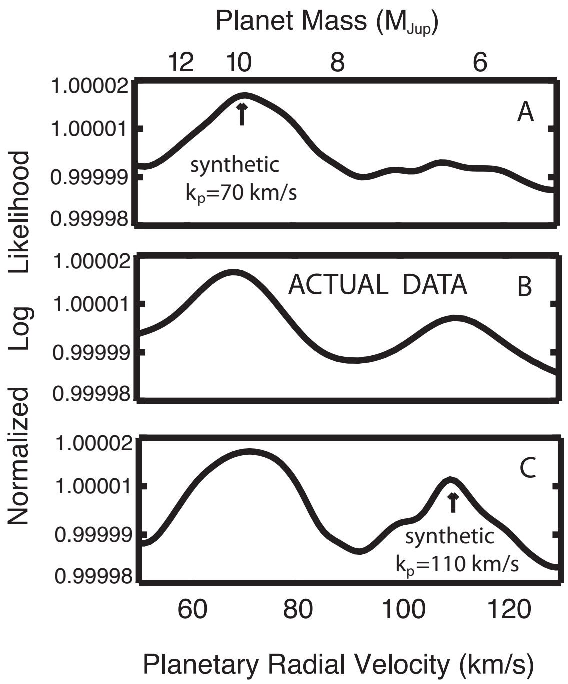

Figure 3.3: The normalized log likelihood as a function of planetary velocity, k_p. *A:* Results from synthetic spectra, composed of the stellar and planetary templates, with a planetary signal injected at 70 km/s and analyzed with the same procedures applied to the data. *B:* The data analyzed using a planet-to-star flux ratio of 10^{-5} for water vapor around a planet with T_{eq} ~2000 K. *C:* Same as *A* but for a signal injected at 110 km/s.

It is clear that the ML curve for each epoch in Figure 3.2 shows multiple peaks. Only one of these peaks per epoch can be the true peak that results from the planet signal in our spectra; the other peaks are artifacts caused by chance misalignments of the molecular lines in the model water spectrum with both signal and noise features in the observed spectra. The true peaks can be distinguished from artifacts by requiring a multi-epoch orbital solution that is consistent with a Keplerian orbit. The dashed, dotted, and solid lines in Fig. 3.2 represent the v_{pl} for three Keplerian solutions with $k_p = 70$ km/s, 90 km/s, and 110 km/s, respectively. While none correspond to the highest peak for all epochs, certain orbital solutions find peaks more often than troughs. For instance, the dashed and solid lines, corresponding to 70 km/s and 110 km/s, are seen to have higher probability at each epoch than the solution for $k_p = 90$ km/s.

To find the most likely orbit, the likelihoods at every epoch for a given k_p are combined. The second panel in Figure 3.3 presents this composite maximum likelihood, along with the corresponding planetary mass. This function represents the sum of the log likelihoods of all five epochs. There are two peaks in the likelihood function, at $K_p \sim 70$ km/s and 111 km/s. We have demonstrated empirically the degenerate effects of cross-correlating a water spectrum. Now we explore the systematics of the analysis and consider how both the properties of the individual stellar and planetary template autocorrelation functions, as well as the correlation of the two template spectra, can affect the composite likelihood function.

To do this, synthetic data sets are subjected to the same analysis as the original data. Synthetic target spectra of just the stellar and planetary templates are used, each shifted to the correct velocity for a given epoch. The results are given in Fig. 3.3, whose top panel shows the normalized log likelihood from a planetary spectrum injected at 70 km/s, with a planet-to-star flux ratio of 10^{-5}. The proper signal is clearly retrieved. However, the third panel shows that at an injected planetary radial velocity of 110 km/s and the same contrast ratio, a double-peaked log likelihood results. Thus, following exactly the same procedure as was used for the observations, a “perfect” target spectrum with no noise and no (terrestrial) atmosphere retrieves both the correct and an additional signal, with a structure that mimics the data, likely as a result of the complex hot water spectrum near 3 μm.

At a sufficiently high planet-to-star flux ratios, the true planetary signal should dominate the posterior likelihood. Indeed, using a flux ratio of 10^{-3}, Birkby et al. (2013) detect water absorption from another (transiting) hot Jupiter, HD 189733 b. The right panel of Fig. 3.4

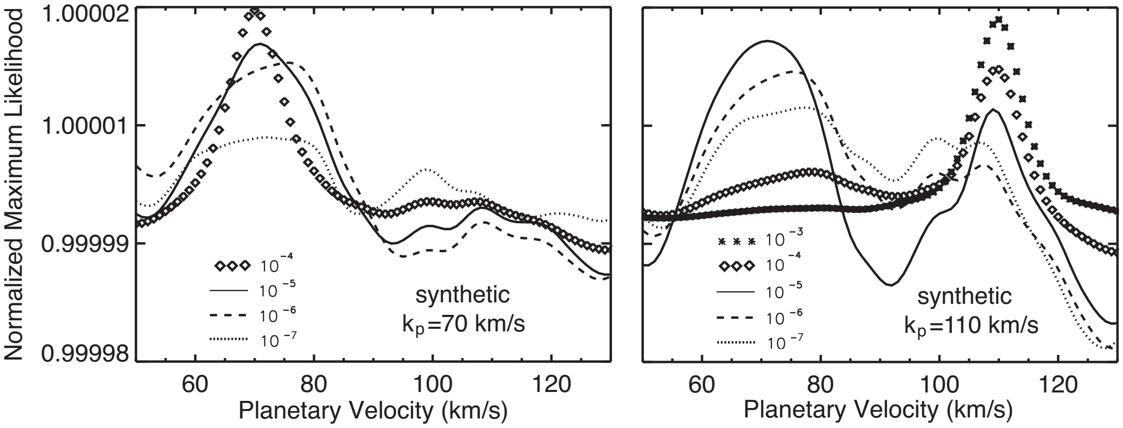

Figure 3.4: The normalized log likelihood as a function of planetary velocity, K_p, for different spectroscopic flux ratios. *Left:* Results from synthetic spectra, composed of the stellar and planetary templates, with a planetary signal injected at 70 km/s and analyzed with the same procedures applied to the data. *Right:* Same for a signal injected at 110 km/s. The signal at 110 km/s requires a much stronger planetary signal to uniquely determine the correct orbital velocity.

shows that when the flux ratio of the planetary signal is increased to this level, the singular correct velocity is retrieved. We can constrain the spectroscopic contrast of τ Boo b relative to its host star by comparing the data to these synthetic fits. The simulations show that for $\alpha \geq 10^{-4}$, the correct 110 km/s solution should present a larger maximum likelihood. Since our data do not demonstrate this, we can put a 1-σ upper limit on the high resolution spectroscopic flux ratio of 10^{-4} at $\sim$ 3.3 microns. The left panel of Figure 3.4 shows that a planetary signal of 70 km/s would be uniquely retrieved for all realistic flux ratios.

3.4 Conclusions & Future Work

The detection of τ Boo b has been a difficult quest. Contradictory results have been published over the past 15 years and the difficulty in both thoroughly removing the telluric absorption and also extracting the diminutive planetary signal is not to be underestimated. Multiple observations at different wavebands improve the validity of the detection, and facilitate a variety of statistical tests to ensure an accurate measurement.

Here, the validity of the most likely solutions for the RV of τ Boo b are explored. Of the two prominent velocities that fit the data, one is shown to result from the systematics of the cross-correlation analysis performed on this high flux ratio spectroscopic binary system. Interestingly, previous velocity studies of the planet in reflected light (Collier Cameron et al. 1999) and methane (Wiedemann et al. 2001) retrieved values close to this artifact. We suggest that residual water vapor in the atmosphere, after the telluric removal, might have been responsible for the false value previously reported from infrared observations. As methods for telluric corrections have improved over the past decade, this problem can be overcome and the correct radial velocity retrieved.

Our analysis gives a 6-σ detection of the planet at $K_p = 111 \pm 5$ km/s for τ Boo b, with a 1-σ upper-limit on the 3.3 μm planet/star spectroscopic flux ratio of 10^{-4}. To determine the significance of our detection, we injected synthetic signals at a variety of planetary velocities and planet-to-star spectroscopic flux ratios and constructed the chi-square surface of the maximum likelihood fits. The orbital velocity is in good agreement with previous RV amplitude detections via CO by Brogi et al. (2012) and Rodler et al. (2012), and our analysis reveals the presence of water vapor in the planet's atmosphere. Furthermore, using a stellar mass of $1.341^{+0.054}_{-0.039}$ $M_\odot$ (Takeda et al. 2007) and a stellar velocity semi-amplitude of 0.4664 ± 0.0033 km/s (Brogi et al. 2012), we derive a planetary mass of $M_P = 5.90\ ^{+0.35}_{-0.20}$ M_{Jup} with an orbital inclination of $i = 45\ ^{+3}_{-4}$ degrees.

The technique presented here is in its nascent stages, and the work is by no means complete. Additional quantitative characterization of the physical properties (temperature, opacity) and composition (and thus estimates of vertical mixing) of τ Boo b's atmosphere will require both significant simulations of the atmospheric radiative transfer and data analysis along with additional data at longer and shorter wavelengths. Such work is beyond the scope of this letter, but expanded studies of τ Boo using the same methods described above, but also including molecules such as CH_4 and CO at longer wavelengths than examined here, are underway. Indeed, although the mole fractions of methane should be insignificant for τ Boo b, we have searched for the molecule using the methods described herein and have no detection to report in our data. With careful analysis in the future, the relative abundances of these molecules in the atmospheres of non-transiting exoplanets can be ascertained. Further applications of this technique, using water and methane as template molecules, to a variety of additional hot Jupiter exoplanets will be reported elsewhere.

3.5 Extended Analysis

The data were subjected to numerous tests to probe the rigor of the atmospheric water vapor detection, to more thoroughly explore the possible explanations of the second peak observed near 70 km/s, and to search for other species in the atmosphere – specifically methane (CH_4).

3.5.1 Chunked Data

We have performed several tests on the data and template spectra in addition to those outline above. Our first test is to separate the data into smaller chunks and rerun the analysis. We find that the double peaked solution remains intact when we separate the data in time, analyzing the first half of the observations and then the second half. We also separate the data by order and the solution remains double-peaked. Removing any of the epochs from the analysis did not change the shape of the maximum likelihood function either. Another test is to run the cross correlation again with fake planetary spectra to see if the false signal persists. To do this, we bin the template planetary spectra and randomly rearrange sections of the spectra. The bin size was varied from 7 cm^{-1} down to 0.13 cm^{-1}. We found that for the largest bin sizes, the structure in the water spectrum was not sufficiently randomized. The resulting likelihood function no longer had the correct peak, but still had a peak at the $\sim$ 70 km/s lag. However, when the bins were made small enough and randomized, thereby destroying any coherent water structure, neither of the peaks appeared in the posterior log likelihood. These tests gave an indication that the planetary water template was responsible for the lower velocity peak, however they were not convincing alone, and so additional tests were undertaken using the template spectra.

3.5.2 Template Spectra

The template spectra used in the cross correlation analysis are presented here for further analysis. Figures 3.5 and 3.6 show the original template spectra, as described in the Methods section above.

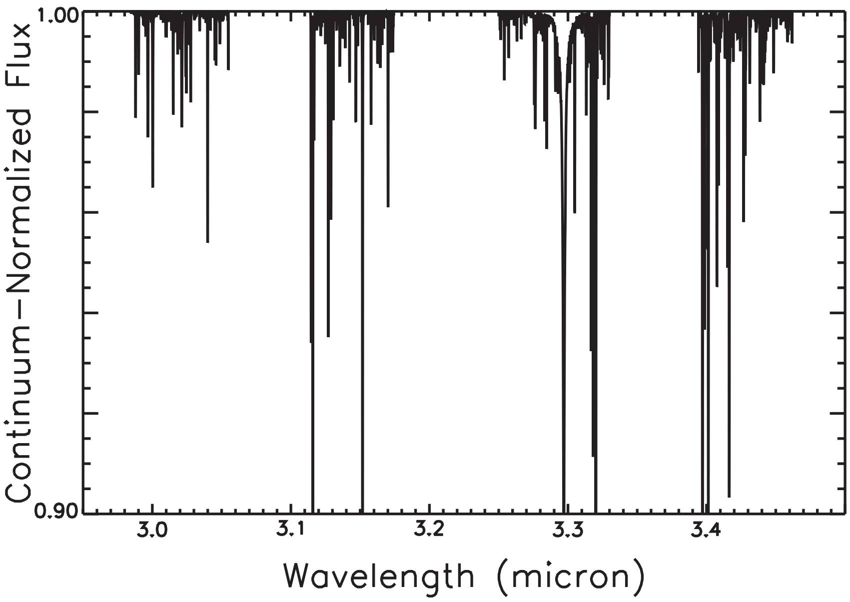

Figure 3.5: The stellar spectrum used in the cross correlation analysis.

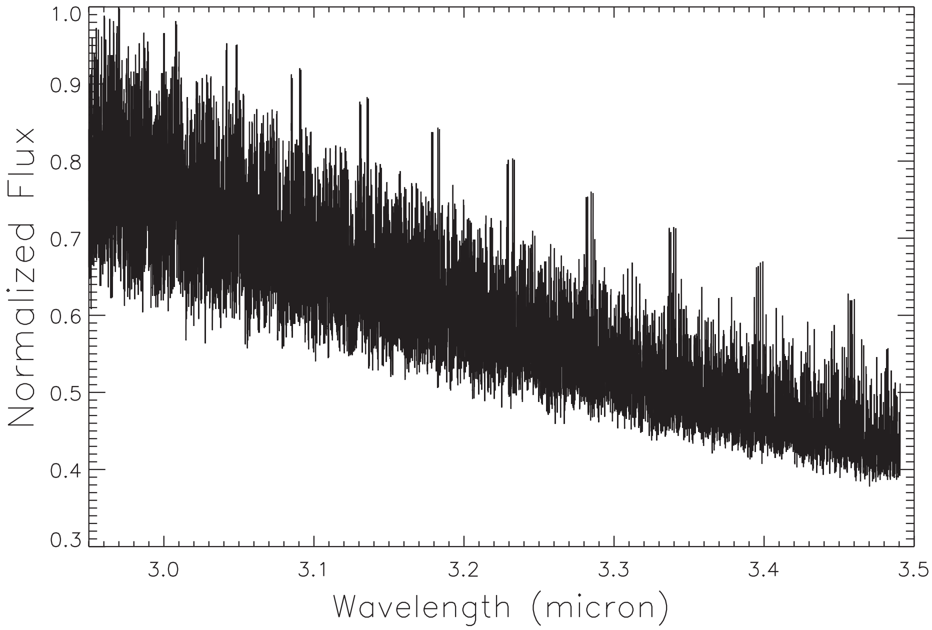

Figure 3.6: The water-dominated planetary atmospheric spectrum used in the cross correlation analysis.

In analyzing the CCF, it is necessary to consider both the structure in the individual stellar and planetary template autocorrelation functions, as well as the correlation of the two template spectra. This is due to the fact that the two-dimensional cross-correlation code compares both template spectra to the observations simultaneously. This means that features in either template could correlate with features in either component of the target spectra. Figure 3.7 shows the autocorrelation function when the stellar template, described above, is cross-correlated with itself. Fortunately, the difference between the correlation of the stellar velocity at the correct velocity lag (0) and an incorrect velocity lag (< 0 or > 0) is large, especially for velocity lags where Δ v > 30 km/s. For this reason and as can be seen from the data analysis, the CCF of the stellar velocity is a single, distinguishable peak for every epoch.

However, the planetary template does not cross-correlate with itself so cleanly. It can be seen in Fig. 3.8 that there is indeed a strong peak at zero velocity lag between the

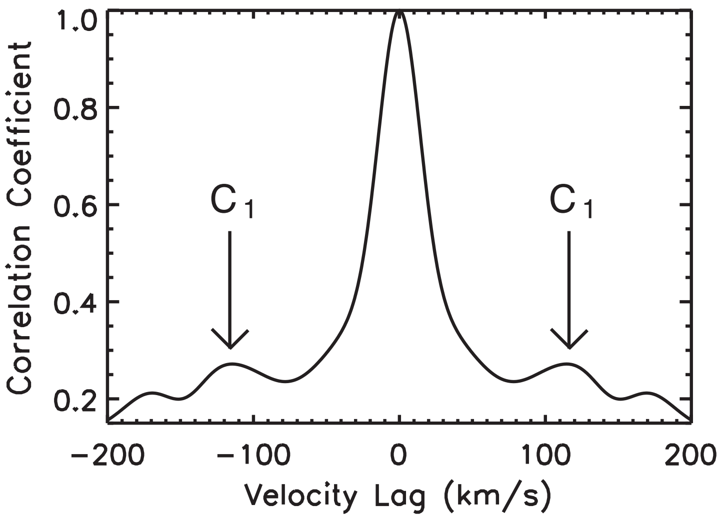

Figure 3.7: The stellar template spectrum autocorrelation function.

template and itself, as there should be. There is also a high correlation of the planetary spectrum with itself at almost any other velocity lag, with a correlation better than 80%, due to complex nature of the asymmetric top water molecule at high temperatures. This strong correlation coefficient indicates that the multiplicity of features in the planet spectra are easily confused with each other, at varying velocity lags. We do see, though, that a lag of ∼ ±80 km/s or ∼ ±120 km/s are favored more than other lags. We will discuss this further below. Another correlation to consider is between the stellar and planetary templates shown in Fig. 3.9. There is some distinct structure in this correlation function, and while the scale of this correlation is much smaller than either of the autocorrelations, the magnitudes of the peaks in Fig. 3.9 are larger than those in the planetary CCF analyzing the data. The takeaway message is that correlations between the templates can have an effect on the relative magnitudes of the peaks in the CCFs and therefore bias the overall most likely orbital solution.

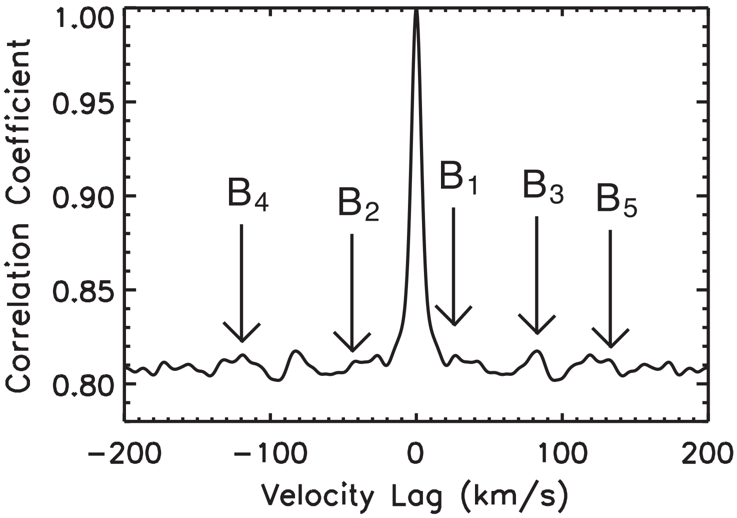

Figure 3.8: The planetary water template spectrum autocorrelation function.

3.5.3 Generating Synthetic Spectra

A rigorous test of the analysis is to create synthetic target spectra and run them through the cross-correlation analysis procedure that we use for the data. If we know how a planetary signal at a given orbital radial velocity *should* respond, we can compare this to our results. Specifically, we will test the two aforementioned most likely solutions. Synthetic spectra for a variety of spectroscopic flux ratios, α, and a number of orbital velocities, k_p, were created by combining a stellar and planetary template at the correct spectral shifts and relative fluxes; Figure 3.4 in the previous section shows the resulting maximum likelihood functions.

At high flux ratios, either signal clearly stands out. As the flux ratio lowers, the lower peak appears in the right panel of Figure 3.4 and persists down to planetary signals smaller than our detection limits. Figure 3.10 shows exactly where the maximum likelihood profile changes from single to double-peaked. For a spectroscopic ratio of 5 x 10^{-5} or greater, the water signal should be uniquely retrieved for a k_p of 110 km/s. However, the synthetic

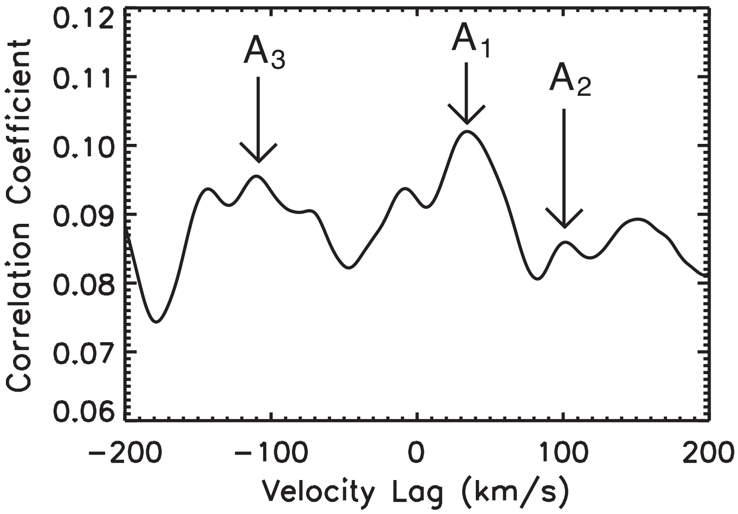

Figure 3.9: The cross-correlation function between the stellar and planetary model templates.

signal at k_p of 70 km/s is retrieved down to flux ratios of 10^{-6}. At a smaller spectroscopic flux ratio, we see some structure begin to arise in the maximum likelihood function. Even then, the 70 km/s is the strongest and the second strongest peak, at $\sim$ 100 km/s, does not match our analysis of the data.

The fact that essentially "perfect" spectra - spectra with no noise and no telluric features to remove, comprised solely of the template spectra added together at the correct flux ratio - do not uniquely retrieve a planetary water signal injected at 110 km/s, is demonstrative. That the shape of the likelihood function mimics the data, provides an even stronger case that the water signal is indeed at k_p =110 km/s. However, the exact reasoning for this phenomenon is a bit trickier to determine.

3.5.4 Closer Examination of Cross Correlations

If we look more closely at where the peaks lie in these correlation functions, we begin to understand where the $\sim$ 70 km/s signal, that is coupled with the correct signal, might

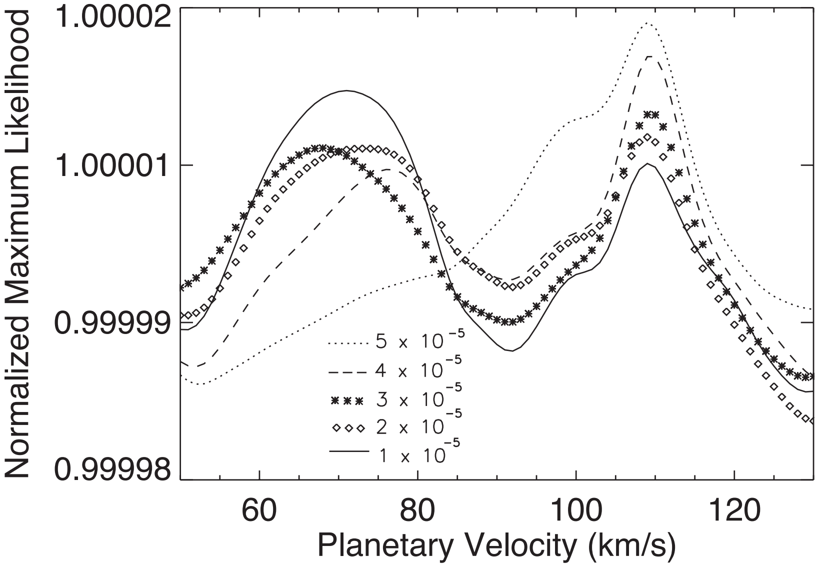

Figure 3.10: Maximum likelihood functions using k_p = 110 km/s and flux ratios from $\alpha = 1\times10^{-5}$ to $\alpha = 5\times10^{-5}$, demonstrating the change in retrieval from a double- to a single-peaked likelihood.

Table 3.2: Orbital Velocity Solutions at Phases of Epochs

Date	Phase	V_{pl} if k_p=110 km/s	V_{pl} if k_p=70 km/s
21 May 2011	0.3199	99.5	63.3
03 Apr 2012	0.3847	72.9	46.4
01 Apr 2012	0.7810	-107.9	-68.7
14 Mar 2011	0.8164	-100.6	-64.0
24 Mar 2011	0.8353	-94.5	-60.2

originate. For reference, Table 3.2 lists the planetary velocity with respect to the star, for each epoch we observe, assuming either of the two k_p in question, 70 km/s or 110 km/s. In other words, the tables lists $v_{pl} = K_p \sin(\omega\ t)$. We will ignore ± 25 km/s from the stellar velocity, to accommodate for the wide autocorrelation feature. This means we can ignore this region from the planet-star correlation as well. It is good that the epochs were chosen to capture the planet at quadrature, thus maximizing the difference between the stellar and planetary velocity. However, we will see that the specific epochs that were chosen might actually lead to the degenerate solution of the maximum likelihood function. We can also ignore planetary velocities 150 km/s since we know the absolute orbital velocity of the planet and the system is not transiting.

Here we consider the correlation peaks at +34 km/s (A_1)+102 km/s (A_2) and -112 km/s (A_3) in Fig. 3.9, ±28 km/s (B_1), ±42 km/2 (B_2), ±83 km/s (B_3), and ±120 km/s (B_4) in Fig. 3.8, and ±120 km/s (C_1) in Fig. 3.7. The question is: Do any of these correlation peaks preferentially support one of the two orbital solutions (k_p=110 km/s or k_p=70 km/s) we are comparing? Peaks that are velocity shifted from the stellar velocity are A_1, A_2, A_3, and C_1. If we look at Table 3.2 (which lists the planetary velocities with respect to the stellar velocity) we can see that the solution for k_p=110 km/s on 21 May 2011, might have a higher correlation coefficient due to A_2. However, our analyses are robust if we ignore any of the epochs, so this single coincidence cannot be the cause for the double-peaked result. We see that A_3 and C_1 do not prefer either of the k_p values we find to be most likely. The final peak to consider, A_1 might be part of the answer we seek. The function plotted in Fig. 3.9 is the velocity shift of the planet with respect to the star. However, since the correlation is two-dimensional, we can also consider the shift of the stellar template relative to the planetary template spectrum. In this case, the sign of all velocity lags in Fig. 3.9 is reversed. We then consider A_1 as a preferential velocity shift with respect to the actual planetary template position. Table 3.2 shows that, at the epochs we selected, the -34km/s that the A_1 peak would preferentially boost the correlation of k_p=70 km/s for the observations on 21 May 2011.

Now we turn to other velocity shifts with respect to the velocity of planetary template spectrum. The planetary autocorrelation peaks might help explain the double peaked structure. If we look at the differences between the third and fourth columns in Table 3.2, all differences are within 26 and 40 km/s. This is the same range that appears slightly preferential in Fig. 3.8 corresponding to B_1 and B_2. The fact that the planetary template correlates well with itself at all velocity shifts, but especially at $\Delta v \sim 30$ - 40 km/s, means that solutions with those velocity shifts with respect to the actual planetary velocity will be preferred. In other words, all of the V_{pl} for k_p=70km/s for our given epochs are automatically preferred as solutions when the actual signal is k_p=110 km/s. Finally, the other two peaks (B_3 and B_4) in the planetary autocorrelation function would result in unphysical peaks in the CCFs of the data, so we can ignore them.

The synthetic spectra above demonstrate that the double-peaked nature of the maximum likelihood function comes directly from cross-correlating planetary and stellar templates with a target spectra that has a k_p of 110 km/s. The structure in the template correlation functions does not explicitly explain why this happens, but does support the findings.

3.5.5 Other Molecules

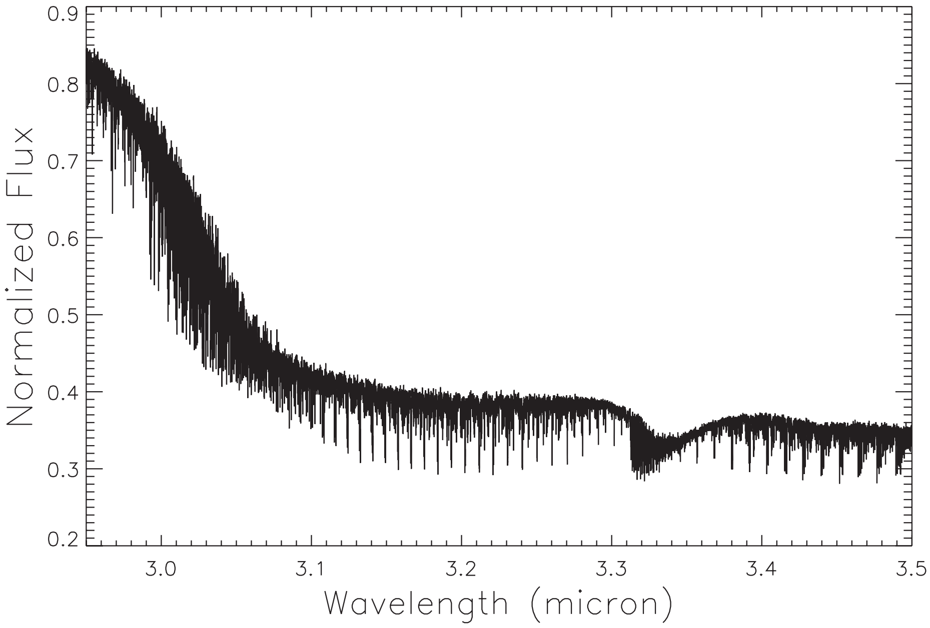

Figure 3.11: The methane-dominated planetary atmospheric spectrum used in the cross correlation analysis.

Two other molecules that are expected to be abundant in the atmospheres of hot Jupiters are CO and CH_4. Brogi et al. (2012) and Rodler et al. (2012) confirmed the presence of hot CO in τ Boo b. Here we look for the presence of methane in our spectra. The methane template spectrum that was used in the following analysis is shown in Fig. 3.11. Again we see multiple structures at high correlation coefficients in the autocorrelation of the template with itself (Fig. 3.12) and structure in the correlation of the methane template spectrum with the stellar template spectrum (Fig. 3.13). However, we do not detect methane in the data. The top panel of Figure 3.14 shows the likelihood of methane being present in the planet, assuming a flux ratio of $\alpha = 10^{-5}$. Using synthetic spectra generated in the same way as described above, except using a methane planetary template for a slightly cooler planet, we find that if the spectroscopic flux ratio of the methane in the planet was $\alpha = 10^{-4}$ or greater, we would be able to detect it (bottom panel of Fig. 3.14). However, there are not enough unique features in a methane spectra to detect a signal of $\alpha = 10^{-5}$ or less, making this the upper limit on our non-detection of methane.

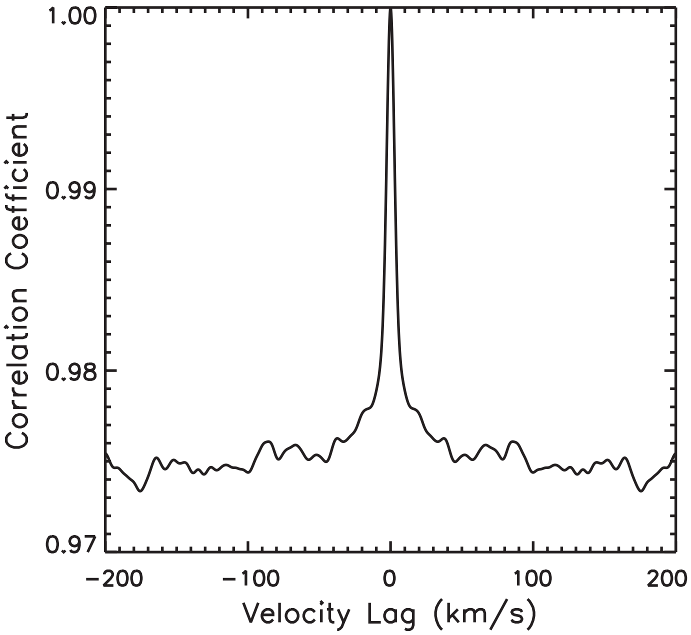

Figure 3.12: The planetary methane template spectrum autocorrelation function.

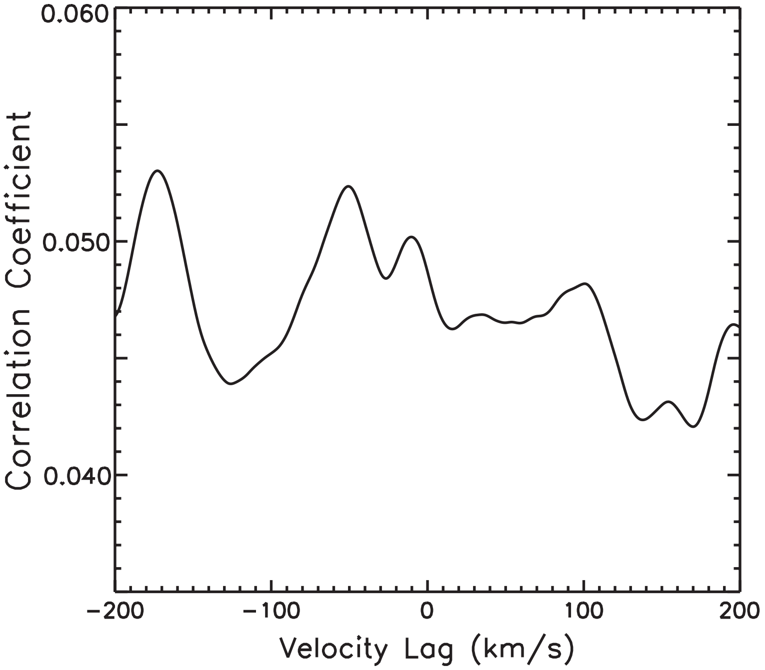

Figure 3.13: The cross-correlation function between the stellar and planetary model templates, using a methane-dominated planetary atmosphere.

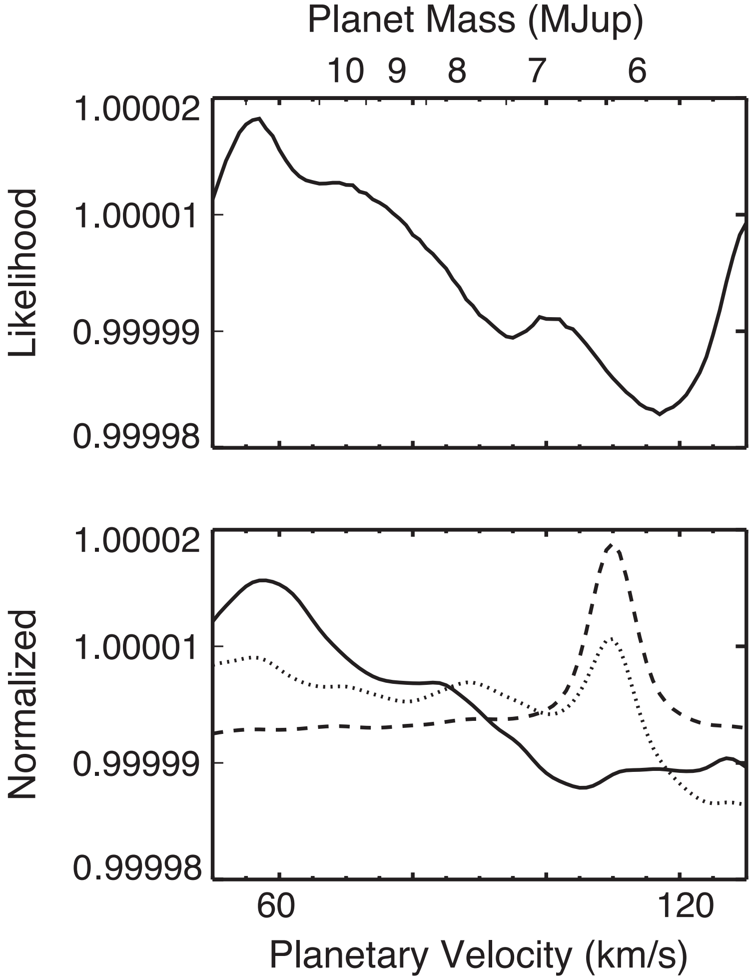

Figure 3.14: The normalized log likelihood as a function of planetary velocity, k_p. *Top:* The data analyzed using a planet-to-star flux ratio of 10^{-5} for methane around a planet with T_{eq} ~1200 K . *Bottom:* Results from synthetic spectra, composed of the stellar and planetary templates, with a planetary signal injected at 110 km/s and analyzed with the same procedures applied to the data and a variety of α values.

Chapter 4

Protoplanetary Disks

4.1 Introduction

All planetary systems undergo a formation phase in which ∼micron-sized dust (and, at sufficiently large radii, ice) grains grow to planetesimals in a gas-rich environment, and where giant planets may form. This *protoplanetary* phase is characterized by a high mass surface density 0.001-0.1 $M_\odot$ disk in near-Keplerian rotation that consists of, by mass, 98-99% molecular gas, principally H_2+He, and 1-2% of solids such as silicates and ices. The dynamics of protoplanetary disk material govern their evolution and ultimately drive the formation of planets. Indeed, the observed diversity (Marcy et al. 2005; Batalha et al. 2013) of (exo)planetary systems suggest that planet formation is highly sensitive to the properties of the disks from which they form. Once one or more protoplanets of significant mass have formed, they can then begin to sculpt their parent disk through dynamical interactions. Protoplanets of sufficient size may carve out gaps, excite spiral arms and twist the disk gas into elliptical orbits (Goldreich & Sari 2003; Machida et al. 2010). At early stages, these effects can in principle be observed in the molecular gas in the planet-forming region (in most cases radii near or within 10 AU). Thus, there is a strong drive to observe large samples of protoplanetary disks to reveal the properties (kinematics, relative abundance, mass and chemistry) of the molecular gas in the inner few to few tens of AU in protoplanetary disks.

Arguably the most robust, and most readily available, tracer of molecular gas in inner protoplanetary disks is the rovibrational fundamental ($\Delta v = 1$) band of CO, conveniently located in the atmospheric M-band window at 4.5-5.2 μm. The transitions in the M-band trace gas of a few 100 to a few 1000 K gas in only the upper $\sim 1\%$ of the disk, due to the high disk opacity provided by dust. In the past 5-10 years, a growing list of observational studies of rovibrational CO in protoplanetary disks has emerged (Najita et al. 2003; Brittain et al. 2003; Blake & Boogert 2004; Rettig et al. 2004; Brittain et al. 2007; Pontoppidan et al. 2008; Salyk et al. 2009; Brown et al. 2013), demonstrating that the CO fundamental is, essentially, ubiquitous in protoplanetary disks.

Yet, the line formation of the CO rovibrational transitions is not well understood, for a number of reasons. Most importantly, the rovibrational transitions of CO have very high critical densities – of order $10^{12}\,\mathrm{cm}^{-3}$, too high to thermalize the excited vibrational states in the disk surfaces where the lines form. In spite of this, simple models assuming Local Thermodynamic Equilibrium (LTE) are actually remarkably successful in reproducing the integrated line strengths and rough excitation temperatures in disks around low-mass to solar-mass disks (Salyk et al. 2007; Pontoppidan et al. 2009).

At higher stellar temperatures and masses, the LTE models clearly break down as the CO vibrational states are excited to distances of 10s of AU by an ultraviolet-driven fluorescent pumping mechanism (excitation through electronic states, followed by a rovibrational cascade) (Brittain et al. 2007; Brown et al. 2012). This process is easy to recognize because it leads to very high vibrational temperatures ($\sim$5000 K or more) in regions of the disk where the kinetic temperatures are as low as $\sim$100-200 K. The problem therefore seems to be: How are rovibrational CO lines excited in the absence of a strong UV radiation field, and why does the vibrational ladder appear to be nearly thermalized in protoplanetary disks around low-mass and Sun-like stars?

These questions are particularly important because the standard assumption of thermalized level populations may lead to erroneous determinations of the physical parameters of the gas, CO abundance, kinetic temperature, gas-to-dust ratios, etc. Furthermore, it is not just the gas that we aim to characterize. At planet-forming radii, the disk is highly optically thick and we must use the surface emission to infer the entire vertical structure of the disk. We therefore aim to quantify the processes in the upper layers of the disk, where low densities and radiative processes necessitate a non-LTE formalism. Though more complex than LTE calculations, ultimately the improved understanding provided by non-LTE simulations can not only model the resultant emission, but link the observed line ratios and kinematic properties to both the local physical characteristics of the emitting gas and the disk as a whole.

In this chapter, we isolate the effects of non-LTE excitation of rovibrational CO in protoplanetary disks around low- and solar-mass young stars. To this end, we use the two-dimensional raytracing code RADLite (Pontoppidan et al. 2009), which is optimized for rendering lines in the infrared, with the assumption of CO level populations in LTE removed. This is accomplished by adding an escape-probability statistical balance calculation, following the approach of Woitke et al. (2009). We then generate non-LTE model grids that we match to a comprehensive database of high resolution M-band spectra obtained with the Keck-NIRSpec and VLT-CRIRES instruments (Salyk et al. 2011; Brown et al. 2013). The grid is used to reproduce observed rotation diagrams, line-to-continuum ratios, as well as line profiles. We focus on isolated classical T-Tauri stars (cTTs) with material that is dominantly in Keplerian rotation to understand the basic excitation processes of warm CO at a few AU from the central star.

This chapter is organized as follows. The observational database is described in Section 2, while the non-LTE modification to RADLite is developed in Section 3. Section 4 presents the model grid for both the LTE and non-LTE cases. In Section 5, we match the main observables to the model grid and identify the best-fit regions of the parameter space searched. Finally in Section 6, we discuss the implications and identify the main excitation process for rovibrational CO emission in disks around low- to solar-mass young stars.

4.2 Observational Database

The goal of this chapter is to explore how modeling can be used to investigate interesting disk characteristics. We will use the observational properties of the CO emission to constrain and guide our understanding. Models are compared to a sample of high spectral resolution disk data, collected using the NIRSPEC instrument at the W.M. Keck Observatory by Salyk et al. (2011) and the CRIRES echelle on the Very Large Telescope by Brown et al. (2013). A summary of disk properties in the sample is listed in Table 4.1. For the most part, these are taken from published surveys of the CO emission from disks with reasonably well characterized distances and inclination angles. It is important to note the range in stellar masses and temperatures presented here, which correspond to luminosities spanning more than an order of magnitude.

Table 4.1: ^{12}CO Observational Disk Properties

Source Name	M_{star} (M_{sun})	T_{star} (K)	i deg	P(10) FWHM (km/s)	P(10) L2C ratio	P(30) FWHM (km/s)	P(30) L2C ratio
AS 205 N	1.5	4450	25	30.26	1.92	31.10	1.58
DF Tau	0.53	3470	78	80.39	1.52	86.41	1.42
DL Tau	0.56	4060	25	31.31	1.16	92.99	1.22
DoAr24E S	–	5250	–	59.51	1.41	70.73	1.42
DoAr 44**	1.4	4730	45	48.61	1.35	61.76	1.24
DR Tau	0.4	4060	37	26.82	2.47	28.26	2.00
GK Tau	0.75	4000	52	92.67	1.28	86.62	1.25
GQLup	0.8	4060	–	86.96	1.45	84.71	1.34
HD135344**	1.8	6600	21	20.54	1.18	20.94	1.04
HD150193	2.3	8970	38	44.84	1.11	61.94	1.05
HD190073	5.05	9500	28	37.20	1.11	17.31	1.10
HD50138	–	11480	–	45.36	1.06	38.09	1.04
LkHα327	–	–	–	63.33	1.51	49.92	1.38
LkHα330**	2.5	5800	42	17.96	1.29	23.35	1.06
RNO90	0.9	5662	37	74.09	1.53	65.55	1.50
SCrA*	1.5	4800	–	21.76	1.66	45.96	1.40
V1121Oph	0.9	4250	38	49.28	1.15	87.89	1.15
VVSer	2.6	10600	70	60.68	1.08	64.82	1.06
VSSG1	0.52	3890	53	26.55	1.54	64.99	1.55
WaOph6	0.9	4205	39	121.67	1.17	162.55	1.16

The disks used for comparison with the models, with measured high-J and low-J lines. **The P(30) fits are actually to P(31) for SCrA. ** indicates a transitional disk.*

4.3 Modeling

4.3.1 Continuum Radiative Transfer

The dust continuum radiation field is generated for a 2D axisymmetric disk using the RADMC program (Dullemond & Dominik 2004). Most runs presented here use a grid of 70 vertical and 150 radial divisions, dispersed logarithmically to provide better sampling at the inner radii. We use Kurucz stellar spectra for a given stellar mass, radius, and temperature to generate photon packages of varying frequencies. RADMC employs a Monte Carlo approach to distribute photon packages into the disk and follow their scattering, emission, and absorption. The output is the local dust temperature and mean intensity at

Table 4.2: ^{13}CO Observational Disk Properties

Source Name	R(12) FWHM (km/s)	R(12) L2C ratio	T$_{star}$ (K)	NCol (cm^{-2})	Temp (deg K)
AS 205 N	26.95	1.12	4450	19.5	1200
DR Tau	16.80	1.12	4060	18.9	8505
HD150193	–	–	8970	18.8	750
HD190073	–	–	9500	20.9	600
HD50138	–	–	11480	19.8	900
LkHα327	–	–	–	19.8	600
LkHα330**	17.83	1.03	5800	18.3	500
SCrA	39.84	1.13	4800	19.1	900
VSSG1	33.15	1.13	3850	19.0	750

Line shapes of the v=1→0 ^{13}CO emission. Column densities and temperatures are fit as described in 4.5, using both ^{12}CO and ^{13}CO lines, with a constrained emitting radius of 0.5 AU. ***LkHα33 is a transitional disk.*

all frequencies, for every point in the grid. This output depends on the input stellar and disk properties.

4.3.2 Non-LTE Line Excitation

The precise excitation of a molecule in non-LTE conditions requires a complete calculation of individual level populations. To do this we follow the method of Woitke et al. (2009) and Poelman & Spaans (2005) with some modifications, described next. We aim to balance the equation of statistical equilibrium for an N-level system such that

$$\Sigma n_u R_{ul} = \Sigma n_l R_{lu}$$

where R_{ij} is the rate coefficient for bound transitions between the upper and lower levels and

$$R_{ul} = A_{ul} P_{ul}^{esc} + B_{ul} P_{ul}^{pump} J_{v_{ul}} + C_{ul}$$

$$R_{lu} = B_{lu} P_{lu}^{pump} J_{v_{lu}} + C_{lu}.$$

We use the Einstein relations

$$B_{ul} = \frac{c^2}{2h\nu^3} A_{ul}$$

$$B_{lu} = \frac{g_u}{g_l} B_{ul}$$

and the numerical approximation for P^{esc} and P^{pump} as described in Woitke et al. (2009), for computational efficiency. The probability that an emitted photon will escape the disk or be absorbed as a radiative pumping mechanism depends on the optical depth in the disk. We calculate the optical depth in a vertically integrated line by

$$\tau = \frac{A_{ul} c^3}{8\pi \nu_{ul}^3} \int \frac{n_u}{\Delta v_d} [\frac{n_l g_u}{n_u g_l} - 1]$$

over all heights in the disk, where v_d is the velocity dispersion at the disk, which we set to 1 km/s for all models. This value affects the line widths, but is inconsequential at the resolution of the data we are modeling.

We employ an iterative second order Newton-Rahpson scheme with backtracking to converge on a solution for all level populations. Convergence was tested with a variety of initial conditions leading to the same results. All models presented here began with LTE initial conditions. We parallelize this process to minimize computing time, computing several radii simultaneously. This is possible because while the optical depth is a function of depth into the disk, there is little/no communication between radii thanks to the steep radial velocity gradient in disks and the high optical depth radially through the disk, both of which enforce minimal radiation transfer.

4.3.3 Molecular Information

In all models we include the first 3 vibrational states up through $J = 40$, as listed in the Leiden Atomic and Molecular Database (van der Tak et al. 2007). The molecular abundance of ^{12}CO is set to 10^{-4} per H, and we use an isotopologue abundance of 70 for ^{12}CO/^{13}CO (Wilson 1999). We note that while lower abundances of CO have been noted at larger radii in disks (Qi et al. 2013; Favre et al. 2013), either due to freeze out onto grains at low temperature or chemical processing in the gas or icy grain mantles, the rovibrational emission we model is from the much warmer inner radii, where CO is the preferred form of carbon. We ran several models including higher vibrational states, and found no hot band emission from states above $v = 2$, which is consistent with the data on cTTs disks (Salyk et al. 2011). Furthermore, we did many runs including these higher levels and see no qualitative affect on the spectra. Although UV fluorescence has been argued to be a factor in young stellar systems, the data indicate otherwise, and we do not include it in our work. We do incorporate all possible rotational and vibrational transitions between the levels, and have over 2000 collisional transitions from Neufeld & Hollenbach (1994), Flower (2001), Wernli et al. (2006), and Yang et al. (2010). We have gathered collisional rates for p- and o-H_2, He and electrons, although currently only molecular hydrogen is included as an abundant collisional partner. Published values include rotational transitions as well as vibrational excitation with $\Delta J = 0$.

While other groups include several collisional partners in the warm molecular environment, we argue that abundant H_2 is sufficient. Najita et al. (2011) use a thermal-chemical model to show that there is a sharp transition from atomic to molecular hydrogen. At this same level in the disk, which corresponds to a sharp temperature gradient, there is a complete transition from C to CO. Therefore, the CO emitting region is highly molecular.

We also do not include electron-CO collisions in our current model, although we have the capability. Neglecting to do so, however, should not affect the results significantly as the molecular emission comes from below the extremely hot surface of the disk, where ionization and thus free electrons should be considered (Najita et al. 2011). Furthermore, we do not include X-ray or UV heating at this time, which have been shown to further discretize layers of the disk with regards to temperature and ionization level.

4.3.4 Line Rendering

Spectra at the proper resolution and frequency were generated with the raytracing code RADLite, as described in Pontoppidan et al. (2009). The models assume a kinematic resolution of 12 km/s, in accordance with the spectroscopic performance of NIRSPEC.

4.4 Model Grid

We vary the disk and stellar properties as we explore their implications in the resultant spectra. The available stars with measured near-IR CO line emission guide our parameterization, and we model a representative sample of B to M stars to match the range of observed luminosities. We use Siess et al. (2007) isochron models of pre-main sequence stars with an age of 2 Myr. According to these models, the stellar luminosity should not change by more than an order of magnitude during a disk lifetime (∼10 Myr). Table 4.3 states the stellar properties explicitly.

The disk properties are allowed to vary over a physical ranges of values, and the effects of each parameterization are discussed in due turn. Disk mass is modeled for several orders

Table 4.3: Stellar Model Parameters

Mass (M_{sun})	Temperature (K)	Radius (R_{sun})	Luminosity (L_{sun})
0.5	3765	1.5	0.2
1.0	4275	2.0	1.3
2.0	4820	2.85	4.4

of magnitude around the minimum mass solar nebula value. The mass loss rate of the star will depend on the stellar type, accretion rate, and age of the disk, leading to a wide range of possible conditions. Also variable is the shape of the disk surface, which changes with the index of the scale height power law, $y \propto (H/R)^{\alpha}$. We model an unflared disk, $\alpha = 0$, the value determined from Chiang & Goldreich (1997) for a disk in hydrostatic equilibrium, $\alpha = 2/7$, as well an intermediate value of $\alpha = 1/7$. The more flared a disk, the larger the surface radii that can intercept stellar radiation. Thus, changes in the flaring parameter change the shape of the line quite significantly. As we will discuss later, a self-shadowed disk $\alpha \leq 0$ might even be needed to explain some of the observed emission line profiles.

Finally, we vary the gas-to-dust ratios from the ISM value of $\sim$100 to enhanced values of 10^4. To understand disk evolution, we are interested in the grain growth and dust settling. Other than millimeter CO measurements, there is not a good way of accessing the dust content, and specifically how much it has settled for a given disk. We use inflated gas-to-dust ratios (higher than the typical ISM value of 128), to mimic these dust processes. Enhanced gas-to-dust ratios have been shown to be necessary to match lines fluxes from several disks. Brittain et al. (2005) and Rettig et al. (2006) use rovibrational emission lines to measure CO gas columns of up to an order of magnitude greater than the ISM value in nearby disks, and recent results from the Herschel Space Telescope have demonstrated that rotational emission lines also require enhanced gas-to-dust ratios (Bruderer et al. 2012;

Fedele et al. 2013b; Meeus et al. 2013). Furthermore, the line to continuum ratios of water is also better fit with higher gas-to-dust ratios (Meijerink et al. 2009).

4.5 Results

While CO has been observed in numerous sources, the spectral characteristics between disks vary greatly (Salyk et al. 2011; Brown et al. 2013). The line shapes, line-to-continuum ratios, rotational temperatures, isotopologue ratios and relative strengths between overtone and fundamental emission lines can each differ by more than an order of magnitude among disks in the same star-forming region. The unique evolutionary path and current conditions of each system must be explored in order to understand the vast differences between the observed spectra. Fortunately, the parameterization of certain stellar and disk properties provides an equally diverse array of CO spectra. We use the available data to constrain the plausible disk parameters, and study trends within the model parameters that help us discern gas excitation mechanisms.

4.5.1 LTE versus Non-LTE

Previous studies of disks have modeled warm emission from gas in local thermodynamic equilibrium. While computationally difficult, a full non-LTE treatment of the gas is necessary to accurately model the state of the disk. Here we explore the necessity of non-LTE and present differences derived from the different analyses.

4.5.1.1 Rotation Diagrams

A common tool used for analysis of CO emission is a rotation diagram, used to attempt to extract disk parameters from the lines (Salyk et al. 2008, 2009). In this straightforward calculation, an emitting temperature, area, and column density can be uniquely determined for disks with measurable ^{12}CO and ^{13}CO emission – provided optically thick and thin lines are measured. The area fitted is important, as in this application the width of the slit is large compared to the emitting area. Thus, it is the total number of emitting molecules in the slit that are measured directly, and an effective emitting area is needed to yield a column density. The assumptions included in the analysis are that the emission lines come from a slab of gas in LTE with a single emitting temperature. Multiple gas temperatures and/or opacity within the slab model can be included to more accurately reflect the shape of the rotation diagrams (Salyk et al. 2009). The LTE approach is widely used because it is simple and provides an estimate of molecular abundances and disk temperatures. Still, the modeling is unphysical. However, it would be useful to be able to relate the actual disk properties and gradients to the outputs fit using the rotation diagram. Here we use the disk models and their resultant spectra to do just that.

Specifically, we first use a grid of single temperature LTE slab models, with opacity, to simultaneously predict line fluxes from ^{12}CO and ^{13}CO (using an isotopologue ratio of 70 (Wilson 1999)). In plotting the rotation diagram we use the P branch emission lines for ^{12}CO, to mimic the wavelengths probed by majority of the data. We note, however, that using the R branch lines consistently predicted slightly lower rotational temperatures. Normalized integrated line fluxes from the slab models were compared to both the observed spectra and the model spectra, for which we already know the disk conditions. We determine the best fit temperature, column density, and emitting area from the rotation diagrams generated from each spectrum. There are two goals of this assessment. First, we can compare the data and models to see which predictions best match the data. Second, we can try to compare actual disk properties with those derived from this traditionally used tool.

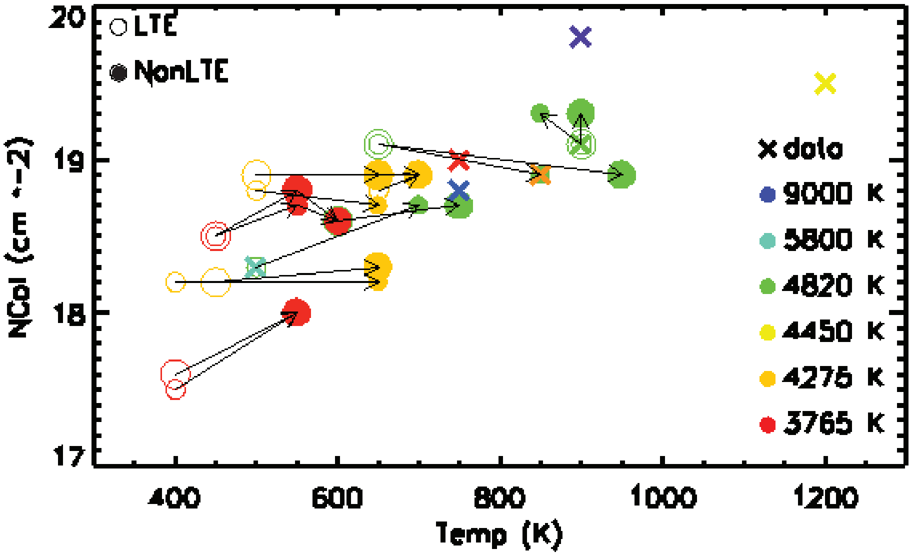

Figure 4.1: Rotation diagram best fit values for emitting temperature and column density for a suite of models (circles) and data (crosses). The models are presented for gas-to-dust ratios ranging from 100 to 10000. Larger circles correspond to models with $M_{disk} = 10^{-2}$ M_{star} and smaller circles depict the $M_{disk} = 10^{-3}$ M_{star} models. The arrows connect the LTE and non-LTE models for disks with the same initial conditions. The sample of disks with both ^{13}CO and ^{12}CO emission are marked on the plot as crosses.

Figure 4.1 shows that for the sample of disks with ^{13}CO emission lines, the derived column densities and temperatures are consistent with the model values. The emitting area in all fits was kept constant for simplicity. Comparing LTE and non-LTE models with the same initial conditions, connected by arrows, the non-LTE spectra generally prefer hotter rotational temperatures. This is consistent with overall shape of the spectra and with the high- to low-J flux ratios. However, one might expect that the LTE rotational temperatures would be hotter since the LTE emission from a disk is dominated by the hottest, innermost radii. This contradiction indicates that the LTE fits are not representative of the actual gas temperatures they sample. It is also clear that disks around hotter stars are best fit with higher rotational temperatures, but this trend only holds for the model spectra, not for the data. This difference probably reflects the unknown and varying disk properties within the data.

A final and intriguing observation from Fig. 4.1 is the difference of rotation diagram fits for disks of different masses. For all gas-to-dust ratios and stellar temperatures modeled, the disks with lower mass ($M_{disk} = 10^{-3}$ M_{star}), are best fit with column densities less than or equal to the column density of their higher mass counterparts. Overall, however, the column density differences are quite small, which makes sense since only the upper layers of the disk are being probed and the physical densities there should be similar.

This leads us to further investigate the deeper relationship between derived rotation diagram fits and the actual properties of the model disks. Now the area is allowed to vary, to find the true best fit to the spectra. Figure 4.2 demonstrates that for most of the disks we model, the true mass of the disk is indeed correlated to the characteristics fit by the rotation diagrams in that the higher mass disks require a larger column density, all other properties being held equal. This relationship confirms that the gas being probed is in the upper layers of the disk and the emission lines are not being saturated for disks with M_{disk} $= 10^{-3}$ - 10^{-2} M_{star}. Unfortunately, an actual disk mass is still difficult to derive from the M-band data, since so little of the disk volume is probed. Instead, we use optically thin millimeter-wave dust emission, combined with our near-IR-gleaned understanding of gas-to-dust ratios, to yield total disk gas mass. Ultimately, the non-LTE code will reveal local physical conditions at the disk surface at 0.1-10 AU, so we can consistently compare our gas (near-IR) and dust (mm-wave) mass estimates.

In summary, rotation diagrams are a reasonable first order interpretation of the data, but they integrate over the entire line width, losing valuable information contained therein. With some knowledge of the geometry of the (mostly) Keplerian field of the disk, we can use the line shapes to determine more precise spatial information and radial patterns. We

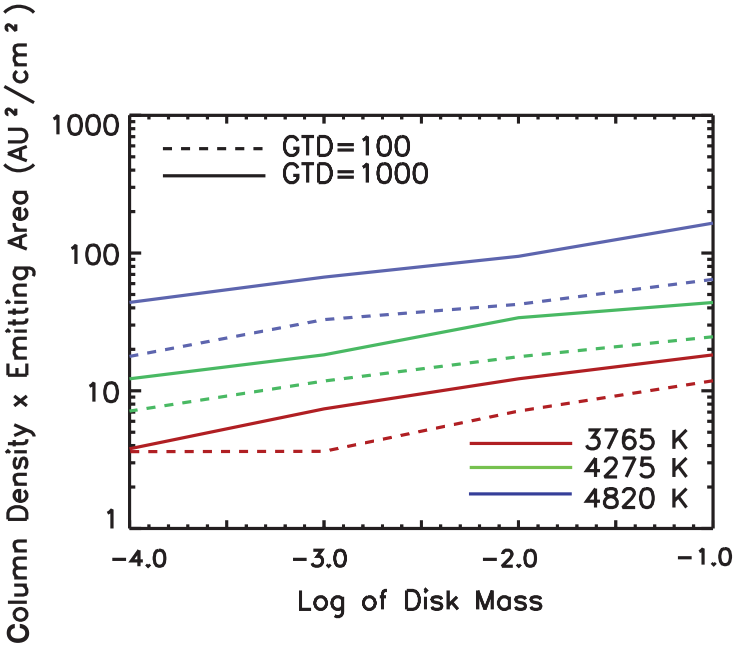

Figure 4.2: A comparison of input disk parameters and measured quantities from the resultant spectra. The column density and emitting area are fit from an LTE slab model optimized to simultaneously reproduce the ^{12}CO and ^{13}CO lines. The dashed and solid lines represent gas-to-dust ratios of 100 and 1000, respectively. Different stellar temperatures are indicated by color.

aim to exploit this information in the future, but for the purposes of this chapter we will examine the line shape as another observational constraint to the models.

4.5.1.2 Line Widths

The differences in the spectra generated from LTE or non-LTE gas can explain certain features in the data. Figure 4.3 demonstrates the differences in low- and high-J line profiles between LTE and non-LTE models, with a close-up look at the line shapes in Fig. 4.4. The plotted regions represent regions of high- and low-J P branch lines and are chosen to match the observational data ranges. Observations of DL Tau, as published in Salyk et al. (2011) are presented in the bottom panel for comparison.

Figure 4.4 shows the consistency of the double-peaked line profile in LTE, for both low-

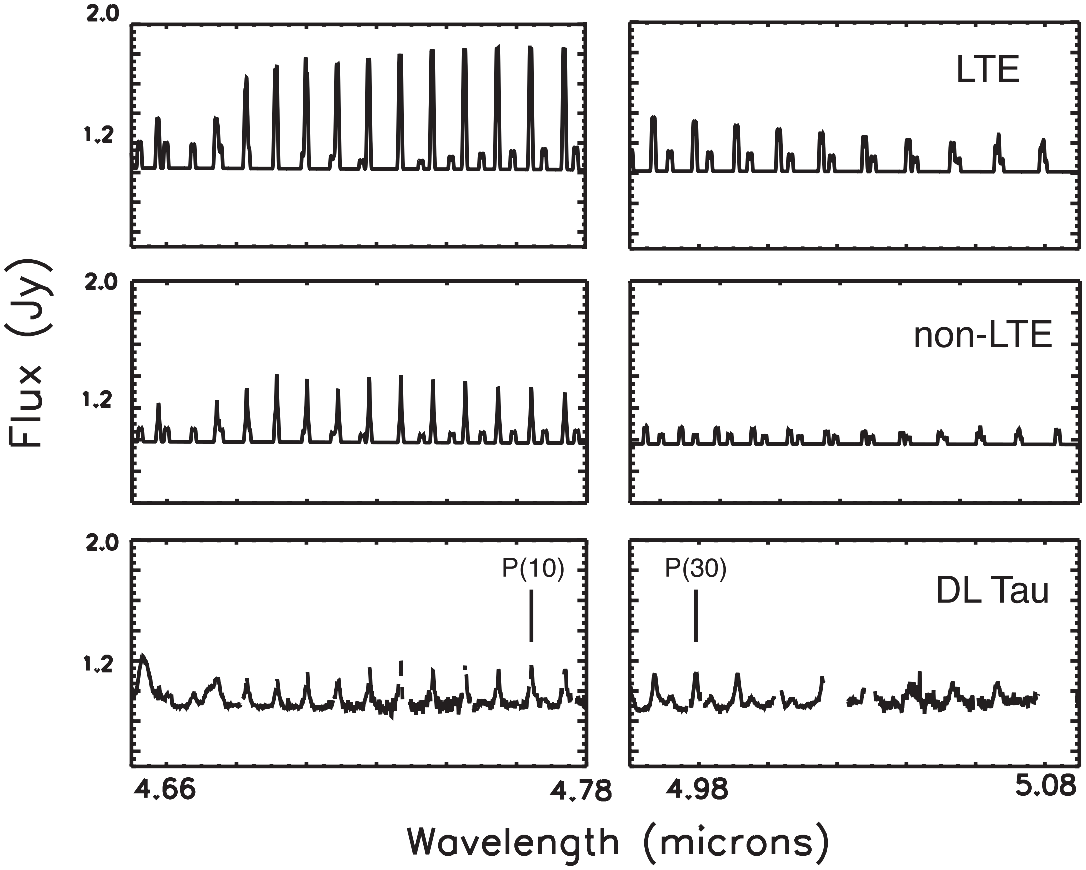

Figure 4.3: Top: CO rovibrational emission from a disk with $T_{star} = 4275$ K, a gas-to-dust ratio of 10000, $M_{disk} = 0.0001 M_{star}$ and $\alpha = 0$ in LTE, observed at an inclination of 25° from face on at a distance of 140 pc. Right and left panels represent the two wavelength regions observed for the data. Middle: Same for non-LTE emission. Bottom: Observed emission from DL Tau.

and high-J lines. The LTE behavior is easily explained by the fact that even at low-J the upper states of the transitions probed have an energy considerably larger than kT. The resulting exponential growth in population with temperature overwhelms any area decrease with radius, and so the LTE emission is dominated by the smallest, hottest radius in which CO is present. The separation of the peaks reveals the innermost gaseous radii of the disk, which corresponds to the dust sublimation radius in our models. The narrow range of radii important to the LTE emission results in the classical double peaked line profile for a Keplerian disk. Thus, line widths for LTE lines are similar for all lines (see solid lines in Fig.

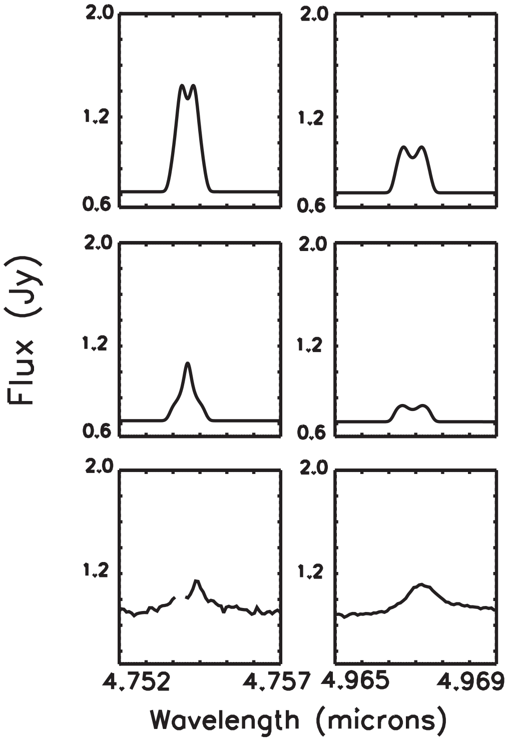

Figure 4.4: Same panels as in Figure 4.3, but for close-up examinations of the P(10) (left) and P(30) (right) line profiles.

4.5.) However, non-LTE lines show varying line profiles and single-peaked emission at low-J. Pontoppidan et al. (2011) suggest a slow molecular disk wind to explain the non-Keplerian line shapes seen in many disk sources (Salyk et al. 2011; Brown et al. 2013). While this can indeed be the case, Figure 4.3 shows that peaky emission at low-J can arises solely from thorough non-LTE modeling of the gas. The non-LTE computation accounts for IR fluorescence at much larger radii from a flared disk, resulting in a single-peaked profile in measurements that do not spatially resolve the CO emission.

Indeed, many of the observed sources have narrowly peaked features, and line widths are thus a useful tool for distinguishing disk properties. First and foremost, the narrow emission we see from so many sources demonstrates the need for a full calculation of the non-LTE excitation of the gas. Figure 4.5 plots the full width half maximum (FWHM) values of the

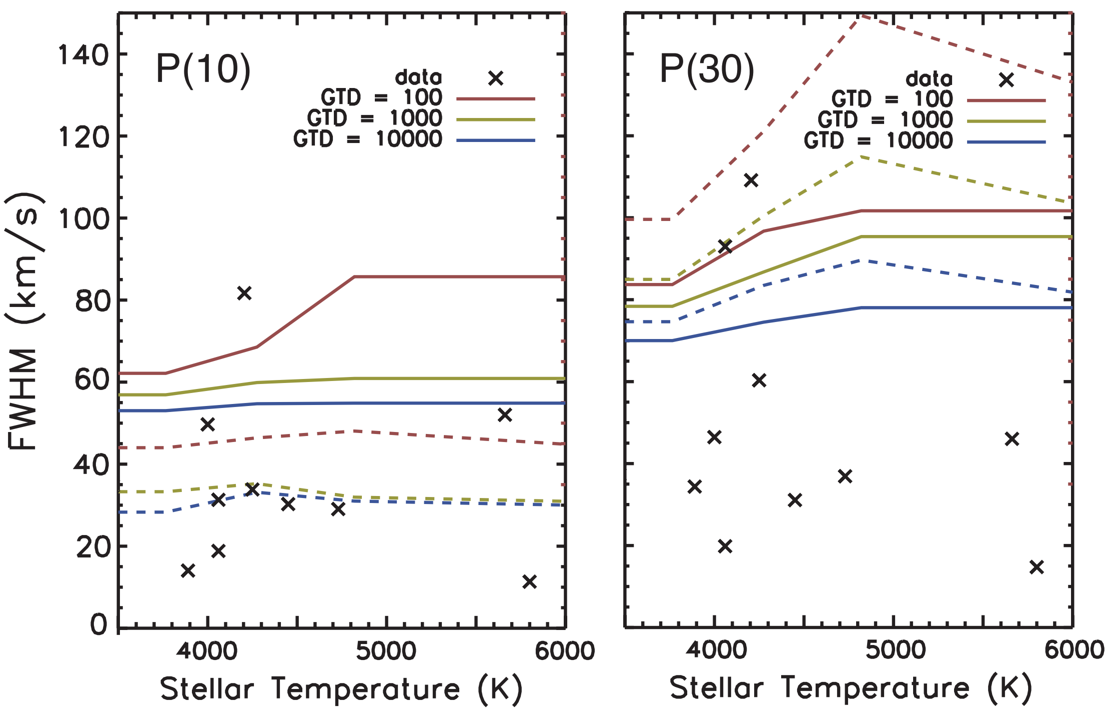

Figure 4.5: Values for the full width half maximum of the P(10) in LTE (solid lines) and non-LTE (dashed lines) for different values of the gas-to-dust ratio. FWHM values of actual disks are marked with crosses.

P(10) emission line for different stellar masses and gas-to-dust ratios. We use this line as our standard low-J line for comparison between model and data. For all conditions, the LTE (solid lines) widths are much larger than the non-LTE values. Corresponding data from a subset of sources is over plotted for comparison. Brown et al. (2013) similarly measure the P(8) emission lines of dozens of sources and categorize the line shapes into narrow, broad single peaked, broad, and double peaked. Of the 38 sources with clear emission, 31 of them were categorized as narrow to broad single peaked, with FWHM of less than 40 km/s (Brown et al. 2013). A non-LTE model is needed to fit the majority of the observed FWHM from low to moderate excitation lines, as the LTE models are too wide and even a disk wind profile reveals a wider line base from which the emission is launched. It is important to note that for all models, non-LTE and LTE, higher J lines are double peaked and broad, with FWHM values of ~ 85 km/s. P(30) is used for direct comparison in these and further analyses of the high-J emission.

4.5.2 Gas-to-dust Ratios

The gas-to-dust ratio in a disk can be used as a simple proxy for processes such as grain growth or dust settling, and is demonstrative of disk aging. The typical ISM value of $\sim$100 (Spitzer 1978) has been shown to be insufficient at explaining observed line-to-continuum ratios for the water emission detected with the Spitzer-IRS (Meijerink et al. 2009), so we test a range of values here. Constraining this parameter will help us look at disk evolution more precisely.

4.5.2.1 Line Widths

Between the non-LTE models, we can use line width to differentiate between disk properties. For low-J lines, a lower gas-to-dust ratio increases the line width (Figure 4.6), although the line widths derived from all non-LTE models are consistent with the data. This reveals that the ^{12}CO emission lines come from the upper parts of the disk, where increased gas at larger radii means more emission from those distances. Another similar trend has to do with the shape of the disk. The bottom panel in Fig. 4.6 depicts the variability of line width as a function of the flaring of the disk. The less flared disks tend to have wider emission lines. Physically this makes sense since one would expect a more flared disk to intercept emission at larger radii, giving narrower, but also stronger, emission lines. There is also a slight correlation between line width and stellar temperature, most likely simply due to the resultant radial temperature structure.

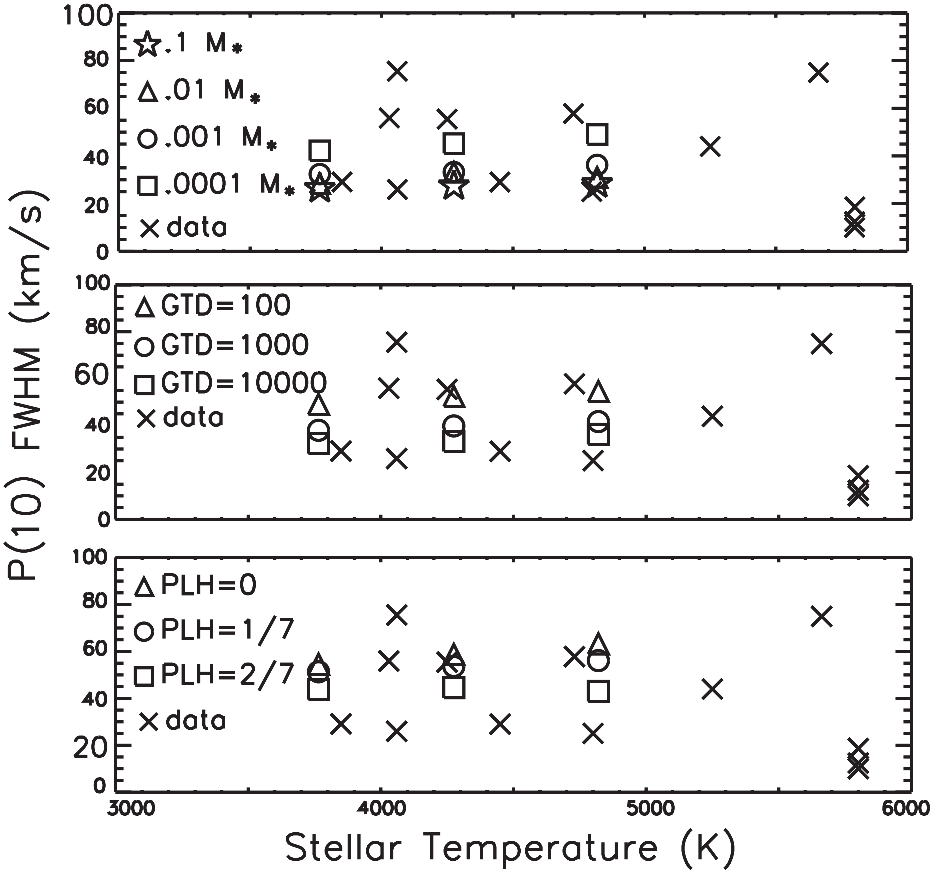

Figure 4.6: Line width of P(10) as a function of disk mass (top; expressed in units of M_{star}), gas-to-dust ratio (middle), and α, the coefficient of the scale height power law (bottom). Data are marked by crosses.

4.5.2.2 Line Strengths

One of the most obvious variations in line emission is in the strength of the lines. The line to continuum ratio of certain lines, as well as the relative line strengths between high- and low-J lines, can reveal underlying disk characteristics. As expected, emission line strengths are strongly dependent on the gas-to-dust ratio, with the most settled disks producing the largest line to continuum values at both high- and low-J (see Figures 4.7 and 4.8). This trend is especially strong for low-J lines, where we see the strength of the P(10) line can nearly double in strength with an increased gas-to-dust ratio. Again, this trend with gas-

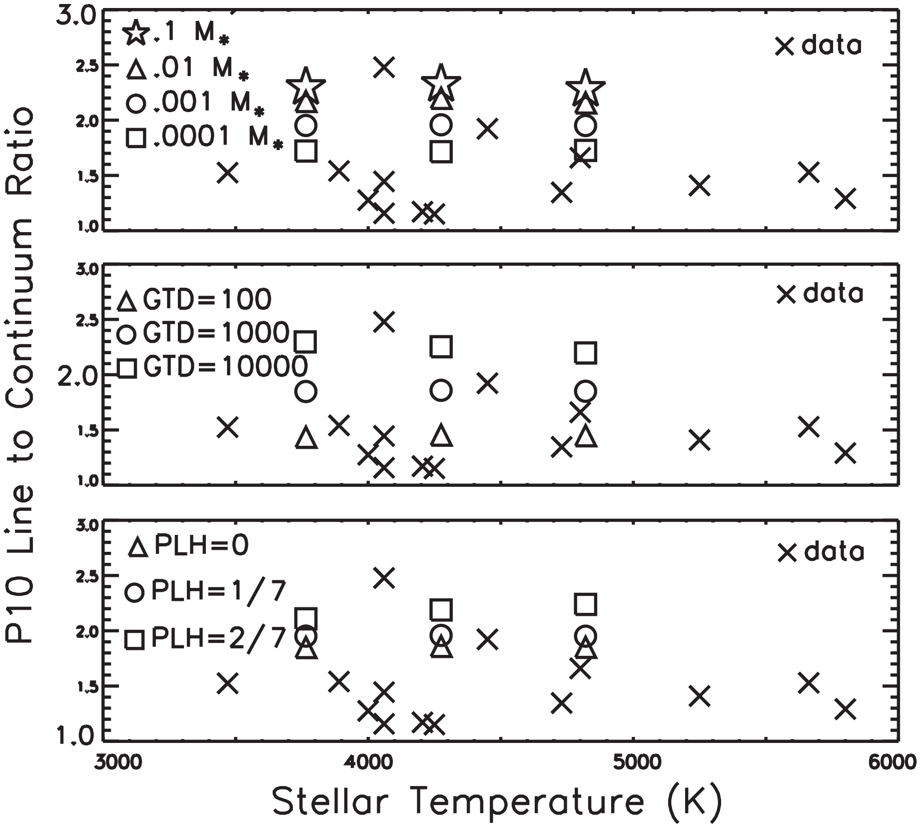

Figure 4.7: Integrated flux of the P(10) line from models (stars, triangles, circles, and squares) and data (crosses). The model fluxes vary with disk mass (top; given as a function of stellar mass), gas-to-dust ratio (middle), and flaring parameter, α (bottom).

to-dust ratio is indicative of the emission coming from the upper layers of the disk, where the gas content is directly related to the resultant emission strength.

There is also a predictable correlation between the fundamental emission line strength and both stellar temperature and disk mass. The correlation between disk flaring and line strength, seen in Figure 4.7, is interesting and will be addressed later in this chapter. In general, the models do a good job of matching the flux we see in the data, demonstrating that for rovibrational lines, temperature decoupling between the gas and dust is not necessary to explain the high-J emission, as is necessary when modeling the purely rotational lines (Bruderer et al. 2012; Fedele et al. 2013a,b; Meeus et al. 2013)

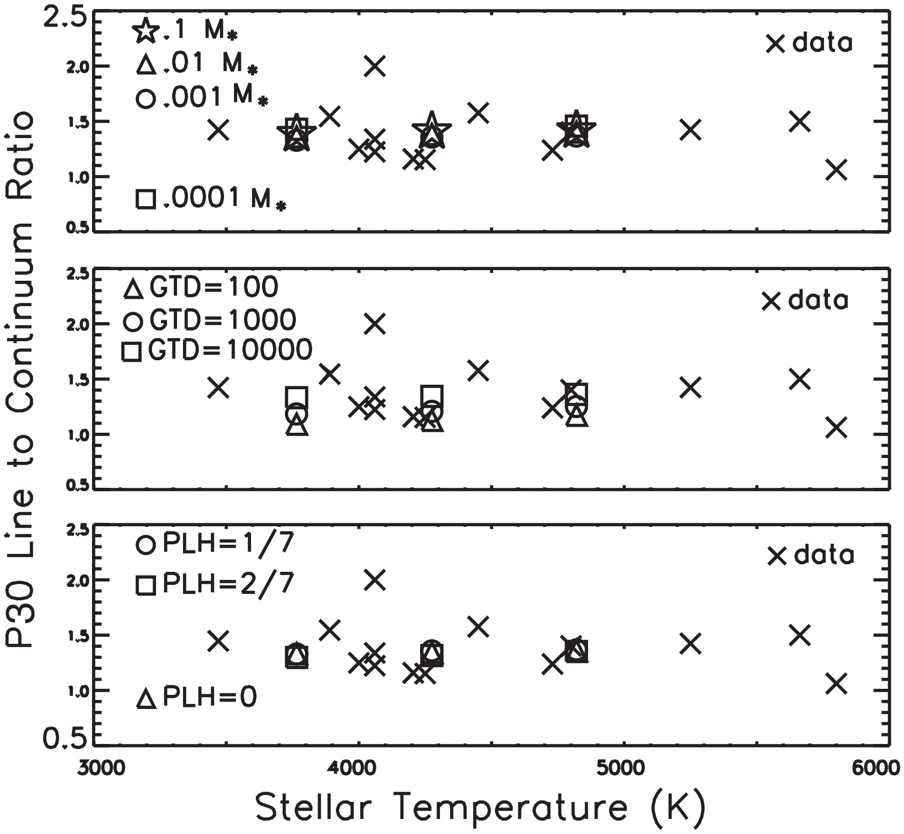

Figure 4.8: Same as Fig. 4.7, but for the P(30) line.

4.5.3 Isotopologues

While several isotopologues of CO have been observed in disks, ^{13}CO is the most isotopically substituted form of CO and has been detected in several sources (Salyk et al. 2011; Brown et al. 2013). Brown et al. (2013) use rotation diagrams to uniquely determine rotational temperatures for ^{12}CO and ^{13}CO and find lower rotational temperatures from the istopologue. They propose that the ^{13}CO gas emits from deeper in the disk, where it is colder. They posit that ^{13}CO cannot exist in the upper parts of the disk because it is not abundant enough to sufficiently self-shield (Brown et al. 2013). Here we use these emission lines as an additional constraint on our models, focusing on the observationally observed, low-J R-branch lines of ^{13}CO. Our findings also indicate distinct emission locations for the different isotopologues.

4.5.3.1 Line Widths

Just as for ^{12}CO, non-LTE line widths for ^{13}CO are generally narrow and single peaked. Fig. 4.9 compares the width of the R(5) line from ^{13}CO in the models, in which there lies a strong inverse correlation between disk mass and FWHM. This is due to the different emitting locations and excitation mechanisms of the two isotopologues. The moderate excitation v=1-0 ^{12}CO lines are significantly optically thick in the inner parts of the disk. Thus, any emitted line photons have a short mean free path, and the combined continuum and line radiation fields therefore contribute substantially to the ^{12}CO excitation. The rotational excitation temperatures of ^{12}CO reflect this, with values that are bracketed by the dust and gas kinetic temperatures (see also Thi et al. (2013)). Emission from ^{13}CO, however, is optically thin or nearly so above the dust photosphere, and so any collisional excitation will result in molecular emission that can escape the disk. Thus, ^{13}CO has a more significant excitation contribution from collisions compared to ^{12}CO, and has an excitation temperature more strongly determined by the kinetic temperature of the gas. By increasing disk mass, the radius at which the critical density is reached at/near the dust photosphere is also increased, thereby decreasing the FWHM of the emission lines. This effect is most clearly seen in the model simulations for the ^{13}CO emission lines, but is noticeably present in the moderate excitation ^{12}CO models as well. The lower states of the high-J transitions for either isotopologue have high critical densities, and so these lines are dominantly collisionally excited and therefore close(r) to LTE, as Figure 4.8 shows.

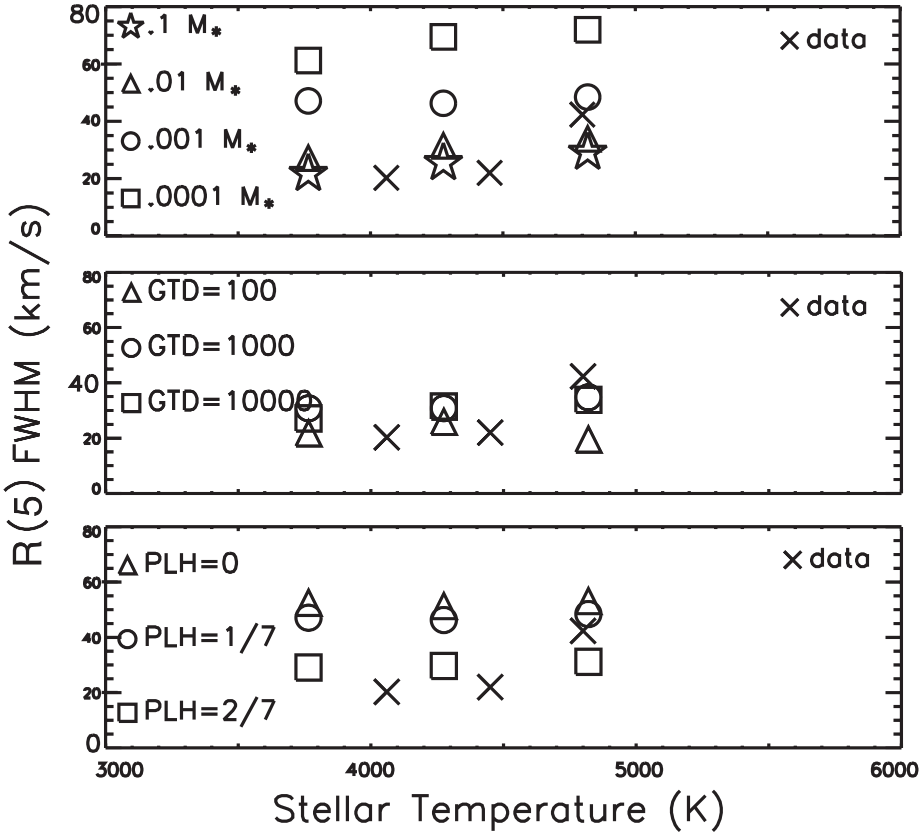

Figure 4.9: Full width half maximum values for the R(5) ^{13}CO emission line. The models are plotted as a function of disk mass (top; in units of stellar mass), gas-to-dust ratio (middle), and flaring parameter, α (bottom). Available data values are plotted as crosses.

4.5.3.2 Line Strengths

Figure 4.10 demonstrates that non-LTE modeling is also a good match to the isotopologue flux ratios between ^{13}CO and ^{12}CO that are seen in the data. Furthermore, the relative strength of the ^{13}CO lines increases for less flared disks, due to the decrease in radiative exposure (and excitation) of the ^{12}CO gas at the surface. The strongest correlation here, though, is that the line fluxes of ^{13}CO are dependent on the gas-to-dust ratio, with more settled disks producing more isotopologue emission. A settled disk, or one in which grains have grown in size, increases the column of gas above with the disk is optically thick. This correlation between gas to dust ratio and line strength confirms that the ^{13}CO is (mostly) optically thin and the emission strength is directly related to the depths probed in the disk. All of these factors reveal the collisionally dominated excitation of ^{13}CO.

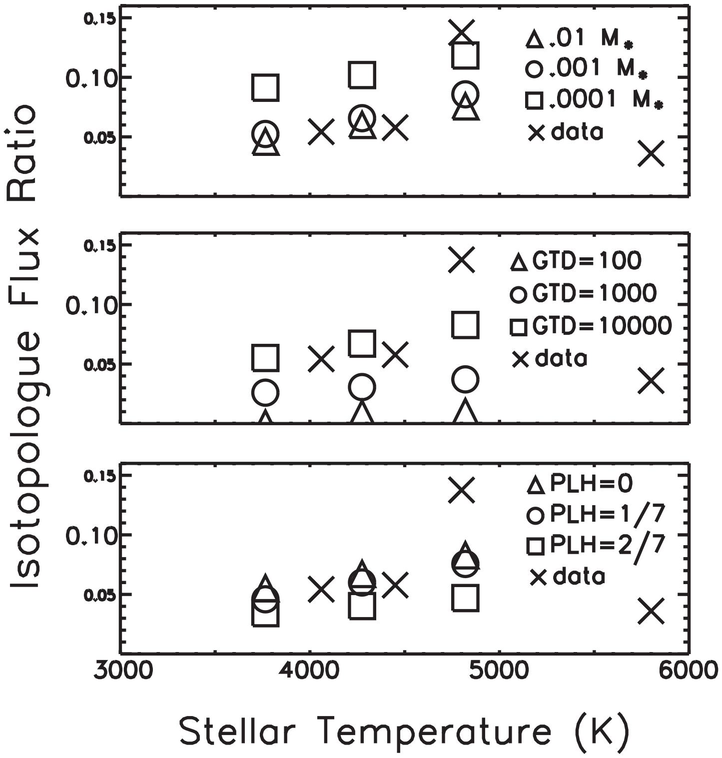

Figure 4.10: ^{13}CO/ ^{12}CO flux ratio of low-J lines. The flux in the R(5) lines of ^{13}CO and the P(10) line of ^{12}CO are compared as a function of disk mass (top; in units of stellar mass), gas-to-dust ratio (middle), and flaring parameter, α (bottom). Data are shown as crosses.

4.5.4 Other Model Trends

The shape of an emission line can be quite complex, and the observed spectra show profiles varying from strongly single-peaked lines with large line to continuum values, to weak, broad, double-peaked profiles (Salyk et al. 2011; Brown et al. 2013). However, Brown et al. (2013) find that there is a correlation between line strength and line width. The narrowest lines are also the strongest, a correlation our models strongly support, as shown in Figure 4.11. Now that it is clear that the ^{12}CO emission arises from the surface layers, we can interpret this trend as a consequence of the larger amounts of irradiated emitting area at larger radii, resulting in narrower and stronger line profiles.

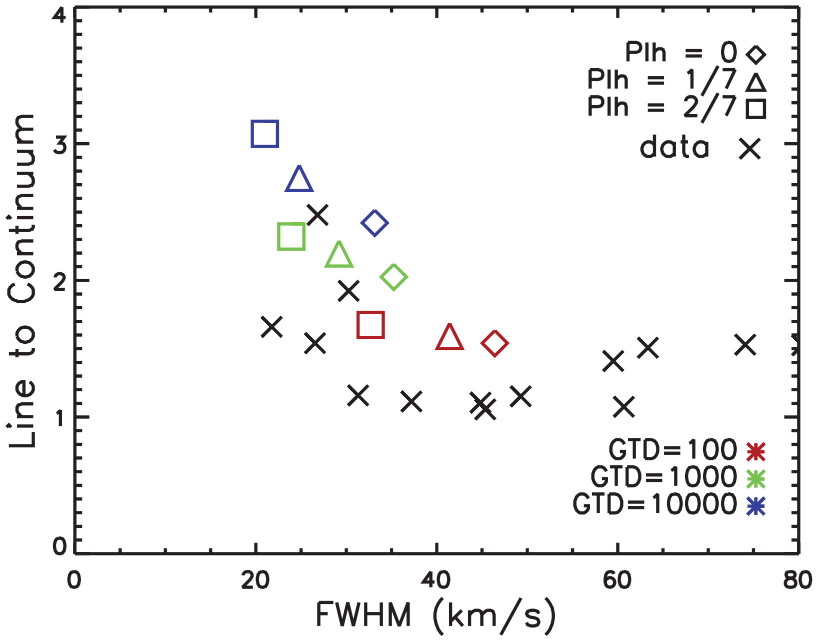

Figure 4.11: Plot of line to continuum ratio and line width for the data (crosses) and the models (triangles, circles and squares). Color corresponds to the gas to dust ratio and the symbol indicates the flaring parameter. Note the correlation between these two parameters for both the models and the data.

A final constraint provided by many of the data sources are the overtone emission lines (v = 2→1) (Salyk et al. 2011). However, Figure 4.12 shows that our models are unable to predict the shape of these emission lines correctly. The line widths from the data imply emission coming from the innermost parts of the disk, inside the dust sublimation radius and the proposed "puffed up inner rim" (Woitke et al. 2009). Our model does not address this part of the disk in detail, and therefore we underestimate the line widths. Our models do show that the vibrationally excited states are populated further out in the disk, which could be a result of their flared geometry and/or minimal UV fluorescence.

Fortunately, the line fluxes of the overtone emission lines are well-matched with the

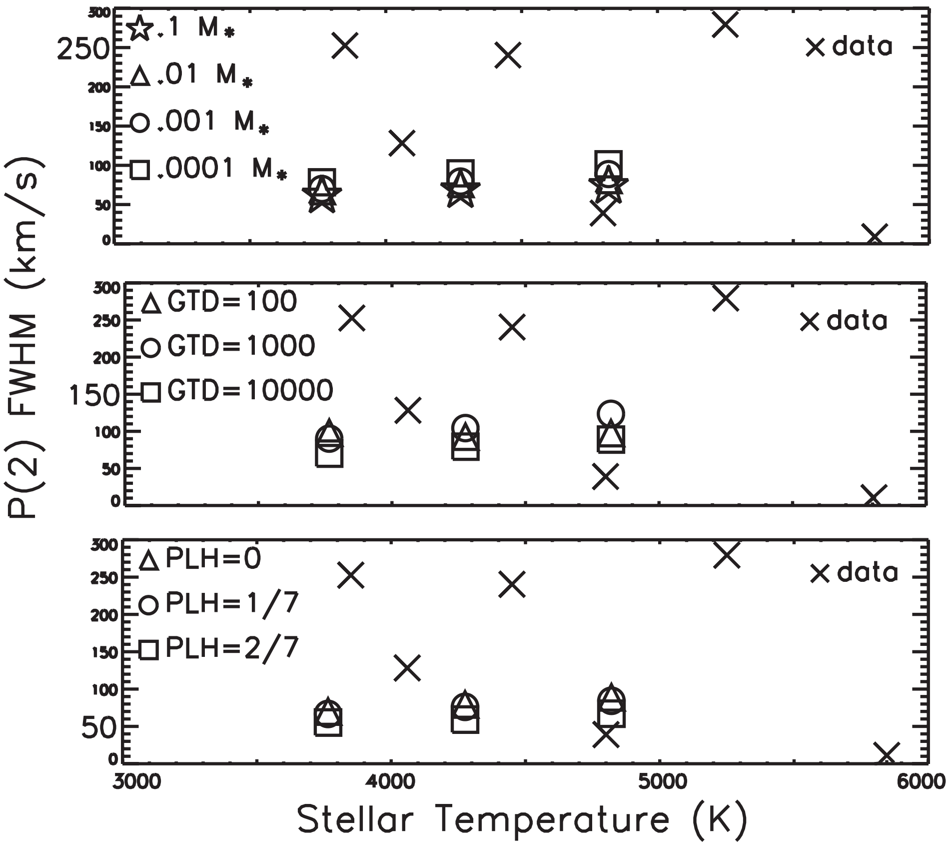

Figure 4.12: Full width half maximum of the P(2) overtone emission line. The models are plotted as a function of disk mass (top; in units of stellar mass), gas-to-dust ratio (middle), and flaring parameter, α (bottom). Available data values are plotted as crosses.

models. HerbigAe/Be stars have significant excess UV radiation that can pump the upper vibrational levels of CO but this UV excitation is not necessary to explain the T-Tauri lines. Our models show that these levels can be populated radiatively in the upper layers of the disk without UV fluorescence. Furthermore, the strength of the overtone emission lines is strongly correlated with the gas-to-dust ratio in the disk, as seen in Figure 4.13. Substantial grain growth or settling in the upper layers of the disk decreases the optical depth due to dust, permitting a larger gas column to reside above the dust photosphere. Since CO can self-shield itself against photodissociation, it can survive in such regions and the result is added optical depth in the hot band transitions as more of the gas is radiatively heated and therefore emissive.

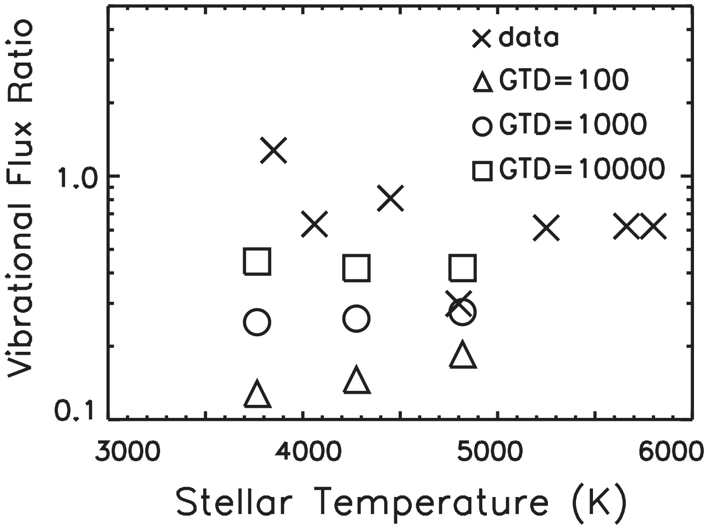

Figure 4.13: Ratio of integrated line fluxes for vibrational and fundamental line emission. The P(2) overtone line is compared to the P(10) fundamental. The symbols represent the three different gas-to-dust ratios tested and the crosses depict the data.

4.6 Discussion

Using observations to determine actual disk properties is critical for understanding disk evolution. CO is an abundant tracer of warm gas in disks and significant effort has been expended to understand the rotational and ro-vibrational spectra we see from this molecule (Salyk et al. 2009, 2011; Brown et al. 2013; Meeus et al. 2013). The goal of the work presented here is to harness the observations to constrain parameter space of disk properties, using a large model grid with an efficient non-LTE algorithm, before applying expensive computational time using a more complex thermophysical code applied to specific disk conditions. Here we have presented a suite of non-LTE models using only the most basic excitation mechanisms (collisions with molecular hydrogen and infrared pumping) that accommodate most of the observational constraints. Specifically, we have demonstrated the ability of a non-LTE codes without gas/dust temperature decoupling or excess UV radiation to adequately predict the strength of the ^{13}CO isotopologue and v=2-1 ^{12}CO hot band lines, as well as the strength and shape of the more intense fundamental v =1-0 ^{12}CO emission.

Previous CO studies have used LTE slab models to determine disk properties such as column density, emitting area, and temperature (Salyk et al. 2011). While these models are overly simplified and unphysical, they do provide a reasonable match to the observed integrated line strengths. Temperatures derived from ^{12}CO and ^{13}CO are both realistic and indicate that the optical depth of these lines differs greatly, with ^{13}CO line probing deeper in the disk. The cooler rotational temperatures obtained for ^{13}CO (Brown et al. 2013) are difficult to reconcile with thermal gradients in the upper surface layers of disks, however. We have shown that realistic model spectra, both LTE and non-LTE calculations, can be predicted well by an LTE slab model with opacity. Unfortunately, we do not yet understand the correlation between disk properties and rotation diagram fits. Although the column densities seem consistent relative to one another and the rotational temperatures increase with stellar temperature for the models, the data fits do not lead us to obvious conclusions. In part this may be due to the wide range of disk parameters that are present even for carefully selected isolated cTTs in the nearest star-forming regions. Still, rotation diagrams are easy tools for analyzing disks and have helped develop our understanding of disk emission.

Accurately modeling the gas temperature in disks has proven a difficult, but important quest. High-J transitions in the far-IR demonstrate the need for temperature decoupling between the gas and dust (Bruderer et al. 2012; Fedele et al. 2013a,b; Meeus et al. 2013). Sophisticated thermochemical models have been developed to determine the gas temperature structure, radially and vertically, in a self-consistent way (Woitke et al. 2009; Bruderer et al. 2012). However, we have shown that a model without an explicit gas temperature calculation does a good job matching the available rovibrational data. Indeed, the line fluxes of high-J fundamental transitions and hot band emission can be explained by the non-LTE excitation in which $T_{gas} = T_{dust}$. Interestingly, the fundamental transitions and hot band lines discussed below tend to have quite different line profiles, pointing to a different emitting location in the disk that is not yet reproduced in the models. The M-band emission lines studied here trace warmer gas in the inner disk, while the far-IR transitions probes radii $\geq$ 20AU (Bruderer et al. 2012). It is possible that the dust temperature remains warm enough close to the star that it is able to explain the relative strengths of the fundamental CO lines. The flaring in the disk, increasing at larger radii, will also decouple the gas and dust to a greater extent, requiring separate temperature calculations. Whatever the reason, our modeling demonstrates that the gas temperature does not need to decouple from the dust temperature in order to predict sufficient rovibrational line fluxes of CO.

The hot band emission lines, as well as those in the fundamental band, are well predicted by our models. With only collisions and IR fluorescence it is possible to excite populations of the $v = 2 \rightarrow 1$ levels to produce the line strengths that are observed in nearby sources. Previous studies have called for UV excitation to explain the vibrational ladder (Thi et al. 2013; Brown et al. 2013), but we show that non-LTE excitation with infrared pumping alone can account for these lines. Specifically, high gas-to-dust ratios create the strongest hot band emission. Substantially enhanced gas-to-dust ratios also appear necessary to explain the observed ^{13}CO emission lines. The significantly increased gas-to-dust ratios at large scale height likely reflect a combination of grain growth and settling, and the large mass surface densities that result near 1 AU are in accord with viscous accretion models for disks with sufficient total mass to form planetary systems.

There are a few limitations to the models in matching the observed line characteristics. For instance, the current models do not predict the width of the hot band lines seen in the data. The $v = 2 \rightarrow 1$ lines appear to be excited in the innermost parts of the disk, where the rotational broadening can be >100 km/s (Brown et al. 2013). The need for a puffed-up inner rim has been examined by others (Woitke et al. 2009), and might be the source of these wide, double peaked emission lines.

The low-J non-LTE lines from the models presented in this chapter are also narrower than the range of widths seen in the data. Thi et al. (2013) also encounter this problem when modeling non-LTE CO emission. Indeed, a non-LTE excitation calculation with only molecular hydrogen as a collisional partner is strongly affected by fluorescence in the outer parts of the disk. To mimic a Keplerian profile, the flaring parameter, α, must be decreased and the abundance of collisional partners, including atomic H and electrons, increased. These changes to the model will be discussed further in future work.

Overall, the models presented in this chapter do a good job, both qualitatively and quantitatively, of matching the available disk observable properties. Without modeling individual disks, we have garnered information about reasonable parameter constraints including higher-than-ISM gas-to-dust ratios and a range of plausible disk flaring. We have also identified the differing excitation mechanisms, and subsequently different dominant emission locations, for the ^{12}CO and ^{13}CO gas. The ^{12}CO emission closely traces the disk surface out to larger radii and is dominated by the local and stellar radiation fields. The ^{13}CO gas, unable to self-shield at the surface, has a low opacity until deeper in the disk, at which point collisional process are more efficient and control the molecular excitation. The two isotopologues reveal different local physical conditions of the disk, and together will help complete our understanding of protoplanetary environments.

Chapter 5

Future Prospects

The work presented above represents three separate observational avenues for understanding planet formation and evolution. Ultimately, the disciplines of astronomy and planetary science seek a unified model to explain all of the data, although the theoretical machinery and computational processing necessary are as yet unavailable. Instead, here I will focus on some particular advancements to the fields, and specifically to this work, that could develop our knowledge on the subject of planetary evolution.

5.1 Characterization of Exoplanetary Atmospheres

The direct detection of exoplanetary atmospheres is an emerging field with exciting possibilities. The work I have presented is merely the tip of the iceberg in terms of the capabilities of the facilities and modeling currently available.

5.1.1 Atmosphere Variability

The model atmosphere used in Chapter 3 was an informed prediction of the atmosphere of a hot-Jupiter. However, this represents just one thermochemical realization of viable atmospheric temperature, density, and molecular abundance structures (Seager & Deming 2010). Theorertical studies of the radiative transfer and chemistry in exoplanet atmospheres have been undertaken for more than a decade, and myriad of models exist (Burrows & Sharp 1999; Fortney et al. 2005; Seager et al. 2005). Chemical mixing ratios, temperature inversions, hazes, and hemispherical energy redistribution can all affect the photometric and spectroscopic signatures (Burrows et al. 2010; Madhusudhan & Seager 2010; Line et al. 2012; Marley et al. 2013). We intend to expand upon the exploratory work presented in Chapter 3 by testing our conclusions with a number of different models. In this manner we hope to probe the atmospheric composition and structure of the planets. This is a large step from where we are now – only confirming or denying the existence of a gaseous molecule and measuring the planet's velocity, and therefore mass.

From atmospheric models, we know that water vapor is expected in exoplanets and observations have confirmed this (Swain et al. 2009, 2010; Konopacky et al. 2013). CO, CH_4 and CO_2 are expected to be present as well, depending on the conditions near the exoplanet photosphere (Swain et al. 2009; Madhusudhan & Seager 2009). We have presented a thorough analysis using a planetary template dominated by water opacity, and some exploration into the presence of methane. The modeling of other molecules, especially those listed previously, is also planned. There may well be other abundant species to be measured, and we can use brown dwarfs to extrapolate which molecules we should find (Burgasser 2011). At disequilibrium temperatures around 1500 K we see many spectral types of brown dwarfs (McLean et al. 2001; Kirkpatrick et al. 2012). With similar temperatures, the same richness of chemical possibilities should exist in hot Jupiters. The presence of other molecules is already being explored.

In Chapter 3, I demonstrate the full analysis of a water-dominated atmosphere, and begin to assess the presence of methane in the atmosphere. Carbon dioxide would also be a good molecule to study at the wavelengths we have observed. Furthermore, the columns of CH_4 and CO_2 do not vary as quickly in the Earth's atmosphere as does H_2O, so these molecules might be easier to study from the ground in hot exoplanet atmospheres, where substantial molecular opacity structure is expected in wavelength regions where the terrestrial atmosphere is highly transmissive. Templates with realistic combinations of these molecules will also be tested.

5.1.2 Improvements to Current Techniques

A significant and troubling discovery that was made during the τ Boo b data analysis, after the observations were taken, involves the specific timing of the observations. We found that the correlation between the stellar and planetary template can bias the maximum likelihood of the planetary velocity. The incorrect signal we found is specific to the stellar and planetary templates used, as well as actual radial velocity of the planet (that is, the inclination angle of the system) and the phasing of the observations. We demonstrate above that the synthetic spectra can be used to identify the false signal. In the future, we plan to use the processing tools developed to build algorithms that ingest templates and plausible velocities to determine *a priori* the best phases to observe the target. We will use this information to guide future telescope proposal planning. We are also considering observational campaigns using more than one echelle setting. For example, the simple structure of CO might be best suited for velocity determination of a target, with the presence of other atmospheric molecules explored afterwards. This would lessen the likelihood of false signals and would provide more constraints on atmospheric characterization.

Forthcoming work includes the application of this technique to other planets, many of which have already been observed. We have acquired multiple epochs of L-band NIRSPEC data for *upsilon* And b, HD 88133 b, HD 187123 b, 51 Peg b, 61 Vir b, and HD 102195 b, as

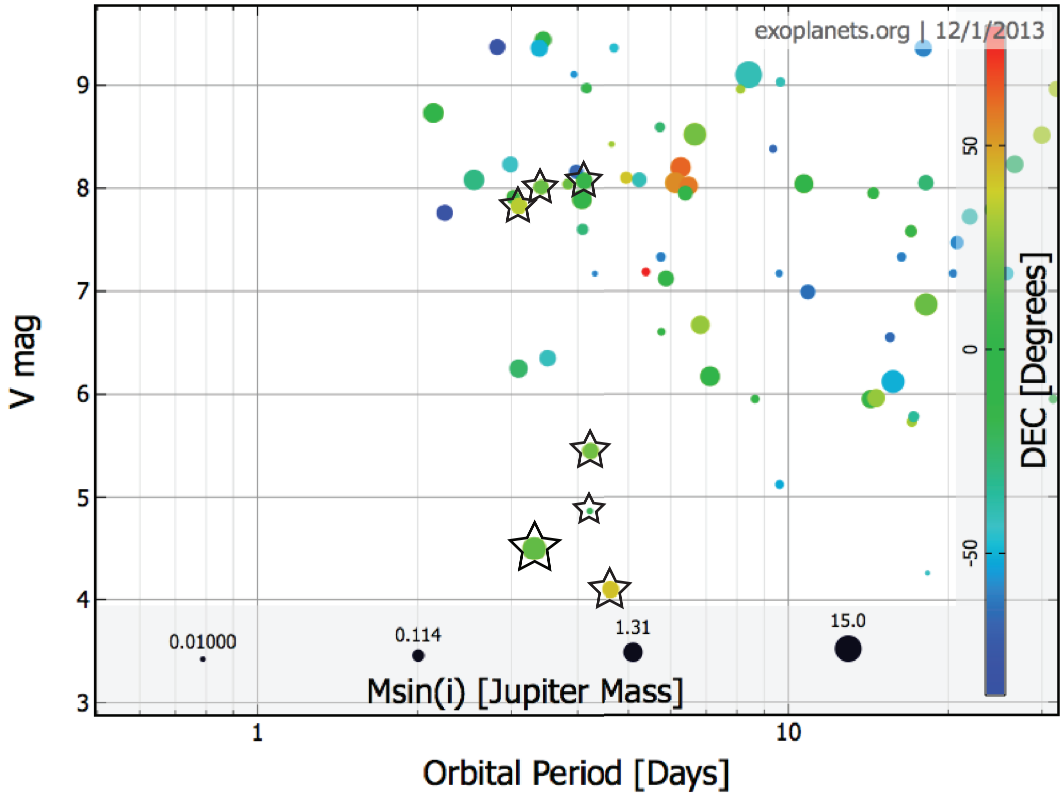

Figure 5.1: A plot showing the currently known, non-transiting planets in close-in orbits around bright stars. The size of the marker indicates minimum mass of the planet and the color scale corresponds to declination. Observed targets have been starred. Plot generated using data from www.exoplanets.org

well as 55 Cnc e which has now been found to transit. These targets are starred in Figure 5.1, which shows many other non-transiting targets with similar stellar fluxes and semi-major axes. We have observations on fainter targets (V_{mag} ∼8), but have not analyzed them yet. These results will help us understand the brightness limits required for these studies. In theory, provided we reach a high enough S/N for a target by integrating long enough, we can extract the exoplanet signal. However, with the short orbital periods of these targets we cannot combine data from observations greater than a few hours in duration because the velocity of the planet changes too much, smearing out the spectroscopic signal. Observing objects at quadrature allows for slightly longer integrations, but we are still limited. Still, there remains several targets of interest to be studied. Many of these reside in the Southern Hemisphere and so are inaccessible to NIRSPEC. We would therefore like to expand this project to use high-resolution spectrographs such as CRIRES, especially when its upgrade to a multi-order echelle format is complete. The single order of CRIRES on the VLT is not ideal for studying water or methane, whose lines are spread out through the L-band, but it is conceivable. We could also look for the signal temporally throughout several hours of data, as Brogi et al. (2012) did for CO in τ Boo b, and this would help break the CCF degeneracies we experienced. While Figure 5.1 demonstrates the currently viable parameter space of targets to be explored, the increased collecting area of upcoming telescopes such as the Thirty Meter Telescope and the Extremely Large Telescope will permit extensions of this technique to fainter primary stars. Additionally, the James Webb Space Telescope will provide mid-IR spectra to probe cooler planets, although decreased resolution may only allow atmospheric characterization for transiting planets. There is also some work with the MOSFIRE instrument at Keck to do “real-time” telluric correction, using multiple background stars in various slits, and collect planetary spectra, but this again has only begun for transiting planets.

5.2 Further Modeling of Protoplanetary Disks

5.2.1 Finding Protoplanets

Protoplanetary disks are going to be the key to understanding the full story of planet formation. For now we use the available molecular emission to model disk structure and constrain material abundances – infrared observations for the inner disk and a combination of far-infrared through radio observations for the outer disk. The next step, one that is already being explored, is the discovery and characterization of protoplanets themselves. While we have imaged hot young planets (HR 8799 by Marois et al. (2008) and detected planetary signatures in debris disks (Fomalhaut b by Kalas et al. (2005, 2009)), we are on the brink of discovering planetary embryos growing in gaseous disks. Very recently, disk asymmetries have been detected in transitional disks LkHα 330 and Oph IRS 48 that are suggestive of planetary companions (Isella et al. 2013; van der Marel et al. 2013). van der Marel et al. (2013) made their finding using the the Atacama Large Millimeter Array (ALMA), a powerful sub-mm array that is only beginning its journey. This facility will continue to probe the dust continuum and cool gas emission from disks, and will most certainly uncover asymmetries around other stars.

While the current maps are of dust continuum emission, the presence of a protoplanet can also affect the local gas (Pontoppidan et al. 2009; D'Angelo & Bodenheimer 2013). The state of the gas in the disks during planet formation is especially interesting. Photoevaporation can be an effective cause of gas dispersal in disks, which beckons the question of not only where, but also if, there is gas in the disk as oligarchs are forming. Our current understanding of giant planet formation has a large rock and ice core accreting gas only after reaching a minimum mass (several to ten Earth masses). The time to accrete enough material is still uncertain, and depends on several factors including disk viscosity and magnetohydronamic effects on turbulence and the opacity structure of the protoplanetary atmosphere, but Hubickyj et al. (2005) find 1 to 5 Myr to be possible for a Jupiter-like gas giant. Dissipation of the disk also depends on several factors, but estimates of the gas lifetime vary from a few to several million years (Haisch et al. 2001; Alexander et al. 2006). With the number of hot Jupiters found thus far, we know that there must be gas left after oligarch formation. Still, we would like to detect a planet forming in situ from its affect on the surrounding gas. Studying the state of dust and gas together in these systems will help confirm the origin of the asymmetry and develop the understanding of how such a companion interacts with the disk. Furthermore, while ALMA will soon become, by far, the most sensitive millimeter-wave observatory ever built, even it will only be able to image dust and gas down to several AU scales, that need to overlap directly with near- and mid-infrared spectroscopic studies of disks, in a handful of systems. More generally, high velocity resolution observations of disk gas with ALMA will be limited to radii of 10-20 AU from the central star in the nearest star-forming molecular clouds. To understand the disk at dense, inner, planet-forming distances, we need to probe the warm/hot gas.

Spectroastrometry is therefore a critical next step, both theoretically and experimentally, in studying planet formation. Spectroastrometry uses accurate measurements of the emission centroid of gas verses dust (or stellar radiation) made possible by the 2D format of echelle spectrographs. Thanks to recent AO systems mounted on existing ground-based telescopes, such as Keck and the VLT, 100 micro-arcsecond resolution or better is possible (Pontoppidan et al. 2008). In nearby disks, this corresponds to sub-AU sizes and it is finally possible to spatially resolve the inner radii of disks. In addition to studying gas asymmetries in classical disks, spectroastrometry can be applied to measuring gaps in transitional disks, where the dust and/or gas has already been cleared. Another use will be probing gas in non-Keplerian orbits, as can result from evaporative flows or accretion infall (Alexander et al. 2006; Pontoppidan et al. 2011). This will be especially illustrative in determining disk structure and molecular abundances.

5.2.2 Modifications to Current Codes

The studies presented in Chapter 4 have focused on carbon monoxide, a stable, abundant molecule with vibrational and rotational emission measured from numerous disk sources. However, several other simple molecules have been detected and warrant further study. We have used CO here to constrain certain disk parameters – principally the gas-to-dust ratio and disk mass – in order to begin nailing down certain critical characteristics of the disk. The next step is modeling other molecules such as water and HCN, whose abundance structure will vary greatly due to temperature gradients in the disk, as well as photochemistry. The adaptable excitation code presented here has been written such that any molecular data file, in the LAMDA format, will be accepted and the emission modeled. The modeling of several molecules simultaneously will help further determine the disk properties and dominant physical, thermal, and chemical properties at play.

There are still several improvements that we are considering for our disk modeling. A possible extension of the code would be to turn the 1 by 1D excitation code into 2D code with radial communication. This extension has thus far been foregone because the differential Keplerian rotation incites strong radial opacity gradients. However, Pontoppidan et al. (2011) show that wide-angle disk winds could redistribute a significant fraction of inner disk gas to the outer radii during the lifetime of a disk. This material transport must be considered, but does not necessarily imply inter-radii line excitation. Accretion onto the central star and photoevaporation are other radial transport processes that need to be fully modeled in order to properly constrain disk lifetimes and molecular abundances.

Further studies that we have in mind will directly address our observational constraints as follows. The current non-LTE models do not adequately model the full suite of line shapes presented by the high-resolution data. While we can replicate the peaky line profiles, some of these have been shown to originate in disk winds (Bast et al. 2011; Pontoppidan et al. 2011). Winds were not included in these studies, but a RADLite implementation for such flows is available and will be used in the future. A further weakness of the models presented here is the inability to mimic the Keplerian profiles in non-LTE. We believe that by experimenting with more shadowed disks and/or higher fractions of collisional partners we can remedy this problem. Another important disk characteristic that was not explored here, but that can strongly affect line shapes and strengths is the disk inclination. We would like to explore the degeneracies this can lead to in our results, with the hopes that sub-mm measurements along with spectroastrometry will conclusively determine disk inclinations and this will be a known parameter when modeling.

In addition, the precision of our data analysis for the disk observations thus far is not as good as it could be. We currently use a spectrally featureless hot star as our atmospheric standard, which we divide out from our disk observations taken with the same settings. Despite the aim of matching air masses, the temporal and spatial variations in the atmosphere dictate that the telluric lines will never exactly match. For the strong CO lines presented here, the resulting noise is permissible, but ultimately we will want to improve our telluric removal on the disk data. We have plans to use the TERRASPEC code to reanalyze some previous disk observations, particularly at K and L-bands, to try get better constraints on other molecules such as OH and H_2O. We are also searching for the presence of hydrogen fluoride and methane, which have not been detected in the warm gas, but are expected to be present in small quantities. The evolution of methane, in particular, is of great interest to planet formation since it has been found in exoplanets and Kuiper Belt objects alike. Mandell et al. (2008) achieve dynamic ranges on disk observations consistent with shot noise statistics by using an atmospheric retrieval code, allowing accurate line profiles to be measured. A precise telluric removal will provide higher fidelity data, which can be used to constrain molecular abundances as well as line shapes and further guide the disk modeling.

5.2.3 Areas of Continued Interest

Findings by recent Herschel studies have emphasized the need for precise calculation of the gas temperature in the surface layers of the disk. An immediate addition to our work can be to solve the hydrostatic thermal balance of the gas at these altitudes and use that temperature prescription. While this will be a significant step towards a more realistic gas temperature, there is a detailed heating and cooling balance that must ultimately be considered. This full thermochemical approach has been tried by some, but has not been able to fully match the observational constraints (Woitke et al. 2009). Futhermore, Woitke et al. (2009) invoke additional UV radiation to heat the gas in their models, which could lead to rapid disk dissipation and prevent giant planet formation. To begin a proper treatment of the gas temperature, we can focus on one species at a time and its contribution to the thermal balance, starting with the strongest disk coolants: neutral oxygen, H_2 and CO. Fortunately, this can be localized in the surface layers where the gas and dust and decoupled, saving some processing time. The future of modeling will likely need to a highly iterative process between radiation, chemistry, excitation, emission, and molecular transport, requiring large computational facilities.

As mentioned in Chapter 4, disk winds are an area of emerging importance for protoplanetary disks. The origin of these winds likely comes from a photoevaporative flow, however the driving mechanism and the duration of this phenomenon is yet unknown. Stellar winds described by Alexander et al. (2006) excite ionized surface layers that gravitationally escape. However, the blueshifted nature of the lines does not match the spectoastrometric molecular line profiles (Pontoppidan et al. 2011). Furthermore, Acke et al. (2005) measure atomic emission in Keplerian rotation in disks that are predicted to have molecular disk winds. This uncertainty only drives the need for a 3D non-LTE disk model that can simultaneously predict all emission lines from visible to sub-mm, and from all parts of the disk. This will probably be done with grids that can spend more time developing the physics and chemistry in sub-sections of the disk, such as at the surface, the inner rim, and near accreting protoplanets. The near-IR spectroastrometry and ALMA image cubes will almost certainly provide more data than theoretical modeling can accommodate, at least for the next several years. Ultimately, the combined power of high spatial and spectral resolution observations and models/theory capable of treating the length and time scales involved will yield a self-consistent understanding of protoplanetary disk, and thus of the formation of planetary systems.

Bibliography

Abrams, M. C., Goldman, A., Gunson, M. R., Rinsland, C. P., & Zander, R. 1996, Appl. Opt., 35, 2747

Acke, B., van den Ancker, M. E., & Dullemond, C. P. 2005, A&A, 436, 209

Aikawa, Y. 2013, Chemical Reviews, http://pubs.acs.org/doi/pdf/10.1021/cr4003193

Alexander, R. D., Clarke, C. J., & Pringle, J. E. 2006, MNRAS, 369, 229

Balbus, S. A., & Hawley, J. F. 1991, ApJ, 376, 214

Barber, R. J., Tennyson, J., Harris, G. J., & Tolchenov, R. N. 2006, MNRAS, 368, 1087

Barkume, K. M., Brown, M. E., & Schaller, E. L. 2006, ApJL, 640, L87

Barman, T. S., Hauschildt, P. H., & Allard, F. 2001, ApJ, 556, 885

—. 2005, ApJ, 632, 1132

Barucci, M. A., Merlin, F., Dotto, E., Doressoundiram, A., & de Bergh, C. 2006, A&A, 455, 725

Baskin, N. J., Knutson, H. A., Burrows, A., et al. 2013, ApJ, 773, 124

Basri, G., & Reiners, A. 2006, AJ, 132, 663

Bast, J. E., Brown, J. M., Herczeg, G. J., van Dishoeck, E. F., & Pontoppidan, K. M. 2011, A&A, 527, A119

Batalha, N. M., Rowe, J. F., Bryson, S. T., et al. 2013, ApJS, 204, 24

Bender, C. F., Mahadevan, S., Deshpande, R., et al. 2012, ApJL, 751, L31

Bergin, E. A. 2011, The Chemical Evolution of Protoplanetary Disks, ed. P. J. V. Garcia, 55–113

Berta, Z. K., Charbonneau, D., Désert, J.-M., et al. 2012, ApJ, 747, 35

Birkby, J. L., de Kok, R. J., Brogi, M., et al. 2013, ArXiv e-prints, arXiv:1307.1133

Blake, G. A., & Boogert, A. C. A. 2004, ApJL, 606, L73

Borucki, W. J., Koch, D. G., Basri, G., et al. 2011, ApJ, 736, 19

Brittain, S. D., Rettig, T. W., Simon, T., & Kulesa, C. 2005, ApJ, 626, 283

Brittain, S. D., Rettig, T. W., Simon, T., et al. 2003, ApJ, 588, 535

Brittain, S. D., Simon, T., Najita, J. R., & Rettig, T. W. 2007, ApJ, 659, 685

Brogi, M., Snellen, I. A. G., de Kok, R. J., et al. 2012, Nature, 486, 502

Brown, J. M., Herczeg, G. J., Pontoppidan, K. M., & van Dishoeck, E. F. 2012, ApJ, 744, 116

Brown, J. M., Pontoppidan, K. M., van Dishoeck, E. F., et al. 2013, ApJ, 770, 94

Brown, M. E., Barkume, K. M., Ragozzine, D., & Schaller, E. L. 2007, Nature, 446, 294

Brown, M. E., Schaller, E. L., & Fraser, W. C. 2011, ApJL, 739, L60

Brown, M. E., Bouchez, A. H., Rabinowitz, D., et al. 2005, ApJL, 632, L45

Brown, R. A. 2011, ApJ, 733, 68

Brown, R. H., Cruikshank, D. P., & Morrison, D. 1982a, Nature, 300, 423

Brown, R. H., Morrison, D., Telesco, C. M., & Brunk, W. E. 1982b, Icarus, 52, 188

Bruderer, S., van Dishoeck, E. F., Doty, S. D., & Herczeg, G. J. 2012, A&A, 541, A91

Buratti, B. J. 1995, J. Geophys. Res., 100, 19061

Burgasser, A. J. 2011, in IAU Symposium, Vol. 276, IAU Symposium, ed. A. Sozzetti, M. G. Lattanzi, & A. P. Boss, 135–142

Burrows, A., Rauscher, E., Spiegel, D. S., & Menou, K. 2010, ApJ, 719, 341

Burrows, A., & Sharp, C. M. 1999, ApJ, 512, 843

Butler, R. P., Marcy, G. W., Williams, E., Hauser, H., & Shirts, P. 1997, ApJL, 474, L115

Butler, R. P., Wright, J. T., Marcy, G. W., et al. 2006, ApJ, 646, 505

Carr, J. S., & Najita, J. R. 2008, Science, 319, 1504

Charbonneau, D., Brown, T. M., Latham, D. W., & Mayor, M. 2000, ApJL, 529, L45

Charbonneau, D., Brown, T. M., Noyes, R. W., & Gilliland, R. L. 2002, ApJ, 568, 377

Chiang, E. I., & Goldreich, P. 1997, ApJ, 490, 368

Christie, W. H., & Wilson, O. C. 1938, ApJ, 88, 34

Clough, S. A., Shephard, M. W., Mlawer, E. J., et al. 2005, J. Quant. Spectrosc. Radiat. Transfer, 91, 233

Collier Cameron, A., Horne, K., Penny, A., & James, D. 1999, Nature, 402, 751

Crossfield, I. J. M., Barman, T., Hansen, B. M. S., & Howard, A. W. 2013, ArXiv e-prints, arXiv:1308.6580

Cushing, M. C., Vacca, W. D., & Rayner, J. T. 2004, PASP, 116, 362

D'Angelo, G., & Bodenheimer, P. 2013, ApJ, 778, 77

Dullemond, C. P., & Dominik, C. 2004, A&A, 417, 159

Dullemond, C. P., Hollenbach, D., Kamp, I., & D'Alessio, P. 2007, Protostars and Planets V, 555

Dumas, C., Carry, B., Hestroffer, D., & Merlin, F. 2011, A&A, 528, A105+

Favre, C., Cleeves, L. I., Bergin, E. A., Qi, C., & Blake, G. A. 2013, ApJL, 776, L38

Fedele, D., Bruderer, S., van Dishoeck, E. F., et al. 2013a, ApJL, 776, L3

—. 2013b, ArXiv e-prints, arXiv:1308.1578

Flock, M., Turner, N., Dzyurkevich, N., & Klahr, H. 2011, in IAU Symposium, Vol. 276, IAU Symposium, ed. A. Sozzetti, M. G. Lattanzi, & A. P. Boss, 418–419

Flower, D. R. 2001, MNRAS, 328, 147

Fornasier, S., Lellouch, E., Müller, T., et al. 2013, A&A, 555, A15

Fortney, J. J., Marley, M. S., Lodders, K., Saumon, D., & Freedman, R. 2005, ApJL, 627, L69

Goldreich, P., & Sari, R. 2003, ApJ, 585, 1024

Goldreich, P., & Tremaine, S. 1980, ApJ, 241, 425

Gordon, K. D., Rieke, G. H., Engelbracht, C. W., et al. 2005, PASP, 117, 503

Grevesse, N., Asplund, M., & Sauval, A. J. 2007, Space Sci. Rev., 130, 105

Gustafsson, B., Edvardsson, B., Eriksson, K., et al. 2008, A&A, 486, 951

Haisch, Jr., K. E., Lada, E. A., & Lada, C. J. 2001, ApJL, 553, L153

Hapke, B. 1993, Theory of reflectance and emittance spectroscopy

Hase, F., Demoulin, P., Sauval, A. J., et al. 2006, J. Quant. Spectrosc. Radiat. Transfer, 102, 450

Henning, T., & Semenov, D. 2013, Chemical Reviews, 113, 9016

Henry, G. W., Marcy, G. W., Butler, R. P., & Vogt, S. S. 2000, ApJL, 529, L41

Herbig, G. H., & Turner, B. A. 1953, ApJ, 118, 477

Hillier, J., Helfenstein, P., Verbiscer, A., et al. 1990, Science, 250, 419

Ho, S., & Turner, E. L. 2011, ApJ, 739, 26

Holsapple, K. A. 2007, Icarus, 187, 500

Holtzman, J. A., Burrows, C. J., Casertano, S., et al. 1995, PASP, 107, 1065

Howard, A. W. 2013, Science, 340, 572

Hubickyj, O., Bodenheimer, P., & Lissauer, J. J. 2005, Icarus, 179, 415

Isella, A., Pérez, L. M., Carpenter, J. M., et al. 2013, ApJ, 775, 30

Jewitt, D. C., & Luu, J. X. 2001, AJ, 122, 2099

Jorissen, A., Mayor, M., & Udry, S. 2001, A&A, 379, 992

Kalas, P., Fitzgerald, M. P., Clampin, M., et al. 2009, in Bulletin of the American Astronomical Society, Vol. 41, American Astronomical Society Meeting Abstracts #213, 351.02

Kalas, P., Graham, J. R., & Clampin, M. 2005, Nature, 435, 1067

Karkoschka, E. 2001, Icarus, 151, 51

Kenyon, S. J., & Hartmann, L. 1995, ApJS, 101, 117

Kirkpatrick, J. D., Gelino, C. R., Cushing, M. C., et al. 2012, ApJ, 753, 156

Knutson, H. A., Lewis, N., Fortney, J. J., et al. 2012, ApJ, 754, 22

Konopacky, Q. M., Barman, T. S., Macintosh, B. A., & Marois, C. 2013, Science, 339, 1398

Lacerda, P. 2009, AJ, 137, 3404

Lacerda, P., Jewitt, D., & Peixinho, N. 2008, AJ, 135, 1749

Lacerda, P., & Jewitt, D. C. 2007, AJ, 133, 1393

Latham, D. W., Mazeh, T., Carney, B. W., et al. 1988, AJ, 96, 567

Latham, D. W., Mazeh, T., Stefanik, R. P., et al. 1992, AJ, 104, 774

Lebofsky, L. A., Sykes, M. V., Tedesco, E. F., et al. 1986, Icarus, 68, 239

Leinhardt, Z. M., Marcus, R. A., & Stewart, S. T. 2010, ApJ, 714, 1789

Lellouch, E., Kiss, C., Santos-Sanz, P., et al. 2010, A&A, 518, L147+

Lellouch, E., Santos-Sanz, P., Lacerda, P., et al. 2013, A&A, 557, A60

Levison, H. F., & Morbidelli, A. 2003, Nature, 426, 419

Licandro, J., Pinilla-Alonso, N., Pedani, M., et al. 2006, A&A, 445, L35

Lin, D. N. C., & Papaloizou, J. 1986, ApJ, 309, 846

Line, M. R., Zhang, X., Vasisht, G., et al. 2012, ApJ, 749, 93

Machida, M. N., Kokubo, E., Inutsuka, S.-I., & Matsumoto, T. 2010, MNRAS, 405, 1227

Madhusudhan, N., & Seager, S. 2009, ApJ, 707, 24

—. 2010, ApJ, 725, 261

Mandell, A. M., Mumma, M. J., Blake, G. A., et al. 2008, ApJL, 681, L25

Marcy, G., Butler, R. P., Fischer, D., et al. 2005, Progress of Theoretical Physics Supplement, 158, 24

Markwardt, C. B. 2009, in Astronomical Society of the Pacific Conference Series, Vol. 411, Astronomical Data Analysis Software and Systems XVIII, ed. D. A. Bohlender, D. Durand, & P. Dowler, 251

Marley, M. S., Ackerman, A. S., Cuzzi, J. N., & Kitzmann, D. 2013, ArXiv e-prints, arXiv:1301.5627

Marois, C., Macintosh, B., Barman, T., et al. 2008, Science, 322, 1348

Mayor, M., & Queloz, D. 1995, Nature, 378, 355

McLean, I. S., Becklin, E. E., Figer, D. F., et al. 1995, in Society of Photo-Optical Instrumentation Engineers (SPIE) Conference Series, Vol. 2475, Society of Photo-Optical Instrumentation Engineers (SPIE) Conference Series, ed. A. M. Fowler, 350–358

McLean, I. S., Prato, L., Kim, S. S., et al. 2001, ApJL, 561, L115

Meeus, G., Salyk, C., Bruderer, S., et al. 2013, ArXiv e-prints, arXiv:1308.4160

Meijerink, R., Pontoppidan, K. M., Blake, G. A., Poelman, D. R., & Dullemond, C. P. 2009, ApJ, 704, 1471

Merín, B., Brown, J. M., Oliveira, I., et al. 2010, ApJ, 718, 1200

Merlin, F., Guilbert, A., Dumas, C., et al. 2007, A&A, 466, 1185

Millis, R. L., Wasserman, L. H., Franz, O. G., et al. 1987, Icarus, 72, 507

Mommert, M., Harris, A. W., Kiss, C., et al. 2012, A&A, 541, A93

Najita, J., Carr, J. S., & Mathieu, R. D. 2003, ApJ, 589, 931

Najita, J. R., Ádámkovics, M., & Glassgold, A. E. 2011, ApJ, 743, 147

Neufeld, D. A., & Hollenbach, D. J. 1994, ApJ, 428, 170

Pfeiffer, R. J. 1977, AJ, 82, 734

Pinilla-Alonso, N., Brunetto, R., Licandro, J., et al. 2009, A&A, 496, 547

Poelman, D. R., & Spaans, M. 2005, A&A, 440, 559

Pontoppidan, K. M., Blake, G. A., & Smette, A. 2011, ApJ, 733, 84

Pontoppidan, K. M., Blake, G. A., van Dishoeck, E. F., et al. 2008, ApJ, 684, 1323

Pontoppidan, K. M., Meijerink, R., Dullemond, C. P., & Blake, G. A. 2009, ApJ, 704, 1482

Qi, C., Öberg, K. I., Wilner, D. J., et al. 2013, Science, 341, 630

Rabinowitz, D. L., Barkume, K., Brown, M. E., et al. 2006, ApJ, 639, 1238

Ragozzine, D., & Brown, M. E. 2009, AJ, 137, 4766

Rettig, T., Brittain, S., Simon, T., et al. 2006, ApJ, 646, 342

Rettig, T. W., Haywood, J., Simon, T., Brittain, S. D., & Gibb, E. 2004, ApJL, 616, L163

Rieke, G. H., Young, E. T., Engelbracht, C. W., et al. 2004, ApJS, 154, 25

Rodler, F., Lopez-Morales, M., & Ribas, I. 2012, ApJL, 753, L25

Rothman, L. S., Gordon, I. E., Barbe, A., et al. 2009, J. Quant. Spectrosc. Radiat. Transfer, 110, 533

Salyk, C., Blake, G. A., Boogert, A. C. A., & Brown, J. M. 2007, ApJL, 655, L105

—. 2009, ApJ, 699, 330

—. 2011, ApJ, 743, 112

Salyk, C., Pontoppidan, K. M., Blake, G. A., et al. 2008, ApJL, 676, L49

Sano, T., Miyama, S. M., Umebayashi, T., & Nakano, T. 2000, ApJ, 543, 486

Sargent, A. I., & Beckwith, S. 1987, ApJ, 323, 294

Scargle, J. D. 1982, ApJ, 263, 835

Schaller, E. L., & Brown, M. E. 2007, ApJL, 659, L61

Seager, S., & Deming, D. 2010, ARA&A, 48, 631

Seager, S., Richardson, L. J., Hansen, B. M. S., et al. 2005, ApJ, 632, 1122

Semenov, D., Wiebe, D., & Henning, T. 2004, A&A, 417, 93

Siess, L., Palacios, A., Charbonnel, C., Decressin, T., & Forestini, M. 2007, Astrophysics Software Database, 34

Sneden, C. 1973, ApJ, 184, 839

Snellen, I. A. G., de Kok, R. J., de Mooij, E. J. W., & Albrecht, S. 2010, Nature, 465, 1049

Spearman, C. 1904, American Journal of Psychology, 15, 72

Spitzer, L. 1978, Physical processes in the interstellar medium

Stansberry, J., Grundy, W., Brown, M., et al. 2008, Physical Properties of Kuiper Belt and Centaur Objects: Constraints from the Spitzer Space Telescope, ed. M. A. Barucci, H. Boehnhardt, D. P. Cruikshank, A. Morbidelli, & R. Dotson, 161–179

Stellingwerf, R. F. 1978, ApJ, 224, 953

Strom, K. M., Strom, S. E., Edwards, S., Cabrit, S., & Skrutskie, M. F. 1989, AJ, 97, 1451

Swain, M. R., Vasisht, G., & Tinetti, G. 2008, Nature, 452, 329

Swain, M. R., Tinetti, G., Vasisht, G., et al. 2009, ApJ, 704, 1616

Swain, M. R., Deroo, P., Griffith, C. A., et al. 2010, Nature, 463, 637

Takeda, G., Ford, E. B., Sills, A., et al. 2007, ApJS, 168, 297

Thi, W. F., Kamp, I., Woitke, P., et al. 2013, A&A, 551, A49

Thomas, P. C., Parker, J. W., McFadden, L. A., et al. 2005, Nature, 437, 224

Tinetti, G., Vidal-Madjar, A., Liang, M.-C., et al. 2007, Nature, 448, 169

Trujillo, C. A., Brown, M. E., Barkume, K. M., Schaller, E. L., & Rabinowitz, D. L. 2007, ApJ, 655, 1172

Udry, S., & Santos, N. C. 2007, ARA&A, 45, 397

Valenti, J. A., Butler, R. P., & Marcy, G. W. 1995, PASP, 107, 966

van der Marel, N., van Dishoeck, E. F., Bruderer, S., et al. 2013, Science, 340, 1199

van der Tak, F. F. S., Black, J. H., Schöier, F. L., Jansen, D. J., & van Dishoeck, E. F. 2007, A&A, 468, 627

Vasyunin, A. I., Semenov, D., Henning, T., et al. 2008, ApJ, 672, 629

Weiss, L. M., Marcy, G. W., Rowe, J. F., et al. 2013, ApJ, 768, 14

Wernli, M., Valiron, P., Faure, A., et al. 2006, A&A, 446, 367

Wiedemann, G., Deming, D., & Bjoraker, G. 2001, ApJ, 546, 1068

Wilson, T. L. 1999, Reports on Progress in Physics, 62, 143

Woitke, P., Kamp, I., & Thi, W.-F. 2009, A&A, 501, 383

Wright, J. T., Marcy, G. W., Howard, A. W., et al. 2012, ApJ, 753, 160

Wright, J. T., Fakhouri, O., Marcy, G. W., et al. 2011, PASP, 123, 412

Yang, B., Stancil, P. C., Balakrishnan, N., & Forrey, R. C. 2010, ApJ, 718, 1062

Zucker, S., & Mazeh, T. 1994, ApJ, 420, 806

—. 2001, ApJ, 562, 1038

Appendices

Appendix A

RADLite Manual

RADLite is a code designed to generate spectra from a protoplanetary disk or embedded protostars. The input disk parameters are generated by RADMC (Dullemond & Dominic 2004) and include the dust density and temperature structure, gridded radially and vertically. The code has been optimized to calculate the full radiative and collisional excitation of a species of molecule in addition to the state of local thermodynamic equilibrium for every point in the grid. Finally, a 1-D spectra or a 2-D image of the disk can be generated using an included raytracer.

A.1 Continuum Radiative Transfer

See the RADMC manual for a full description of the radiative transfer routine. For this manual, the user must change values in `problem_params.pro` to determine the initial disk conditions used in the dust continuum radiative transfer.

A.2 Flow Chart and Description of Routines

- `hitran_extract.pro`

  Extracts molecular information from the HITRAN database and writes molecular

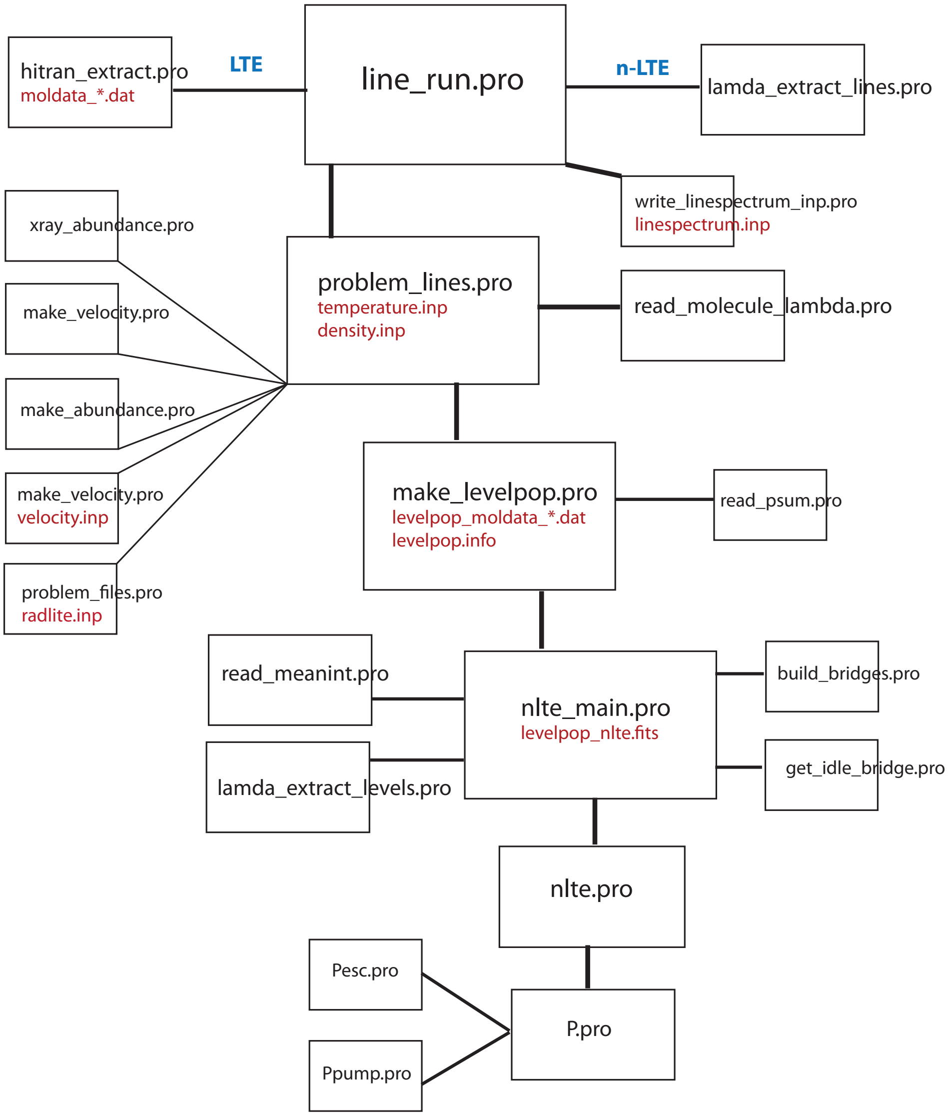

Figure A.1: Routines called during a run of RADlite. The output is given in red for each routine.

data file.

- `lamda_extract_levels.pro`

  User inputs desired levels according to maximum vibrational and rotational level. The levels are extracted from the molecular file as a whole, as are all transitions involving those levels. All collisional transitions are weighted according to collisional partner abundance and interpolated onto one temperature grid, for interpolation in P.pro.

- `lamda_extract_lines.pro`

  Similar to `hitran_extract.pro` except extracts data from LAMDA formatted file.

- `line_run.pro`

  Breaks into sub-runs and creates `moldata_#.dat` for each. Calls `problem_lines.pro` to create level population information and then calls the RADLite executable to generate spectra. Each call of this routine creates a separate time-stamped directory for the output.

- `make_levelpop.pro`

  The level populations of the molecule are determined and stored in the levelpop_moldata.dat files, with the meta data stored in levelpop.info. If non-LTE has been selected, nlte_main.pro is called, otherwise level populations are set to LTE using the temperature structure and partition sum that is calculated previously.

- `nlte.pro`

  This program solves the equations of statistical equilibrium. First, `P.pro` generates all the rate coefficients for the level transitions and then uses a Newton-Rhapson iteration to converge onto a solution for the level populations. The user can set a convergence criteria as a maximum fractional difference between iterations.

- `nlte_main.pro`

  The mean intensity field is read from the RADMC output and interpolated to the desired frequencies. Also, if the user chooses to specify the number of levels to populate (using maximum v and j values from `line_params.ini`), these levels and the associated transitions are uniquely selected. The radii are then processed separately, either consecutively or in parallel using the build_bridges function of IDL, and `nlte.pro` is called for each radius. All the radii are combined at the end and the population file levelpop_nlte.fits is created.

- `P.pro`

  The optical depth along the vertical column is computed and used to calculate the probability of escape (`Pesc.pro`) and of being captured and pumping the lines (`Ppump.pro`). These probabilities, along with the interpolated intensity field, the Einstein A and B coefficients, and the collisional rate coefficients, are used to calculate the rate of transitions between any two levels. The output is an n by n matrix where n is the number of levels specified by the user. The final row in the matrix is populated with the total abundance in the cell in order to conserve mass and constrain the solution.

- `Pesc.pro`

  Calculates the escape probability at a given depth in the disk using the prescription described in Woitke et al. (2009).

- `Ppump.pro`

  Same as `Pesc.pro` but calculates the probability a photon will be re-absorbed, adding to the intensity field.

- `problem_lines.pro`

  This module generates the gas structure input files including temperature, density, abundance, turbulence and velocity profiles, each gridded with height and radius in the disk, and then calls `make_levelpop.pro`.

- `read_molecule_lambda.pro`

  This routine reads the molecular information, including energy levels and radiative and collisional transition rates, from an input file and returns an easily manipulated package.

A.3 Line Excitation

The molecular excitation is calculated from the radiative and collisional environment, solving the equations of statistical equilibrium for multiple vibrational and rotational levels.

A.4 Generating Spectra

Spectra are generated using a call to `line_run.pro`.

Appendix B

Direct Detection Manual

B.1 TERRASPEC

B.1.1 Getting Started

Choose and enter a directory for your work, let's call it *radtrans.* To begin you must acquire 3 tar balls, one with the bulk of the program, another containing additional IDL procedures you will use, and a final package with all the line lists for the atmospheric radiative transfer model. These will be called **terraspec_v#.##.tar**, **terraspecdep_#.tar** and **aer_v_##.tar.gz**, respectively. Begin by unpacking the first two:

```
tar xvf terraspec_v#.##.tar
tar xvf terraspecdep_#.tar
```

This will generate a file called **terraspec.pro**. This file contains instructions on how to unpack the third tar ball and correctly link the files for using TERRASPEC. Do not forget to link the current directory, *radtrans*, to your IDL path in your **.cshrc** file so all of the procedures you just unpacked can be properly accessed by IDL.

B.1.2 Initial Telluric Removal

Initialize IDL. At the prompt type

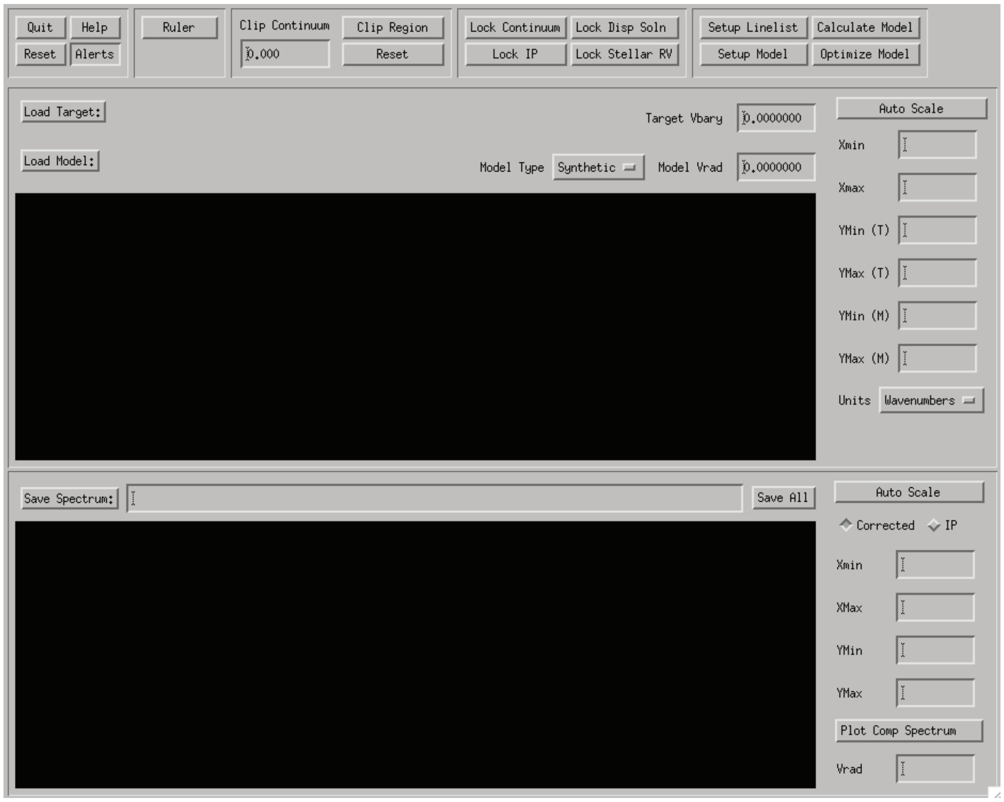

Clip Continuum 0.000

Target Vbary 0.0000000

Model Type Synthetic

Model Vrad 0.0000000

Units Wavenumbers

Figure B.1: Graphic User Interface for TERRASPEC.

```
terraspec
```

and press enter. If a graphic user interface (GUI) window does not appear immediately, something is wrong with the setup. Go back and make sure all the initial checks listed in **terraspec.pro** worked correctly. The GUI should look like Fig. B.1.

Click “Load Target:” and choose the file containing a wavelength-calibrated spectrum. The first line of the file should consist of a header line with Julian Date, barycentric velocity, systemic velocity, and file name. The rest of the file should be two columns containing the wavelength and flux. Wavelength can be in Angstroms, microns or wavenumbers. If the file loads properly, a spectrum should appear in white in the top graph.

Next click “Load Model:” and select the file containing the stellar model, which should also be a two column file, with wavelength (same units as target spectra) in the first column and normalized flux in the second column. If the barycentric or systemic velocities were not recorded properly in the header of the target file, they can be manually entered now in the corresponding boxes. If the stellar velocity is well known, click "Lock Stellar RV" at the top of the screen. The stellar spectrum will be shown in light blue on top of the target spectra.

Click "Setup Linelist" and ensure that the correct AER line file appears at the top of the pop-up GUI. In this box you can select which molecules to include in the atmospheric fitting. The default setting is to use the seven most abundant species, which is the most likely case you will need. Adding other molecules to the fit can be accommodated by pressing the corresponding box. Click "Close" to exit this GUI.

Next choose "Setup Model" which will bring about another pop-up window with 5 tabs. We will only modify the first tab that says "Summary." Choose the desired Atmospheric Model from the pull down menu; the climate for Keck in Hawaii is considered tropical. Set the observer location if different from the default of Mauna Kea. If the zenith angle of the observations is known (from recorded airmass values), enter this value in the appropriate box. If unknown, this parameter can be fit by the model by clicking the "Zenith Ang" box under "Other Pars:" in the bottom right corner of the window.

For the first run of TERRASPEC, we will not allow any molecular values to vary. Instead, we will specify the value of the precipitable water vapor for the evening and assume all other molecules are at their nominal abundances. We will allow these to vary later. Choose the number of molecules to be scaled ("Num. Mol. Scaled"). Entering a value of six allows the user to change the values of H_2O, CO_2, O_3, N_2O, CO and CH_4. Then choose water from the drop down menu and click the button next to "p", which stands for precipitable water vapor. In the "Scaling Value" box, enter the amount of precipitable vapor from the observations in units of cm (e.g., if there were 4 mm of precipitable water vapor that night, enter 0.4).

Now we will specify the fit parameters to optimize. At the bottom of the menu, click all options under “Continuum Fit:” so that four boxes become active in the middle of the window (identified as “C(0)”, “C(1)”,“C(2)”, and “C(3)”). The box “Response Coeff. Width” should also be active. At the bottom again, unclick all depressed boxes under “Response Function:”. We will deal with these later.

We have now instructed TERRASPEC to create an atmospheric model with a given column of water vapor and a typical tropical atmospheric profile. A third order polynomial will be fit to the continuum and the instrument profile will be fit as a single Gaussian with a parameterized width. Close the pop-up window and click “Calculate Model” in the upper right corner of the main TERRASPEC screen. Within a minute, an initial telluric fit should appear in red plotted in the upper graph, on top of the data and stellar model. The continuum fit is plotted in yellow. A pop-up window will appear to notify you the model is done – click “Close” to dismiss.

The final step is to click “Optimize Model”, which will take several minutes and up to 200 iterations to converge on a solution. The program is fitting a continuum solution, as well as an IP width and any other parameters that were left active. The IDL window will display each variable as it changes during the iteration process. When the fit is complete, dismiss the pop-up window that appears, and click “Save Spectrum.” There will be a file saved to your directory with the name of the target spectra plus “.terra.”

B.1.3 Instrument Fringing Removal

The NIRSPREC instrument has a well documented fringe that is caused by reflectance off of the dewar window. For very high S/N observations it is necessary to remove this fringe. After the initial telluric removal, the strongest fringe is usually visible by eye, but we solve for its power and remove it. First though, we remove the stellar lines, which have been fit by TERRASPEC but not removed. From here we work from a file called `target_date_order.terra` that is output from the previous step, as well as stellar and planetary templates named `stellar_model` and `planet_model`. At the IDL prompt type:

```
removestar,'target_date_order','stellar_model,Vbary=##,Vrad=##,$
IP=[IP1, IP2, IP3, IP4, IP5, IP6, IP7, IP8, IP9],/REJECT
```

The final call in the above routine rejects any points whose variance is great that 1.5. The result of this call is to generate a `target_date_order.terra.nostar` file. Next we remove the fringes using `bulkfringe.pro` which calls `cleanlomb.pro` several times.

```
bulkfringe,'target_date_order'
```

which returns the frequency, power, and significance of the strongest periodic signal in the data and prompts the user to find another fringe. While the prompt actually asks if you would like to remove another fringe, the removal does not happen until the end. The user should keep choosing to remove fringes until the power of the fringes is consistently $\leq$10. The two fringes that appear consistently have frequencies of 1.75 and 2.18 (cm^{-1}), but they might not appear until more than a dozen other frequencies appear. There can be some longer wavelength frequencies that have power if the continuum was not fit perfectly well, or very high frequency fringes that can be ignored. With experience the user will become familiar with this step and the required number of frequencies to examine, but as a beginning metric continuing measuring fringes until either a) both aforementioned fringes have been found or b) 15 fringes have been fit. At this point, answer no (`'n'`) to the prompt and the routine will ask you which fringes you want to keep, one by one. Select yes (`'y'`) for the aforementioned fringes, as well as any whose power is $\gtrsim$ half of the highest power frequency. Only with experience can a user become comfortable with this process. The output of this routine is to produce a `target_date_order.defringe` file that is used as an input for the following step.

B.1.4 Final Telluric Removal

As before, enter TERRASPEC in IDL. Follow the steps listed above through the model optimization step, using your `target_date_order.defringe` as the target spectra.

After the continuum has been fit, it is time to start varying the atmospheric abundances. Each order must be dealt with separately. Click the "Load Model" button again and follow the instructions for the correct order, in the following order:

Order 22: Turn on methane scaling by clicking the box next to "CH4" under "Column Scaling:". Close that window and proceed to calculate and then optimize the model. After the optimization has finished, go back to the "Load Model" screen and turn on "L Sat 1", "L Sat 2", "R Sat 1", and "R Sat 2" under "Response Function:". Re-calculate, re-optimize, and save the `.defringe.terra` file. The molecular abundance and instrument profile parameters will update on the Terminal screen for every iteration. Be sure to record what the final values are for the saved fit.

Order 25: Turn on water scaling by clicking the box next to "H2O" under "Column Scaling:". Close that window and proceed to calculate and then optimize the model. After the optimization has finished, go back to the "Load Model" screen and turn on "CO2" and "L Sat 1", "L Sat 2", "R Sat 1", and "R Sat 2." Re-calculate, re-optimize, and save the

`.defringe.terra` file. The molecular abundance and instrument profile parameters will update on the Terminal screen for every iteration. Be sure to record what the final values are for the saved fit.

Order 23: Adjust the water and methane abundances to those calculated in orders 25 and 22, respectively, for use as initial values in the fit. This is done by selecting the molecule from the drop down list in the top box, clicking “l” for linear fit, and typing in the abundance, as read from the Terminal output, into the “Scaling Value” box. Now turn on “H2O” and “CH4.” Close that window and proceed to calculate and then optimize the model. After the optimization has finished, go back to the “Load Model” screen and turn on “L Sat 1”, “L Sat 2”, “R Sat 1”, and “R Sat 2”. Re-calculate, re-optimize, and save the `.defringe.terra` file.

Order 24: Same as order 23.

B.1.5 Cleaning the data

Even after the second telluric removal, the data might need to be cleaned. If the line shape has not been fit precisely, or if the continuum does not model the edges of the order correctly, it is sometimes necessary to go in by hand and remove certain features. We can also account for cosmic rays or other obvious unphysical features in the spectra. After cleaning, save the `.defringe.terra.clean` file for the next steps.

B.2 TODCOR

The TODCOR package should come with a number of routines, including `sxcorr.pro`, `sxcorr_calc1d.pro`, `sxcorr_calc2d.pro`, `sxcorr_control.pro`, `sxcorr_correlation.pro`, `sxcorr_target.pro`, `sxcorr_template.pro` and `sxcorr_units.pro`. Make sure these routines are in your IDL path.

B.2.1 Convolving to the Instrument Resolution

One of the outputs of each TERRASPEC run is an instrument profile, which defines the resolving power of telescope as measured by the program. We will convolve this profile with the stellar and planetary templates, for each of the orders, to generate the appropriate templates for the cross-correlation. To convolve model template called `planet_model` with an instrument profile of [IP1, IP2, IP3, IP4, IP5, IP6, IP7, IP8, IP9] you would type

```
model = readspec('planet_model', header=header, hdata=hdata)
x = terraspecip(model, [IP1, IP2, IP3, IP4, IP5, IP6, IP7, IP8, IP9] )
writespec, x, 'targetname_date_modeltype_ordernumber_IPconv', hdata
```

where the filename is specified in the last command. You will need to run the convolve both templates with the instrument profile measured for each order for every epoch. I suggest making the file names as specific as possible to keep everything organized.

B.2.2 Cross Correlating Each Order

After, compiling, a GUI is opened by typing

```
sxcorr
```

at the IDL prompt. The rest of the instructions involve interacting with the GUI. Figure B.2 is what should pop up on your screen. The GUI should be open to the "Target" tab. Click "Load Target Spectrum:" and select your `'target_date_order.defringe.terra.clean'` file. Clicking "OK" should load the spectrum onto the screen. If this does not happen, check that the header is properly set with the Julian Date, barycentric velocity, radial velocity, and file name and try again. Other error messages, should they occur, will be described in

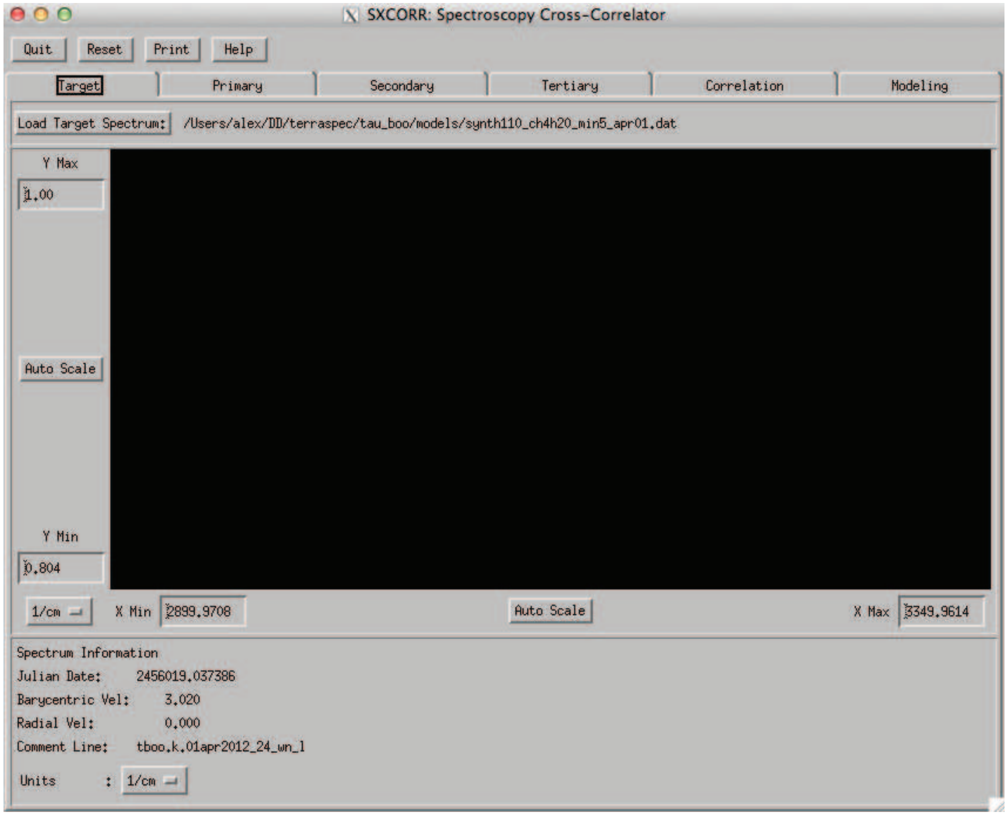

/Users/alex/DD/terraspec/tau_boo/models/synth110_ch4h20_min5_apr01.dat

Y Max: 1.00

Y Min: 0.804

1/cm

X Min: 2899.9708

X Max: 3349.9614

Spectrum Information
Julian Date: 2456019.037386
Barycentric Vel: 3.020
Radial Vel: 0.000
Comment Line: tboo.k.01apr2012_24_wn_1
Units : 1/cm

Figure B.2: Graphic User Interface for TODCOR.

the Terminal screen. After the target spectrum is loaded, make sure the unit boxes (in the lower left corner) for the plot and for the file are set correctly. The default is “Ang.” for Angstroms, but the files we work with are in wavenumbers, so change both of these boxes to “1/cm”. You may adjust the scale on the spectrum here as well.

Click the “Primary” tab and load the stellar template. Again, check that all the header information has been recorded correctly and change the units to wavenumbers. Adjust the scale on the plot as necessary. Repeat for the planetary template under the “Secondary” tab. Be sure that the target, the primary and the secondary spectra all references the same date and order.

Now go to the “Correlation” tab. On the left hand side you will see three sets of “Vmin” and “Vmax” boxes, corresponding to the primary,secondary, and tertiary (which we will ignore). These indicate the limits of velocity space that the cross correlation will search. Setting these limits unnecessarily high will increase the computing time. The primary, or stellar, velocity should not be much more than the combined radial (systemic) and barycentric velocities, since the planet does not induce stellar shifts on the order of multiple km/s. A conservative velocity space to sample for the primary target is usually -100 km/s to 100 km/s. Enter these values into the corresponding boxes. The secondary limits should be similarly scaled, where the maximum velocity shift of the planetary spectra is going to be the barycentric velocity added to the planetary radial velocity. For RV-detected planets, the upper limit on the second value will be the orbital velocity of the planet, which should already be known. Be conservative and enter the appropriate "Vmin" and "Vmax" values. For example, τ Boo b has an orbital velocity of ~157 km/s and the barycentric velocity should not exceed ±30 km/, so limits of -200 km/s and 200 km/s are used.

Next, the user must enter the estimated flux ratio between the secondary and primary in the box labeled "alpha1 (Sec/Pri)". This can be varied in subsequent trials and the correlations compared for further analysis.

Finally, click "Update 1D" to generate the cross correlation function (CCF) for the primary with the target. Within several seconds, the correlation plot should appear. The cursor will become active in the plotting window – click and drag to make a box that includes the peak of the CCF. Upon release this region of the correlation will be highlighted and the velocity of the peak will appear at the top of the window. This will be used as a guideline when the 2-D correlation is run. Next choose "Update 2D" and let the program run. It will normally take 15-30 minutes per model. Once the program is finished running you might need to adjust the scaling on the plotting window to see the planetary CCF. If you would like to save either 1D or 2D correlation, depress the "Save Raw Correlation

Data" button before updating the plots.

For future use, I suggest renaming the resulting `sxcorr_raw1d.##...##.idl.sav` to something more descriptive.

B.2.3 Combining Orders of a Given Epoch

Now you have a number of cross correlation files, each corresponding to a given order on a given date. We will combine the orders to make one representative CCF per epoch for the next step. To do this, we will use the program, `mlcombine2d.pro`. In IDL, enter

```
mlcombine2d, ml, ml_pvfinal, ml_svfinal, ml_nn, pcut, scut
```

and a window will pop up prompting you to select the files to combine. Holding down the control button will allow you to select multiple files. Select the 2D cross correlation files from all orders for a given date. The window will automatically filter the search for files so make sure that your files are named accordingly – usually beginning with "sxcorr_raw2d" or "raw2d." Once all files have been selected click "OK", which should bring up a new plotting window with the 1D stellar CCF.

The mouse is once again active and the Terminal will prompt you to select the left edge of the peak. Do so by clicking the right mouse button. Repeat for the right edge of the peak. On the bottom half of the window is now plotted a 1D cut of the 2D CCF, centered on the chosen peak from the plot above. Again you are prompted for a left and right edge of a peak, this time from the bottom plot. At this point you can choose any velocity peak (highest peak is set as the default and was used to make the upper plot). Select 'n' when prompted to recalculate peak. If the expected planetary velocity for a given epoch is known, you may choose to select this value of the planetary CCF and then choose to recalculate the peak. This will re-display the upper plot, which is actually also a 1D cut of the 2D

CCF, only along the stellar velocity variable, which has now been centered on the chosen planetary velocity. The process may be iterated several times, if desired.

Once the process is complete, we want to save the data with

```
save, ml, ml_pvfinal, ml_svfinal, ml_nn, pcut, scut, $
filename='target_date_OtherInfo.sav'
```

Repeat this process for all epochs.

B.3 Creating a Maximum Likelihood Curve

I have developed a program, `max_likelihood.pro`, that will generate a maximum likelihood curve for multiple epochs of data. The program will calculate the likelihood of a range of radial velocities given the CCFs associated with different phases. In the program the user inputs include "start_kp" and "end_kp" to determine the velocity range tested, the orbital period of the planet "P" and the radial velocity, "grad". The user also inputs three arrays that contain the phases of the observations, "t", the barycentric velocities of each of the epochs, "vbary", and the file names saved above as `target_dat_OtherInfo.sav'` in the vector called "files." The maximum log likelihood is computed as the product of the probabilities of each planetary velocity at a given epoch. The program is run after compilation at the IDL command line with

```
max_like
```

which prints the log likelihood of every k_p and displays a maximum likelihood plot at the end.